# Two-dimensional ideal magnetohydrodynamic waves on a rotating sphere under a non-Malkus field: I. Continuous spectrum and its ray-theoretical interpretation

Ryosuke Nakashima†**and Shigeo Yoshida‡

†Faculty of Science, Kyushu University, Fukuoka, Japan

‡Department of Earth and Planetary Sciences, Faculty of Science, Kyushu University, Fukuoka, Japan

October 3, 2023

**Abstract**

Two-dimensional (2D) ideal incompressible magnetohydrodynamic (MHD) linear waves at the surface of a rotating sphere are studied as a model imitating the outermost Earth's core or the solar tachocline. This thin conducting layer is permeated by a toroidal magnetic field whose magnitude depends only on the latitude. The Malkus background field, which is proportional to the sine of the colatitude, gives two well-known groups of branches on which Alfvén waves gradually become fast or slow magnetic Rossby (MR) waves as the field amplitude decreases. For non-Malkus fields, we show that the associated eigenvalue problems can yield a continuous spectrum instead of Alfvén and slow MR discrete modes. Critical latitudes attributed to the Alfvén resonance wipe out these discrete eigenvalues and produce an infinite number of singular eigenmodes. The theory of slowly varying wave trains in an inhomogeneous magnetic field shows that a wave packet related to this continuous spectrum propagates toward a critical latitude corresponding to the wave and is eventually absorbed there. The expected behaviour that the retrograde propagating packets which pertain to the continuous spectrum approach the latitudes from the equatorial side and that the prograde ones approach there from the polar side is consistent with the profiles of their eigenfunctions shown by our numerical calculations. Further in-depth discussions of the Alfvén continuum would progress the theory of "wave-mean field interaction" in the MHD system and one's understanding of the dynamics in such thin layers.

**Keywords:** Magnetic Rossby waves; Continuous modes; Stably stratified layer; Geomagnetic variations;

## 1 Introduction

Geomagnetic and geodetic variations may partly be accounted for by MHD waves within the Earth's outer core (e.g. Gillet *et al.*, 2021; Triana *et al.*, 2021; Hori *et al.*, 2023). For example, Hide (1966) suggested that the westward drift of the geomagnetic field may originate from slow MR waves in the liquid core. Braginsky (1970) ascribed both the 60-year length-of-day and geomagnetic variations to the torsional oscillations. If this type of attribution is substantiated, the comparison between observations and the theory leads to some inferences on the relevant physical quantities. Zatman and Bloxham (1997) accepted Braginsky (1970)'s explanation to infer that the magnitude of the cylindrical radial field is about $0.2\,\mathrm{mT}$. This suggestion was questioned by Gillet

---

**Corresponding author. Email: r.nakashima.geophysics@gmail.com

*et al.* (2010), who associated the torsional oscillations (or torsional waves) with six-year length-of-day signals to conclude that its magnitude is about $2\,\mathrm{mT}$.

A stably stratified layer at the top of the outer core has been proposed on various grounds. Simple thermal (Gubbins *et al.*, 1982) and compositional (Braginsky, 1984) stratification were considered first, and the proposed physical mechanisms of stratification have been more sophisticated lately. For the thermal stratification, a subadiabatic temperature gradient due to the core's high thermal conductivity (Pozzo *et al.*, 2012; Zhang *et al.*, 2022) has been invoked, and for the compositional stratification, barodiffusion and chemical interactions between the core and the mantle (Buffett and Seagle, 2010; Gubbins and Davies, 2013; Brodholt and Badro, 2017; Davies *et al.*, 2018), and a remnant of the Moon-creating impact (Landeau *et al.*, 2016) were proposed. Seismological evidence for such a layer has been controversial (e.g. Helffrich and Kaneshima, 2010; Kaneshima, 2018; Irving *et al.*, 2018; van Tent *et al.*, 2020). Regional, instead of global, stratification arising from the core-mantle boundary (CMB) heterogeneity was also proposed (Mound *et al.*, 2019). The obscure properties of the layer may be able to be inferred from the identification of sources of geomagnetic and geodetic signatures from the core.

Magnetic-Archimedes-Coriolis (MAC) and MR waves in such a stably stratified layer at the top of the core have often been invoked as possible causes of geomagnetic fluctuations (Braginsky, 1993, 1998, 1999; Buffett, 2014; Chulliat *et al.*, 2015; Buffett *et al.*, 2016; Knezek and Buffett, 2018; Chi-Durán *et al.*, 2021). If the stratified layer exists atop the core, vigorous convection prevailing in the bulk of the core overshoots the interface between the bulk and the layer (Takehiro and Lister, 2001; Gastine *et al.*, 2020) and can excite MHD waves that travel in the layer (Jaupart and Buffett, 2017; Buffett and Knezek, 2018; Couston *et al.*, 2017; Bouffard *et al.*, 2022).

Two-dimensional ideal incompressible MHD linear waves within a thin conducting fluid layer over a rotating sphere are addressed by the present paper. A non-uniform toroidal ($\phi$-directional, $\phi$ being the longitude) magnetic field is imposed on the fluid film as a background field, and the layer rotates almost rigidly with the sphere. To examine Hide (1966)'s suggestion, a similar problem was first considered by Stewartson (1967), in which the azimuthal main field is spatially uniform. Such a toroidal field does not vanish even at the north and south poles ($\theta = 0$ and $\pi$, where $\theta$ is the colatitude). One should therefore express the basic field as $B_{0\phi}(\theta) = B_0 \mathcal{B} \sin\theta$ with a constant $B_0$ and a bounded continuous function $\mathcal{B}(\cos\theta)$. Although a smooth background field at the poles also requires the function $\mathcal{B}$ to satisfy that $\mathcal{B}\sin\theta = -\sum_{n=1}^{\infty} t_n (\mathrm{d}\mathrm{P}_n/\mathrm{d}\theta)$, where $t_n$ ($n = 1, 2, \ldots$) are constants and $\mathrm{P}_n$ is the Legendre polynomial of degree $n$, we now disregard this condition. The simplest profile $B_{0\phi} = B_0 \sin\theta$ in this expression, or $\mathcal{B} = 1$, is equivalent to the well-known Malkus field (e.g. Malkus, 1967; Finlay, 2008). This elementary 2D model is useful to qualitatively understand the wave dynamics in the thin layer at the top of the core.

The dispersion relation of 2D waves under the Malkus background field should be reviewed before moving on to our main topic. Under the Malkus field, the local Alfvén wave velocities are $V_{\mathrm{A}\phi}(\theta) = (B_0/\sqrt{\rho_0 \mu_\mathrm{m}}) \sin\theta$, where $\rho_0$ is a uniform density and $\mu_\mathrm{m}$ is a constant magnetic permeability. If other effects are absent, local Alfvén waves with speeds proportional to $\sin\theta$ can collectively travel in concert in the azimuthal direction like the rigid body rotation. This reduces our perturbation equations to a regular Sturm-Liouville problem because interior poles vanish (Boyd, 1981), as will be shown in Section 2. If the Malkus field permeates a rigidly rotating thin layer on top of a sphere with a radius $R_0$, the dispersion relation for the 2D ideal incompressible MHD wave (Zaqarashvili *et al.*, 2007; Márquez-Artavia *et al.*, 2017) is given by

$$\lambda = \frac{-m \pm m\sqrt{1 + 4\alpha^2 n(n+1)[n(n+1)-2]}}{2n(n+1)}, \tag{1}$$

where $\lambda \equiv \omega/2\Omega_0$ is the angular frequency nondimensionalised by the double of the constant rotation rate $\Omega_0$. In the above expression, $m$ denotes the (positive) zonal wavenumber, $\alpha \equiv B_0/2\Omega_0 R_0 \sqrt{\rho_0 \mu_\mathrm{m}}$ is the (signed) Lehnert number, and $n$ is the degree of the associated Legendre polynomial $\mathrm{P}_n^m(\cos\theta)$. Although the Lehnert number is often defined as $Le \equiv 2|\alpha|$ in geophysics literature, we follow the precedents referred to above. The double sign in (1) corresponds to prograde and retrograde propagating Alfvén waves $\lambda \simeq \pm m|\alpha|\sqrt{1 - 2/n(n+1)}$ for large $|\alpha|$, and the two classes of MR waves as $|\alpha| \to 0$: the slow mode $\lambda \simeq m\alpha^2[n(n+1)-2]$ peculiar to the MHD system and the fast mode $\lambda \simeq -m/n(n+1)$. The last is closely related to (hydrodynamic) Rossby waves celebrated in meteorology and oceanography (e.g. Longuet-Higgins, 1968). Figure 1 shows that the exponent of $|\alpha|$ in a branch of $\lambda$, or $(\partial \log|\lambda|/\partial \log|\alpha|)$, can be used to distinguish among the three types of waves derived from (1).
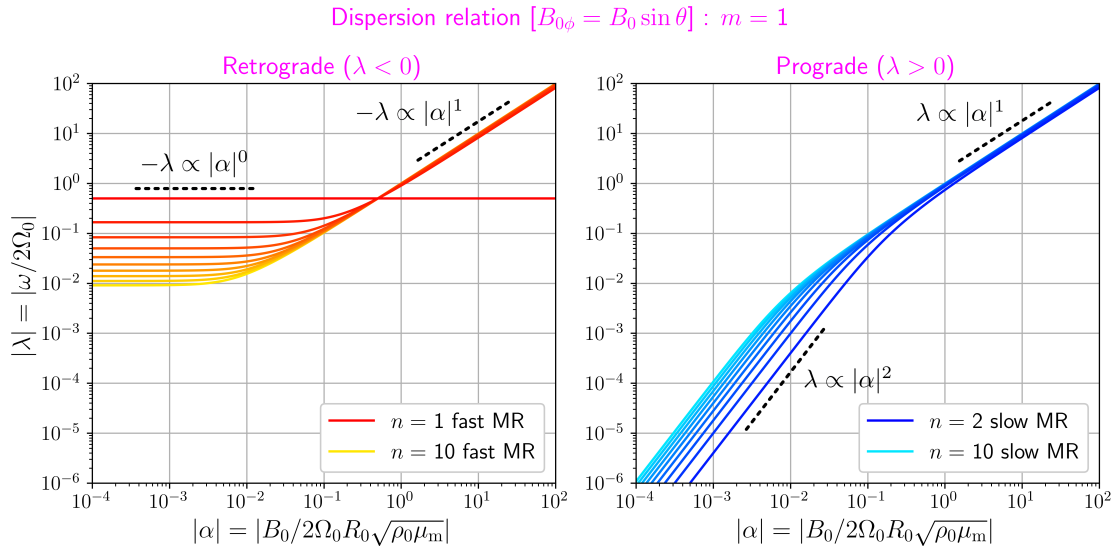
Figure 1: Nondimensional angular frequency $\lambda$ calculated from (1) as a function of the absolute value $|\alpha|$ of the Lehnert number when the zonal wavenumber $m = 1$. The left panel shows retrograde propagating waves ($\lambda < 0$) and the right corresponds to prograde ones ($\lambda > 0$). Fast MR waves for $n = 1, 2, \ldots, 10$ are represented as the warm colour curves, while slow MR waves for $n = 2, \ldots, 10$ are depicted as the cold colour curves. As $|\alpha| \to \infty$, these modes approach the lines $|\lambda| \propto |\alpha|^1$ of Alfvén waves except for $m = n = 1$.

The simplest equatorially-antisymmetric non-Malkus field $B_{0\phi} = B_0 \sin\theta \cos\theta$, or $\mathcal{B} = \cos\theta$, should be more appropriate for the Earth's core than the pure Malkus field. In the current study, we devote our attention to the case of this basic field profile because MHD waves under a non-Malkus field are poorly understood. Note that the field is eastward in the northern hemisphere when $B_0 > 0$, and westward when $B_0 < 0$. It is important that $|\alpha|$ is much smaller than unity in the Earth's core. If the field strength $|B_0|$ inside the core is several millitesla (Gillet *et al.*, 2010), one can estimate that $|\alpha| \approx 10^{-4}$ with $\Omega_0 \approx +0.729 \times 10^{-4}\,\mathrm{s}^{-1}$, $R_0 \approx 3480\,\mathrm{km}$, $\rho_0 \approx 10^4\,\mathrm{kg\,m^{-3}}$ and $\mu_\mathrm{m} \approx 1.26 \times 10^{-6}\,\mathrm{H\,m^{-1}}$.

Non-Malkus fields complicate our linear wave problem because regular singular points appear in their equations. At the singular colatitudes $\theta = \theta_\mathrm{c}$ resulting from the Alfvén resonance, the azimuthal phase velocity $\omega/(m/R_0 \sin\theta_\mathrm{c})$ of a wave is equal to the local Alfvén velocity $V_{\mathrm{A}\phi}(\theta_\mathrm{c})$ at the latitude (e.g. Uberoi, 1972; Goedbloed and Poedts, 2004). For example, such latitudes ordinarily exist for low-frequency neutral modes under a non-Malkus configuration whose function $\mathcal{B}$ has at least one zero in $0 < \theta < \pi$. Even if such points exist for a given angular frequency $\lambda$, one can, however, construct its eigenmode when its eigenfunction is permitted to have singular profiles only at the points, or rather such singular modes are required for completeness (Van Kampen, 1955; Case, 1959; Barston, 1964). This means that its spectrum should include a continuous range, $\min(\mathcal{B}^2) \leq \lambda^2/m^2\alpha^2 \leq \max(\mathcal{B}^2)$. Even though it makes no sense to extract an eigenmode (hereinafter referred to as a "continuous eigenmode" or "continuous mode") from this continuous spectrum as its eigenfunction is singular, the integration (or the superposition) with respect to $\lambda$ in which the integrand is the eigenfunctions weighted by a coefficient depending only on $\lambda$, can constitute a physically relevant solution. Recall that it is not always true that the Fourier transform of a well-behaved function is not pathological. Solutions composed only of the continuous eigenmodes do not show the behaviour being typical of collective oscillations by normal discrete eigenvalues but represent transient growth of initial disturbances (Farrell, 1982) and non-diffusive attenuation (e.g. Adam, 1986). The latter involves the phase mixing and the Landau damping, which cause algebraic decay (Case, 1960; Balmforth and Morrison, 1995b) and exponential decay (Landau, 1946; Briggs *et al.*, 1970; Sedláček, 1971; Tataronis and Grossmann, 1973), respectively. These unintuitive aspects due to the advent of continuous spectra have long been discussed in various research areas: inviscid shear flows, collisionless plasmas, ideal MHD systems, 2D vortices and differentially rotating disks, self-gravitating systems, and the Kuramoto model (e.g. Adam, 1986; Balmforth and Morrison, 1995a; Strogatz, 2000; Barré *et al.*, 2015).

The reasons that we chose the azimuthal field $B_{0\phi} = B_0\mathcal{B}\sin\theta$ are as follows, although the dominant field

may be radial in the Earth's outermost core due to the small conductivity in the mantle (e.g. Knezek and Buffett, 2018). First of all, this model is simpler and can be straightforwardly extended into the "MHD shallow water" system (Zaqarashvili *et al.*, 2007, 2009; Heng and Spitkovsky, 2009; Zaqarashvili *et al.*, 2011; Márquez-Artavia *et al.*, 2017), which was first introduced by Gilman (2000). In contrast with the toroidal field, radial ones normally bring vertical derivatives into their governing equations, and the operator is obviously incompatible with a 2D model, which is computationally undemanding. Secondly, critical latitudes often reside in equations of similar eigenvalue problems even when a radial background field depending on $\theta$ passes through a thin layer (e.g. see the equations in Buffett and Matsui, 2019). Although approximations that are apparently appropriate for each target of study sometimes obliterate the latitudes (Zaqarashvili, 2018; Buffett and Matsui, 2019), it is not clear whether the simplifications that drop the Alfvén resonance are always valid or not. Thus, we need to scrutinise the influences of the critical latitudes on eigenmodes. Lastly, Hardy *et al.* (2020) reported that slight vertical motions under strong stratification can enhance toroidal fields because of the "Malkus constraint." This suggestion supports our choice as a reasonable main field.

Related instability problems may pertain to the dynamics of the solar tachocline underlying the convection zone. Because unstable modes can easily be picked up even in the presence of continuous spectra, this circumstance is significantly different from that of the study of linear waves. Gilman and Fox (1997, 1999a,b) and subsequent work (Dikpati and Gilman, 1999; Gilman and Dikpati, 2000; Zaqarashvili *et al.*, 2010a) examined the "joint instability" or "magnetic Rossby wave instability" arising in the tachocline, which can occur in the MHD system accompanied by latitudinal differential rotation. According to them, some non-axisymmetric infinitesimal perturbations are likely to destabilise the coexistence of the solar-like angular velocity profile deduced from helioseismic observations and a variety of plausible toroidal field configurations such as broad profiles written as $B_{0\phi} = (B_0 + B_1 \cos^2 \theta) \sin \theta \cos \theta$ (in which $B_1$ is also constant) or latitudinally localised field bands expressed by Gaussian functions. These global unstable modes may play an important role in the persistence of such a thin shear layer via latitudinal transport of angular momentum (Spiegel and Zahn, 1992) and put an upper limit on the strength of a toroidal field stored within the layer through the $\omega$-effect (Arlt *et al.*, 2007a,b). The nonlinear evolution of the modes has been developed by Cally (2001) and Cally *et al.* (2003, 2004), who found the novel "clamshell" and "tipping" patterns. Additionally, viscosity and magnetic diffusion were also introduced in the radial (Dikpati *et al.*, 2004) and horizontal (Sharif and Jones, 2005) directions in an anisotropic manner.

Even beyond the strict 2D model, stability analyses of the tachocline have been conducted. The MHD shallow water equations (Gilman, 2000) and the 3D thin shell model or "MHD hydrostatic primitive" equations (Miesch and Gilman, 2004) were newly proposed for evaluating the impacts of subadiabatic stratification and weak vertical displacement of fluid particles. Gilman and Dikpati (2002) and Dikpati *et al.* (2003) demonstrated that the combinations of the differential rotation and the toroidal fields in the shallow model become unstable easily again and that the growing perturbations have non-zero kinetic helicities, which are related to the $\alpha$-effect (Moffatt, 1978). Furthermore, unstable MR waves in the layer may have been causing some periodicities detected in the solar activity (Zaqarashvili *et al.* 2010a,b, 2015; Dikpati *et al.* 2017; Gachechiladze *et al.* 2019; see Zaqarashvili *et al.* 2021, for a review). For instance, nonlinear development in the MHD shallow water system (Dikpati *et al.*, 2017, 2018a,b) indicated that MR waves exchange angular momentum with mean fields and that their wave patterns deformed by consequent reconstructions of the mean profiles can trigger nonlinear quasi-periodic oscillations. In addition, searches for not only non-axisymmetric unstable modes (Cally, 2003; Gilman *et al.*, 2007; Kitchatinov and Rüdiger, 2008) but also axisymmetric ones (Cally *et al.*, 2008; Dikpati *et al.*, 2009) were performed in extensive studies of the 3D thin shell model. The studies currently include nonlinear simulations of these growth modes (Miesch *et al.*, 2007; Hollerbach and Cally, 2009) and linear stability analyses taking vertical profiles of the differential rotation and the background toroidal field into account (Arlt *et al.*, 2007a,b).

Critical lines (or levels, latitudes, and so on) and their concomitant continuous modes have important bearings even on unstable modes which are outside of the objective of this paper. Despite the fact that the eigenfrequencies of unstable modes are complex numbers, their eigenfunctions are affected by the positions of critical points, as demonstrated by, e.g. Gilman and Fox (1999a) and Wang *et al.* (2022a). Moreover, a neutral mode sometimes interacts with continuous modes when the branch of the neutral one overlaps the continuous spectrum. This leads to the appearance of a pair of unstable and decay modes (Iga, 1999; Taniguchi and Ishiwatari, 2006) or non-modal growth (Heifetz *et al.*, 2020). On the other hand, continuous spectra sometimes

cover and hide the branches of such interacting neutral modes (Iga, 2013). Therefore, we also want to detail the critical latitudes and the neutral continuous eigenmodes deeply in advance to understand linear stability in similar problems (e.g Wang *et al.*, 2022b), though our current problem does not have such unstable modes.

Non-ideality and non-linearity are also intimately related to critical points. Small viscosity and magnetic diffusion transform a singular point on the real axis on the "fictional" complex plane of the involved spatial coordinate into a complex turning point, because the diffusion terms include higher-order derivatives (e.g. Drazin and Reid, 1981; Shivamoggi, 1992). Since the eigenfunctions that we are going to seek are functions on the real axis on the complex plane, they then become non-singular. This seems at a glance to mean that we have to recover these ignored damping terms. However, very weak diffusions only give rise to thin boundary layers around the turning points (and by any walls), and the eigenfunctions would still be similar to the profiles of continuous eigenmodes obtained from the non-diffusive limit sufficiently outside the layers. Although decaying normal modes stemming from measurable dissipations (Steinolfson, 1985; Gizon *et al.*, 2020) and nonlinear boundary layers (e.g. Tung, 1979; Maslowe, 1986) may also be somewhat important to our problem, they are beyond the scope of this article.

This paper is organised as follows. In Section 2, we shall derive the governing equations for our problem, and then present a method to seek eigenmodes numerically by the associated Legendre polynomial expansion in Section 2.1. Section 3 gives numerical solutions for the case when the background field is expressed as the simplest equatorially-antisymmetric non-Malkus field $\mathcal{B} = \cos\theta$. In Sections 3.1 and 3.2, the structures of the obtained eigenfunctions are examined outside and near critical latitudes, respectively. In Section 4, we also conduct the numerical integration of ray-tracing equations at large wavenumbers (e.g. Bardsley and Davidson, 2017; Teruya *et al.*, 2022) in order to interpret our eigenvalue problem from a different angle. This approach tracks paths of wave packets migrating with their group velocities. Note that this is different from Dikpati *et al.* (2020)'s calculations of the Stokes drift, which are trajectories of fluid particles advected by oscillatory flow induced by MR waves. Finally, we conclude in Section 5.

## 2 Mathematical formulation

We now begin with a description of the governing equations for the 2D ideal incompressible MHD on a rotating sphere. In the spherical coordinate system $(r, \theta, \phi)$, the 2D vorticity and 2D uncurled induction equations on the spherical surface $r = R_0$ (e.g. Raphaldini and Raupp, 2020) are

$$\frac{\mathrm{D}\zeta}{\mathrm{D}t} - \frac{2\Omega_0 \sin\theta}{R_0} u_\theta = \frac{(\boldsymbol{B} \cdot \boldsymbol{\nabla}_{\mathrm{H}})(\mu_{\mathrm{m}} J)}{\rho_0 \mu_{\mathrm{m}}} \,, \tag{2a}$$

$$\frac{\mathrm{D}A}{\mathrm{D}t} = 0 \,, \tag{2b}$$

where $\boldsymbol{\nabla}_{\mathrm{H}} \equiv (\hat{\boldsymbol{e}}_\theta/R_0)(\partial/\partial\theta) + (\hat{\boldsymbol{e}}_\phi/R_0 \sin\theta)(\partial/\partial\phi)$ is the horizontal nabla operator, and the material derivative is expressed as $(\mathrm{D}/\mathrm{D}t) \equiv (\partial/\partial t) + \boldsymbol{u} \cdot \boldsymbol{\nabla}_{\mathrm{H}}$. The velocity field $\boldsymbol{u} = (0, u_\theta, u_\phi)$ (relative to the rotating frame of reference) and the magnetic field $\boldsymbol{B} = (0, B_\theta, B_\phi)$ are assumed to have only the horizontal components within the thin layer, for the sake of simplicity. The radial components of the vorticity and electrical current in (2) are defined as

$$\zeta \equiv \frac{1}{R_0 \sin\theta}\left[\frac{\partial(u_\phi \sin\theta)}{\partial\theta} - \frac{\partial u_\theta}{\partial\phi}\right] = -\nabla_{\mathrm{H}}^2 \psi \,, \tag{3a}$$

$$J \equiv \frac{1}{\mu_{\mathrm{m}}}\frac{1}{R_0 \sin\theta}\left[\frac{\partial(B_\phi \sin\theta)}{\partial\theta} - \frac{\partial B_\theta}{\partial\phi}\right] = -\mu_{\mathrm{m}}^{-1}\nabla_{\mathrm{H}}^2 A \,, \tag{3b}$$

in which we introduce the stream function $\psi$ and the magnetic vector potential $\boldsymbol{A} = (A, 0, 0)$. Owing to the solenoidal conditions of the fields $\boldsymbol{u}$ and $\boldsymbol{B}$, the scalars $\psi$ and $A$ are related to the two vectors as

$$u_\theta = \frac{1}{R_0 \sin\theta}\frac{\partial\psi}{\partial\phi} \,, \qquad u_\phi = -\frac{1}{R_0}\frac{\partial\psi}{\partial\theta} \,, \tag{4a}$$

$$B_\theta = \frac{1}{R_0 \sin\theta}\frac{\partial A}{\partial\phi} \,, \qquad B_\phi = -\frac{1}{R_0}\frac{\partial A}{\partial\theta} \,. \tag{4b}$$

Using these expressions, the governing equations (2) become

$$\frac{\partial(\nabla_{\mathrm{H}}^2\psi)}{\partial t} + \mathcal{J}(\nabla_{\mathrm{H}}^2\psi, \psi) + \frac{2\Omega_0}{R_0^2}\frac{\partial\psi}{\partial\phi} = \frac{1}{\rho_0\mu_{\mathrm{m}}}\mathcal{J}(\nabla_{\mathrm{H}}^2 A, A)\,, \tag{5a}$$

$$\frac{\partial A}{\partial t} + \mathcal{J}(A, \psi) = 0\,, \tag{5b}$$

where the operator $\mathcal{J}(f, g)$ for any two scalar functions $f$ and $g$ is defined as

$$\mathcal{J}(f, g) \equiv \frac{1}{R_0^2\sin\theta}\left(\frac{\partial f}{\partial\theta}\frac{\partial g}{\partial\phi} - \frac{\partial f}{\partial\phi}\frac{\partial g}{\partial\theta}\right)\,. \tag{5c}$$

In what follows, waves of small amplitude are considered in this system. We introduce a small positive parameter $\varepsilon$ ($\ll 1$) which represents the amplitude of waves to rewrite $\psi$ and $A$ as

$$\psi = \varepsilon\psi_1 + \mathrm{O}(\varepsilon^2)\,, \qquad A = A_0(\theta) + \varepsilon a_1 + \mathrm{O}(\varepsilon^2)\,. \tag{6}$$

The basic state is assumed to be the rigid body rotation $\psi_0 \equiv 0$ with a latitude-dependent toroidal field $B_{0\phi}(\theta)$. With the expression of $B_{0\phi}$ given in the previous section, one obtains $(\mathrm{d}A_0/\mathrm{d}\theta) = -R_0 B_0 \mathcal{B}\sin\theta$. Then, the equations (5) become

$$\left(\frac{\partial}{\partial t}\nabla_{\mathrm{H}}^2 + \frac{2\Omega_0}{R_0^2}\frac{\partial}{\partial\phi}\right)\psi_1 = \frac{1}{R_0\rho_0\mu_{\mathrm{m}}\sin\theta}\left[B_{0\phi}\nabla_{\mathrm{H}}^2 - \frac{1}{R_0}\frac{\mathrm{d}(\mu_{\mathrm{m}}J_0)}{\mathrm{d}\theta}\right]\frac{\partial a_1}{\partial\phi} + \mathrm{O}(\varepsilon)\,, \tag{7a}$$

$$\frac{\partial a_1}{\partial t} = \frac{B_{0\phi}}{R_0\sin\theta}\frac{\partial\psi_1}{\partial\phi} + \mathrm{O}(\varepsilon)\,, \tag{7b}$$

where $J_0(\theta) = \mu_{\mathrm{m}}^{-1}(1/R_0\sin\theta)[\mathrm{d}(B_{0\phi}\sin\theta)/\mathrm{d}\theta]$ is the background electrical current.

The normal mode approach is valid for our purposes. For a given azimuthal wavenumber $m$ and an angular frequency $\omega$ determined later by a dispersion relation, which becomes (1) for the Malkus field $\mathcal{B} = 1$ and is going to be numerically sought in Section 3 when $\mathcal{B} = \cos\theta$, we postulate that $\psi_1(\theta, \phi, t) \equiv \mathrm{Re}[\tilde{\psi}(\mu; m, \omega)\mathrm{e}^{\mathrm{i}\varphi(\phi, t)}] = \tilde{\psi}\mathrm{e}^{\mathrm{i}\varphi}/2 + \mathrm{c.c.}$ and $a_1 \equiv \mathrm{Re}[\tilde{a}\mathrm{e}^{\mathrm{i}\varphi}]$, where $\mu = \cos\theta$ and $\varphi \equiv m\phi - \omega t = m\phi - \lambda\tau$ is the phase of waves with the nondimensional time $\tau \equiv 2\Omega_0 t$. We use c.c. for the complex conjugate of the preceding terms. Upon substituting this ansatz into (7), we immediately get

$$(-\lambda\nabla_{\mathrm{h}}^2 + m)\tilde{\psi} = m|\alpha|\left\{\mathcal{B}\nabla_{\mathrm{h}}^2 - \frac{\mathrm{d}^2[\mathcal{B}(1 - \mu^2)]}{\mathrm{d}\mu^2}\right\}\left[\frac{\mathrm{sgn}(\alpha)\tilde{a}}{\sqrt{\rho_0\mu_{\mathrm{m}}}}\right]\,, \tag{8a}$$

$$-\lambda\left[\frac{\mathrm{sgn}(\alpha)\tilde{a}}{\sqrt{\rho_0\mu_{\mathrm{m}}}}\right] = m|\alpha|\mathcal{B}\tilde{\psi}\,, \tag{8b}$$

in which $\nabla_{\mathrm{h}}^2 \equiv R_0^2\nabla_{\mathrm{H}}^2$ is the dimensionless horizontal Laplacian. From now on, our interest is limited to the case where $m \neq 0$. The above equations are easily transformed into a single ordinary differential equation in the form

$$\frac{\mathrm{d}}{\mathrm{d}\mu}\left[\Lambda(1 - \mu^2)\frac{\mathrm{d}\tilde{\psi}}{\mathrm{d}\mu}\right] - \left\{\frac{m^2\Lambda}{1 - \mu^2} + m\left[\lambda + 2m\alpha^2\mathcal{B}\frac{\mathrm{d}(\mathcal{B}\mu)}{\mathrm{d}\mu}\right]\right\}\tilde{\psi} = 0\,, \tag{9}$$

where the factor $\Lambda(\mu) \equiv \lambda^2 - m^2\alpha^2\mathcal{B}^2$ is crucial to our problem. If there exist real values $\mu$ which satisfy $\Lambda(\mu) = 0$ within the interval $-1 < \mu < 1$, which are hereinafter denoted by $\mu_{\mathrm{c}}$, those points are interior poles depending on $\lambda$. The poles yield continuous spectra, as we stated in the introduction section. On the other hand, the Malkus field $\mathcal{B} = 1$ obviously produces no singular points except for the endpoints $\mu = \pm 1$. Dividing (9) by the factor $\Lambda\ (\neq 0)$, one can obtain its dispersion relation (1) without any hurdles because (9) is then reduced to the associated Legendre differential equation. Note that if $\lambda$ and $\tilde{\psi}$ are an eigenvalue and its corresponding eigenfunction of (9), respectively, the same holds true for their complex conjugates.

The existence of continuous spectra can be justified when the function $\Lambda$ has zeros in $-1 < \mu < 1$. Since (9) is a second-order differential equation, it should have two linearly independent solutions. Let $\tilde{\psi}_{\mathrm{I}}$ be the non-singular one of the solutions, and let the other be expressed in the form $\tilde{\Psi}_{\mathrm{II}} = \tilde{\psi}_{\mathrm{I}}\int^\mu f(\mu_*)\mathrm{d}\mu_*$ with a function $f(\mu)$. Substituting the form of $\tilde{\Psi}_{\mathrm{II}}$ into (9), we find

$$\tilde{\psi} = C_{\mathrm{I}}\tilde{\psi}_{\mathrm{I}} + C_{\mathrm{II}}\tilde{\Psi}_{\mathrm{II}}\,, \qquad \tilde{\Psi}_{\mathrm{II}}(\mu) = \tilde{\psi}_{\mathrm{I}}(\mu)\int^\mu\frac{\mathrm{d}\mu_*}{(1 - \mu_*^2)\Lambda(\mu_*)\tilde{\psi}_{\mathrm{I}}^2(\mu_*)}\,, \tag{10}$$

6

with both $C_{\mathrm{I}}$ and $C_{\mathrm{II}}$ being constants. Let us examine what the integral becomes if the interval of integration in (10) pass over zeros of $\Lambda$ (we assume that $\tilde{\psi}_{\mathrm{I}}^2 \neq 0$ within the interval). With an arbitrary starting point $\mu_0$ of the integration interval (in the following equation, we suppose that $\mu_0 < \min(\mu, \mu_{\mathrm{c}})$ and that at most one singular point exists between $\mu_0$ and $\mu$), we can express the second solution of the linearly independent set as the improper integral

$$
\tilde{\Psi}_{\mathrm{II}}(\mu) = \begin{cases} \tilde{\psi}_{\mathrm{I}}(\mu) \displaystyle\int_{\mu_0}^{\mu} \frac{\mathrm{d}\mu_*}{(1 - \mu_*^2)\Lambda(\mu_*)\tilde{\psi}_{\mathrm{I}}^2(\mu_*)} & (\mu < \mu_{\mathrm{c}}) \\[4mm] \tilde{\psi}_{\mathrm{I}}(\mu) \left[ \displaystyle\lim_{\Delta_1 \to +0} \int_{\mu_0}^{\mu_{\mathrm{c}}-\Delta_1} \frac{\mathrm{d}\mu_*}{(1 - \mu_*^2)\Lambda(\mu_*)\tilde{\psi}_{\mathrm{I}}^2(\mu_*)} \\[4mm] \qquad + \displaystyle\lim_{\Delta_2 \to +0} \int_{\mu_{\mathrm{c}}+\Delta_2}^{\mu} \frac{\mathrm{d}\mu_*}{(1 - \mu_*^2)\Lambda(\mu_*)\tilde{\psi}_{\mathrm{I}}^2(\mu_*)} \right] & (\mu_{\mathrm{c}} < \mu) \end{cases} . \tag{11}
$$

We may then deduce from (11) that (10) is also written as

$$
\tilde{\psi} = C_{\mathrm{I}}\tilde{\psi}_{\mathrm{I}} + C_{\mathrm{II}}\tilde{\psi}_{\mathrm{II}} + \tilde{\psi}_{\mathrm{I}} \sum_i C_{\mathrm{III},i} \mathrm{H}(\mu - \mu_{\mathrm{c},i}) , \tag{12a}
$$

where the integer $i$ is the index of the singular latitudes and $\mathrm{H}(\mu)$ is the step function. In addition, we have introduced the new second solution

$$
\tilde{\psi}_{\mathrm{II}}(\mu) \equiv \tilde{\psi}_{\mathrm{I}}(\mu) \, \mathcal{P} \int^{\mu} \frac{\mathrm{d}\mu_*}{(1 - \mu_*^2)\Lambda(\mu_*)\tilde{\psi}_{\mathrm{I}}^2(\mu_*)} , \tag{12b}
$$

in which $\mathcal{P}$ denotes the Cauchy principal value. In the vicinity of $\mu = \mu_{\mathrm{c}}$, we know that $\mathcal{B}^2 = \mathcal{B}_{\mathrm{c}}^2 + (\mathcal{B}_{\mathrm{c}}^2)'(\mu - \mu_{\mathrm{c}}) + (\mathcal{B}_{\mathrm{c}}^2)''(\mu - \mu_{\mathrm{c}})^2/2 + (\mathcal{B}_{\mathrm{c}}^2)'''(\mu - \mu_{\mathrm{c}})^3/6 + \mathrm{O}(|\mu - \mu_{\mathrm{c}}|^4)$, where $\mathcal{B}_{\mathrm{c}}^2 \equiv \mathcal{B}^2(\mu_{\mathrm{c}}) = \lambda^2/m^2\alpha^2$, $(\mathcal{B}_{\mathrm{c}}^2)' \equiv (\mathrm{d}\mathcal{B}^2/\mathrm{d}\mu)|_{\mu=\mu_{\mathrm{c}}}$ and the like. Now, in this paper, we will narrow down a target only to the case when $(\mathcal{B}_{\mathrm{c}}^2)'$ does not vanish. Using this series expansion, one obtains the magnitude $C_{\mathrm{III},i}$ of the discontinuities at the latitudes in the form

$$
C_{\mathrm{III},i} \equiv -\frac{C_{\mathrm{II}}I_i}{(1 - \mu_{\mathrm{c},i}^2)m^2\alpha^2(\mathcal{B}_{\mathrm{c},i}^2)'\tilde{\psi}_{\mathrm{I}}^2(\mu_{\mathrm{c},i})} \tag{12c}
$$

with the integral $I_i$ given by

$$
I_i \equiv \lim_{\Delta,\Delta_{1,i} \to +0} \int_{\mu_{\mathrm{c},i}-\Delta}^{\mu_{\mathrm{c},i}-\Delta_{1,i}} \frac{\mathrm{d}\mu_*}{\mu_* - \mu_{\mathrm{c},i}} + \lim_{\Delta,\Delta_{2,i} \to +0} \int_{\mu_{\mathrm{c},i}+\Delta_{2,i}}^{\mu_{\mathrm{c},i}+\Delta} \frac{\mathrm{d}\mu_*}{\mu_* - \mu_{\mathrm{c},i}} = \lim_{\Delta_{1,i},\Delta_{2,i} \to +0} \ln \frac{\Delta_{1,i}}{\Delta_{2,i}} . \tag{12d}
$$

This integral can be an arbitrary number, depending on how we take the limit $\Delta_{1,i}, \Delta_{2,i} \to +0$. Indeed, Van Kampen (1955) suggested that, in the problem of plasma oscillations, his counterpart of $I$ may be considered as an arbitrary parameter, which can be determined by a normalization condition of his counterpart of $\tilde{\psi}$, or the distribution function of plasma. As seen in (12a), the existence of these more than two linearly independent solutions despite (9) being a second-order differential equation can lead to an excess of arbitrary coefficients which should be adjusted to satisfy boundary conditions. This excessive freedom results in continuous spectra.

Another explanation for the appearance of continuous spectra is derived from the condition that should be satisfied by the solution of (9) in the vicinity of the singular point. On integrating (9) with respect to $\mu$ over the narrow range sandwiched between $\mu_{\mathrm{c}} - \Delta_1$ and $\mu_{\mathrm{c}} + \Delta_2$ with $\Delta_1, \Delta_2 \to +0$, one get

$$
\lim_{\Delta_1 \to +0} \Delta_1 \frac{\mathrm{d}\tilde{\psi}}{\mathrm{d}\mu}\bigg|_{\mu=\mu_{\mathrm{c}}-\Delta_1} + \lim_{\Delta_2 \to +0} \Delta_2 \frac{\mathrm{d}\tilde{\psi}}{\mathrm{d}\mu}\bigg|_{\mu=\mu_{\mathrm{c}}+\Delta_2} \to 0 , \tag{13a}
$$

provided that the condition

$$
\lim_{\Delta_1,\Delta_2 \to +0} \int_{\mu_{\mathrm{c}}-\Delta_1}^{\mu_{\mathrm{c}}+\Delta_2} |\tilde{\psi}|\mathrm{d}\mu \to 0 \tag{13b}
$$

is fulfilled. The fact that $\tilde{\psi}_{\mathrm{I}}$ is surely a solution for (9) and that $\tilde{\psi}_{\mathrm{I}}\mathrm{H}(\mu - \mu_{\mathrm{c}})$ always fulfills (13a) shows that the third term in (12a) is a weak solution for (9) and $C_{\mathrm{III}}$ should then be an undetermined parameter.

An alternative survey of their structures at the critical latitudes is conducted with the Frobenius method (e.g. Braun, 1975). Suppose that a power series of the form $\tilde{\psi}^{(c)} \equiv \sum_{k=0}^{\infty} a_k(\mu - \mu_c)^{k+\varrho}$ ($a_0 \neq 0$) is a solution for (9) around a critical latitude $\mu_c$, in which $\varrho$ is a root of the indicial equation for (9). On substituting this assumption for $\tilde{\psi}$ in (9), one obtains the equation $\varrho^2 = 0$ from its leading order term. As a result, the two linearly independent solutions near the latitude are given on the basis of the way to deal with the repeated root $\varrho = 0$ by

$$\tilde{\psi}_{\mathrm{I}}^{(c)} \equiv 1 + \sum_{k=1}^{\infty} a_k(\mu - \mu_c)^k, \tag{14a}$$

$$\tilde{\psi}_{\mathrm{II}}^{(c)} \equiv \tilde{\psi}_{\mathrm{I}}^{(c)} \ln|\mu - \mu_c| + \sum_{k=1}^{\infty} b_k(\mu - \mu_c)^k. \tag{14b}$$

Some of the expansion coefficients are found with slightly tedious but standard manipulations as $a_1 = D_1$, $a_2 = (D_1^2 + 2D_1 D_2 + D_3)/4$, $b_1 = -2D_1 + D_2$, $b_2 = (-3D_1^2 - 2D_1 D_2 + 2D_2^2 - D_3 + 2D_4)/4$, where

$$D_1 \equiv -\frac{\lambda/m\alpha^2 + 2\mathcal{B}_c^2 + (\mathcal{B}_c^2)'\mu_c}{(\mathcal{B}_c^2)'(1 - \mu_c^2)}, \quad D_2 \equiv \frac{2(\mathcal{B}_c^2)'\mu_c - (\mathcal{B}_c^2)''(1 - \mu_c^2)/2}{(\mathcal{B}_c^2)'(1 - \mu_c^2)},$$

$$D_3 \equiv \frac{m^2(\mathcal{B}_c^2)'/(1 - \mu_c^2) - 3(\mathcal{B}_c^2)' - (\mathcal{B}_c^2)''\mu_c}{(\mathcal{B}_c^2)'(1 - \mu_c^2)}, \quad D_4 \equiv \frac{(\mathcal{B}_c^2)' + (\mathcal{B}_c^2)''\mu_c - (\mathcal{B}_c^2)'''(1 - \mu_c^2)/6}{(\mathcal{B}_c^2)'(1 - \mu_c^2)}. \tag{15}$$

If one substitutes the first Frobenius solution $\tilde{\psi}_{\mathrm{I}}^{(c)}$ for $\tilde{\psi}_{\mathrm{I}}$ into the integral expression (12b) to calculate the second solution up to its second-order terms, the resulting expression certainly agrees with the second Frobenius one $\tilde{\psi}_{\mathrm{II}}^{(c)}$ up to the same order (strictly speaking, $\tilde{\psi}_{\mathrm{II}} \simeq -(\tilde{\psi}_{\mathrm{II}}^{(c)} + \mathrm{const.} \times \tilde{\psi}_{\mathrm{I}}^{(c)})/(1 - \mu_c^2)m^2\alpha^2(\mathcal{B}_c^2)'$ around the latitude). Accordingly, we can associate $\tilde{\psi}_{\mathrm{I}}$ with $\tilde{\psi}_{\mathrm{I}}^{(c)}$, and $\tilde{\psi}_{\mathrm{II}}$ with $\tilde{\psi}_{\mathrm{II}}^{(c)}$, in the vicinity of $\mu = \mu_c$. The series solutions (14) also justify (13b), since the term which becomes the largest contributor to the integral is $\int_{\mu_c-\Delta_1}^{\mu_c+\Delta_2} \ln|\mu - \mu_c|\mathrm{d}\mu$. The comparison between linear combinations of these linearly independent solutions and our numerical solutions will be shown in Section 3.2.

Necessary conditions for instability often receive interest from a lot of hydrodynamicists. As will be proved in Appendix A, one of the so-called semicircle theorems giving an eigenvalue bound in the current problem is written as

$$\left[\frac{\mathrm{Re}(\lambda)}{m} + \alpha^2 \max\left(2\mathcal{B}\frac{\mathrm{d}(\mathcal{B}\mu)}{\mathrm{d}\mu}\right)\right]^2 + \left(\frac{\mathrm{Im}(\lambda)}{m}\right)^2 \leq \alpha^4\left[\max\left(2\mathcal{B}\frac{\mathrm{d}(\mathcal{B}\mu)}{\mathrm{d}\mu}\right)\right]^2 - \alpha^2 \min(\mathcal{B}^2), \tag{16a}$$

only if $\mathrm{Im}(\lambda) \neq 0$. Additionally, we also find another bound for the case when $\mathrm{Im}(\lambda) \neq 0$ in the form

$$-\frac{1}{2m(m+1)} \leq \frac{\mathrm{Re}(\lambda)}{m} \leq 0. \tag{16b}$$

These relations mean that if unstable modes exist, they must propagate in the retrograde direction, and the value $\max\{2\mathcal{B}[\mathrm{d}(\mathcal{B}\mu)/\mathrm{d}\mu]\}$ concerning the gradient of an imposed magnetic field must be positive. Hughes and Tobias (2001); Mak *et al.* (2016), and Wang *et al.* (2022a,b) derived similar theorems for the MHD or MHD shallow water systems with a background shear flow. The theorem (16a) indicates that magnetic shear ascribed to the spherical geometry may have a destabilising effect. We were not, however, able to find out unstable modes that are likely to be physically meaningful when $\mathcal{B} = \mu$, as described in Section 3.

## 2.1 Numerical method

A numerical method to solve our eigenvalue problem is described now. In this article, we shall focus on the simplest equatorially-antisymmetric non-Malkus field $\mathcal{B} = \mu$. This choice prompts us to utilise the associated Legendre polynomial expansion, since (9) exactly becomes the associated Legendre differential equation if $\mathcal{B} = 1$ and recurrence formulae of these polynomials are useful in the present situation. For a fixed $m$, the polynomials $\mathrm{P}_n^m$ ($n \geq m$) constitute a basis for function expansion in the Galerkin discretization on a spherical surface. Thus, we have

$$\tilde{\psi}(\mu) \equiv \sum_{n=m}^{N_t} \tilde{\psi}^{[n]}\mathcal{N}_n^m\mathrm{P}_n^m(\mu), \quad \frac{\mathrm{sgn}(\alpha)\tilde{a}}{\sqrt{\rho_0\mu_m}} \equiv \sum_{n=m}^{N_t} \tilde{a}^{[n]}\mathcal{N}_n^m\mathrm{P}_n^m, \tag{17a}$$

where $N_t$ denotes the truncation degree and the normalising factor is written as

$$\mathcal{N}_n^m \equiv (-1)^m \sqrt{\frac{2n+1}{2} \frac{(n-m)!}{(n+m)!}} . \tag{17b}$$

Assuming (17a) to be an approximate solution for (8) and using useful relations in the forms

$$\nabla_h^2 P_n^m = -n(n+1)P_n^m , \tag{18a}$$

$$\mu P_n^m = \frac{n+m}{2n+1}P_{n-1}^m + \frac{n-m+1}{2n+1}P_{n+1}^m , \tag{18b}$$

and the orthogonality relation $\int_{-1}^{1} P_n^m P_\nu^m \mathrm{d}\mu = \delta_{n,\nu}/\mathcal{N}_n^m \mathcal{N}_\nu^m$ with the Kronecker delta $\delta_{n,\nu}$, we get the following simultaneous equations for all integers $n$ which satisfy $m \leq n \leq N_t$:

$$\left[\lambda + \frac{m}{n(n+1)}\right] \tilde{\psi}^{[n]} = -m|\alpha| \left[\frac{(n-3)(n+2)}{n(n+1)} k_n^m \tilde{a}^{[n-1]} + \frac{(n-1)(n+4)}{n(n+1)} k_{n+1}^m \tilde{a}^{[n+1]}\right] , \tag{19a}$$

$$\lambda \tilde{a}^{[n]} = -m|\alpha| \left(k_n^m \tilde{\psi}^{[n-1]} + k_{n+1}^m \tilde{\psi}^{[n-1]}\right) , \tag{19b}$$

in which the number sequence

$$k_n^m = \sqrt{\frac{(n-m)(n+m)}{(2n-1)(2n+1)}} \qquad (n = m, m+1, \ldots, N_t) , \tag{19c}$$

is introduced for convenience.

The system of linear equations (19) is equivalent to the eigenvalue problem for the corresponding $2(N_t - m + 1) \times 2(N_t - m + 1)$ matrix, and arrays of the expansion coefficients $\tilde{\psi}^{[n]}$ and $\tilde{a}^{[n]}$ are its eigenvectors. We performed numerical calculations solving this eigenvalue problem with our Python code which is based on the `numpy.linalg.eig` function of the NumPy library. In these calculations, the truncation number $N_t$ was set to 2000. As can be seen from (19), the subset of $\tilde{\psi}^{[n]}$ with $n$ being odd numbers pertains only to the subset of $\tilde{a}^{[n]}$ with $n$ being even, and the same is true of the relationship between $\tilde{\psi}^{[n]}$ with $n$ even and $\tilde{a}^{[n]}$ with $n$ odd. On the basis of this dichotomy, we refer to eigenmodes for which $\tilde{\psi}^{[n]}$'s are non-zero only when $n - m$ is even (in other words, $\tilde{a}^{[n]}$'s do not vanish only when $n - m$ is odd, and $u_\theta$, $b_\phi$ are equatorially-symmetric and $u_\phi$, $b_\theta$ are equatorially-antisymmetric) as the sinuous modes (cf. Márquez-Artavia et al., 2017). Conversely, eigenmodes for which $\tilde{\psi}^{[n]}$'s become non-zero only when $n - m$ is odd (or, $u_\theta$ is antisymmetric and $u_\phi$ is symmetric about the equator) are hereinafter referred to as the varicose modes.

The validity of eigenmodes obtained numerically is diagnosed from the aspect of convergence. This is conducted by evaluating

$$\sum_{n=m}^{\lfloor N_t/2 \rfloor} \left|\tilde{\psi}^{[n]}\right|^2 > 10^2 \sum_{n=\lfloor N_t/2 \rfloor+1}^{N_t} \left|\tilde{\psi}^{[n]}\right|^2 \quad \text{and} \quad \sum_{n=m}^{\lfloor N_t/2 \rfloor} \left|\tilde{a}^{[n]}\right|^2 > 10^2 \sum_{n=\lfloor N_t/2 \rfloor+1}^{N_t} \left|\tilde{a}^{[n]}\right|^2 , \tag{20}$$

where $\lfloor x \rfloor$ is the integer part of $x$. Only eigenmodes that pass the screening by this validation will be studied and illustrated in the results section.

Normalising the amplitudes of eigenmodes is valuable to those who want to understand their characteristics by comparing physical quantities such as energies. We employed the manner of normalization in which we let the mean total energies $\mathrm{MKE} + \mathrm{MME}$ of perturbations be $(\rho_0/8R_0^2)\mathrm{e}^{2\mathrm{Im}(\omega)t}$, where the mean kinetic and mean magnetic energies of an eigenmode are expressed as

$$\mathrm{MKE} \equiv \frac{1}{4\pi} \int_0^\pi \mathrm{d}\theta \int_0^{2\pi} \sin\theta \mathrm{d}\phi \frac{\rho_0 |\boldsymbol{u}_1|^2}{2} = \frac{\rho_0}{8R_0^2} \mathrm{e}^{2\mathrm{Im}(\omega)t} \sum_{n=m}^{N_t} n(n+1) \left|\tilde{\psi}^{[n]}\right|^2 , \tag{21a}$$

$$\mathrm{MME} \equiv \frac{1}{4\pi} \int_0^\pi \mathrm{d}\theta \int_0^{2\pi} \sin\theta \mathrm{d}\phi \frac{|\boldsymbol{b}_1|^2}{2\mu_m} = \frac{\rho_0}{8R_0^2} \mathrm{e}^{2\mathrm{Im}(\omega)t} \sum_{n=m}^{N_t} n(n+1) \left|\tilde{a}^{[n]}\right|^2 , \tag{21b}$$
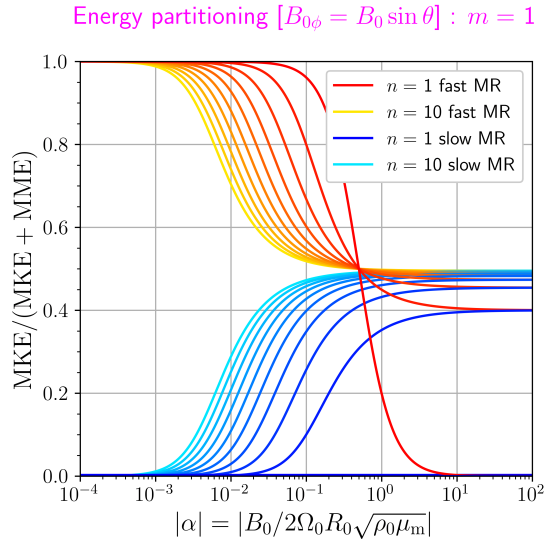
9

Figure 2: Ratio of the mean kinetic energy MKE to the mean total energy MKE + MME against the absolute value $|\alpha|$ of the Lehnert number when the zonal wavenumber $m = 1$ and the Malkus field is imposed. This plot is obtained from the relation MKE/(MKE + MME) = $\lambda^2/(\lambda^2 + m^2\alpha^2)$ in which the nondimensional angular frequency $\lambda$ is calculated by (1). As $|\alpha| \to 0$, either MKE or MME approaches zero, depending on whether the eigenmode is a slow or fast MR wave. The colours of the curves correspond to those in Figure 1.

respectively, with $\boldsymbol{u} = \varepsilon\boldsymbol{u}_1 + \mathrm{O}(\varepsilon^2)$ and $\boldsymbol{B} = \boldsymbol{B}_0 + \varepsilon\boldsymbol{b}_1 + \mathrm{O}(\varepsilon^2)$. The energy partitioning between MKE and MME allows us to examine the force balance of eigenmodes and to classify the types of waves. For instance, Figure 2 represents energy partitions for various eigenmodes under the Malkus field and shows that MKEs dominate the mean total energies for fast MR waves, MMEs are predominant over MKEs for slow MR waves, and Alfvén waves show almost equipartition between the two for large $|\alpha|$. This normalization of eigenvectors is applied to all the figures of profiles of eigenmodes displayed in the following sections. The associated Legendre polynomials $\mathrm{P}_n^m$ employed to construct the eigenfunctions from their corresponding eigenvectors are given by the `scipy.special.lpmv` function of the SciPy library.

# 3 Numerical results

The results section starts by presenting the dispersion relation for our current problem. Figure 3 shows the real parts of eigenfrequencies obtained numerically when $m = 1$ as functions of $|\alpha|$ (we find that their imaginary parts vanish, that is $\mathrm{Re}(\lambda) = \lambda$, for all the eigenmodes except for unreliable eigenmodes which will be slightly discussed later). The figure has four panels. The left and right columns show the retrograde and prograde modes, respectively, and the upper and lower rows show the sinuous and varicose modes, respectively. Each colour in the scatter plots represents the fraction of the mean kinetic energy within the mean total energy of an eigenmode corresponding to a point on the diagrams. Note that we used a nonlinear colour scale which is made by utilising the arctangent function so as to highlight whether an eigenmode is similar to the Alfvén wave (MKE $\approx$ MME; the colour of its marker is greenish) or not. To make it easier to find markers of modes dissimilar to the Alfvén wave (we chose the range MKE $< 0.49$ or $0.51 <$ MKE), we furthermore set the size of them to be larger than that of markers representing the Alfvén wave. On the basis of the knowledge learned from Figure 2, even in the present situation, we would be justified to think of an eigenmode whose marker in the figure is coloured reddish as a mode similar to the fast MR wave and a bluish one as a mode similar to the slow MR wave.

In all the panels, we can observe bands crowded with eigenmodes lying just below the lines $|\lambda| = m|\alpha|$. The kinetic and magnetic energies of most eigenmodes in the bands are partitioned almost equally. We conjecture that these bands should be identified with the continuous spectrum due to the Alfvén resonance, which is hereinafter referred to as the Alfvén continuous spectrum or Alfvén continuum, although our numerical method
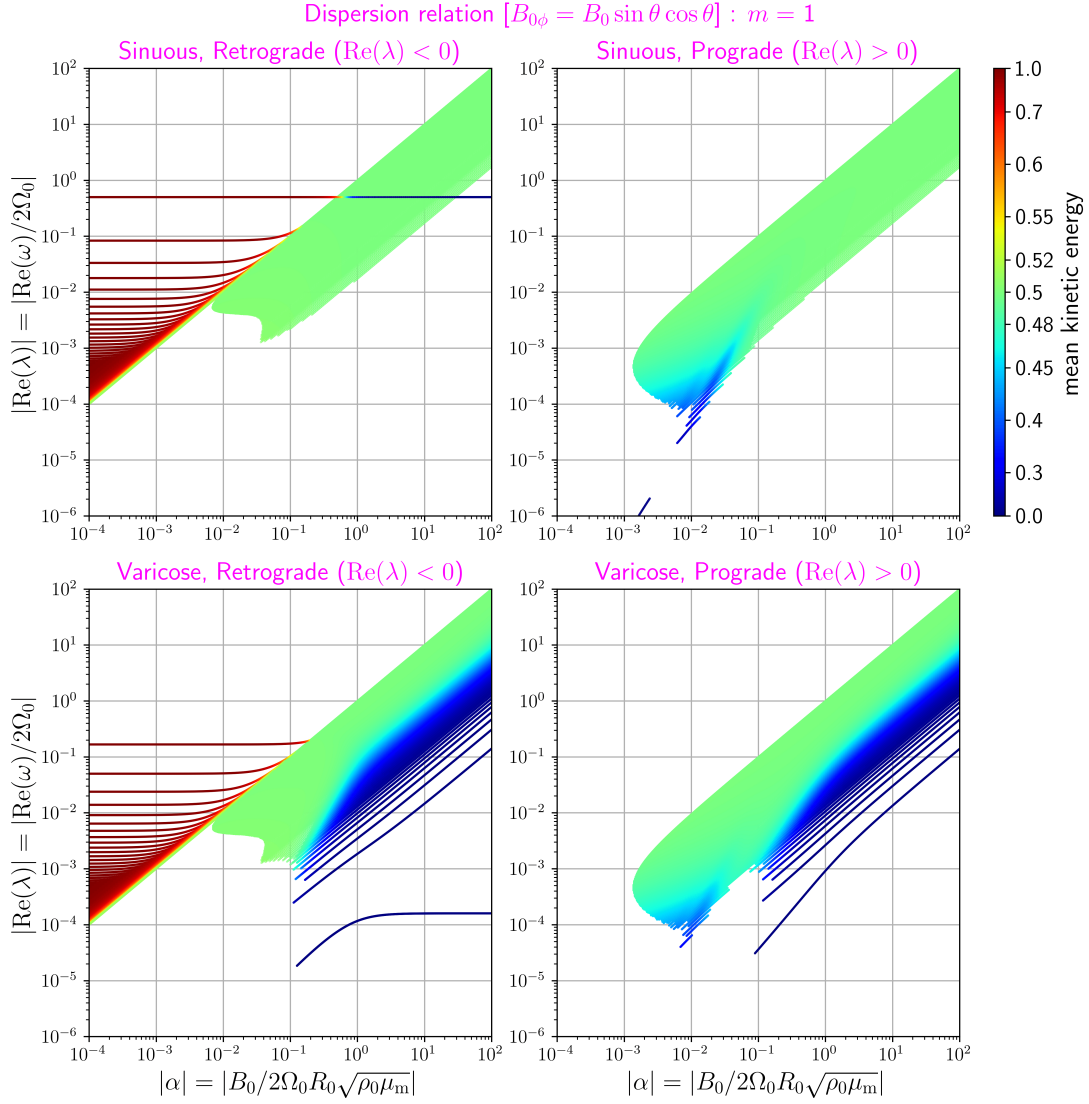
10

Figure 3: Dispersion diagrams when the zonal wavenumber $m = 1$ and the simplest equatorially-antisymmetric non-Malkus field $\mathcal{B} = \mu$ pervades the system. The ordinates of each panel represent the real part $\mathrm{Re}(\lambda)$ of the dimensionless angular frequency and the abscissas are the absolute value $|\alpha|$ of the Lehnert number. Retrograde modes ($\mathrm{Re}(\lambda) < 0$) are shown in the left column, and the right displays prograde modes ($\mathrm{Re}(\lambda) > 0$). The upper and lower rows illustrate sinuous and varicose modes, respectively. The colours of the markers represent the ratio of the mean kinetic energy MKE to the mean total energy MKE + MME.
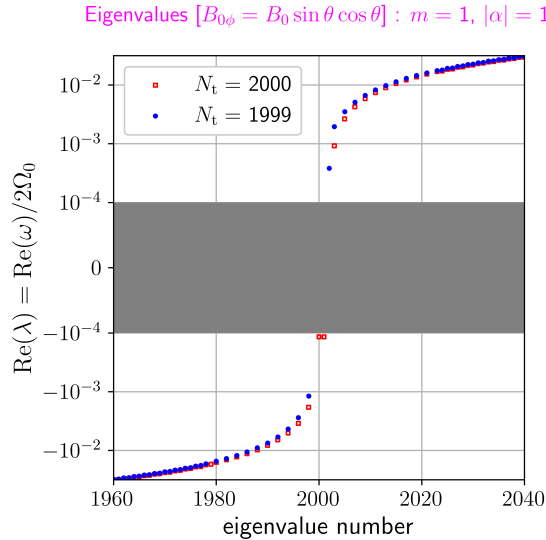
Eigenvalues $[B_{0\phi} = B_0 \sin\theta \cos\theta]$ : $m = 1$, $|\alpha| = 1$



Figure 4: Dependence of the real parts $\mathrm{Re}(\lambda)$ of eigenvalues on the truncation degree $N_\mathrm{t}$ when the zonal wavenumber $m = 1$, the absolute value of the Lehnert number $|\alpha| = 1$, and the background field is the simplest equatorially-antisymmetric non-Malkus one ($\mathcal{B} = \mu$). The horizontal axis is the eigenvalue number when eigenvalues are arranged in ascending order. The red open squares and the blue circles represent the case when $N_\mathrm{t} = 2000$ and 1999, respectively.

yields only approximate discrete modes even when the system has a continuous spectrum. Even though the spectrum ought to cover the expected range $m|\alpha|\min(\mu) = -m|\alpha| \le \lambda \le m|\alpha| = m|\alpha|\max(\mu)$ without any gaps as explained in the previous sections, our eigenmodes satisfying (20) do not have eigenvalues smaller than some levels in terms of absolute values. This is because, in addition to the vertical axes of the panels being logarithmic scale, the critical latitudes $\mu_\mathrm{c} = \pm\lambda/m|\alpha|$ get close to the equator as $\lambda \to 0$ for a given $m$ and a given $|\alpha|$, a fine structure in its eigenfunction appearing around the equator. It is necessary to calculate with a higher truncation degree in order for (17a) to express such a fine structure. Besides, small values of $|\alpha|$ ($\ll 1$) reduce typical meridional wavelengths of perturbations, as will be shown in Figure 9. It follows for the same reason as above that the bands are cut off below certain values of $|\alpha|$. If numerical calculations with an infinite degree were performed, obtained eigenvalues would cover the entire range below the line $|\lambda| = m|\alpha|$ completely. We also conducted calculations with truncation degrees somewhat lower than that of Figure 3, for example, $N_\mathrm{t} = 1000$ (not shown). The outlines of these dispersion diagrams look almost unchanged aside from the difference in the widths of the bands; the higher the truncation degree, the wider the band. In the lower panels of Figure 3, some branches of the retrograde modes look like discrete eigenvalues that lie below the bands. For these eigenmodes, MMEs are dominant. In particular, the lowermost two eigenvalues, whose branches overlap (since they are a complex conjugate pair, as mentioned in Section 2), in the lower left panel have non-zero imaginary parts (not shown), and their values are consistent with (16a) and (16b). However, we consider the branches including the unstable modes as unreliable eigenvalues, or a part of the Alfvén continuous modes, because the calculations (see also Figure 4) reveal that these eigenvalues depend strongly upon $N_\mathrm{t}$ as opposed to normal discrete modes (cf. Carpenter and Guha, 2019).

Discrete branches equivalent to slow MR waves found in Figure 1 disappear from Figure 3 as a result of the modification of the main field. Instead, the markers dyed blue, for which the fractions of MMEs of their eigenmodes are close to unity like slow MR waves, are distributed within the Alfvén continuum. Therefore, we suggest that discrete modes of slow MR waves turn into continuous ones under a non-Malkus field. This situation is similar to that of equatorial Rossby waves in Taniguchi and Ishiwatari (2006), who studied eigenmodes in a linear shear flow on an equatorial $\beta$-plane. An alternative explanation may be their transformation into quasi-modes (Spencer and Rasband, 1997; Schecter *et al.*, 2000; Balmforth *et al.*, 2001; Turner and Gilbert, 2007; Wang *et al.*, 2022a), or the Landau damping in a broad sense. When embedded in a continuous spectrum due to the replacement of basic fields, a discrete real eigenvalue (on the principle Riemann sheet) may change into a complex pole on the next Riemann sheet (e.g. Crawford and Hislop, 1989). Although this novel pole does not
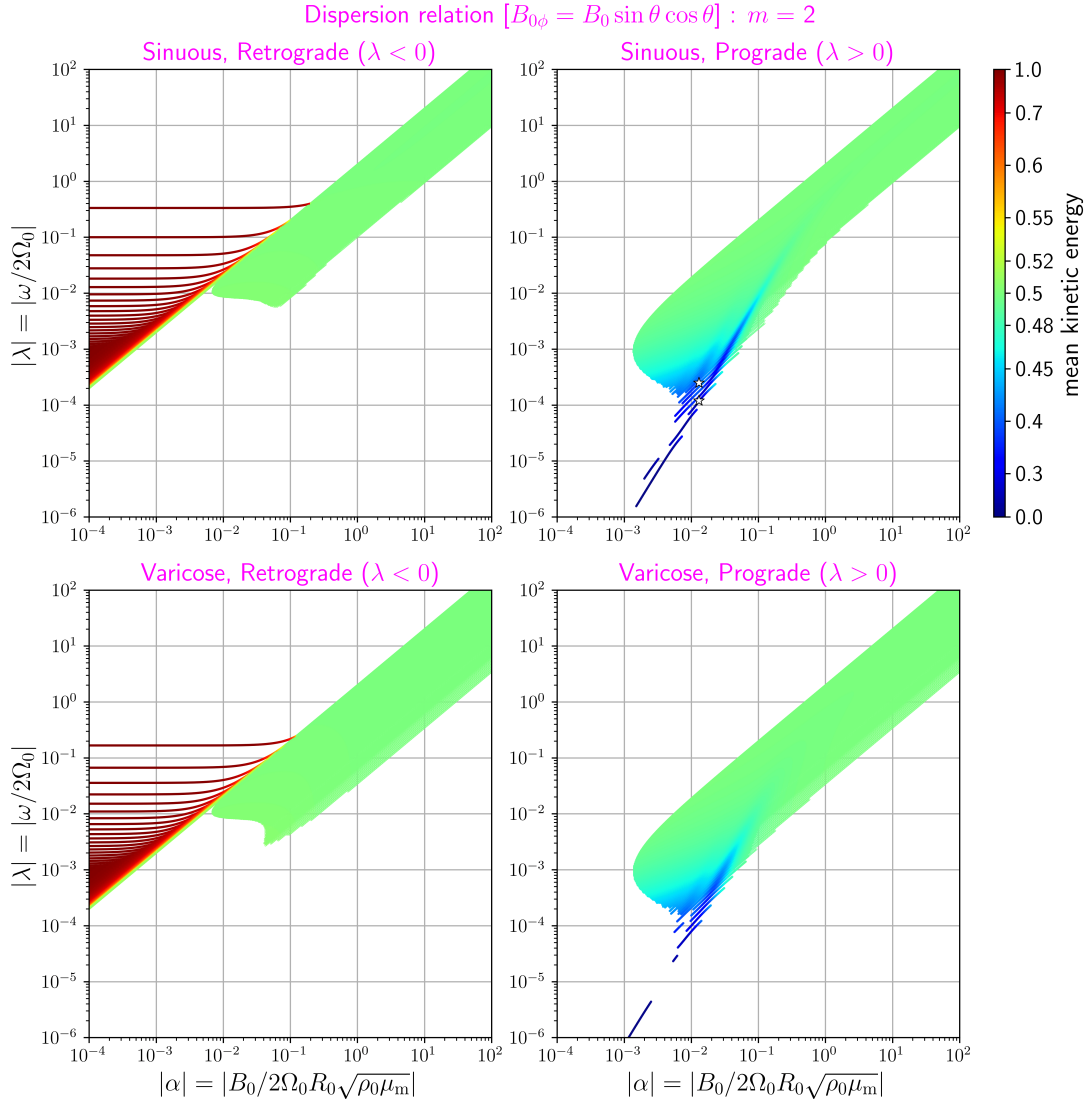
Figure 5: Same as Figure 3, but for $m = 2$. The two white asterisks of the upper right panel correspond to the two eigenmodes depicted in Figure 7.

produce a true eigenmode, it plays a crucial role in the time evolution of the system as a non-diffusive decaying oscillation whose frequency is close to the original real eigenvalue. We suspect that blue upward wedges with the approximate slope $\lambda \propto |\alpha|^2$ at $|\alpha| \approx 10^{-2}$ and $\lambda \approx 10^{-4}$ in the right panels of Figure 3 are connected with quasi-modes originating from slow MR waves. To confirm this, we are preparing a paper that gives the result of a treatment finding quasi-modes, which is described in the foregoing literature (e.g. Spencer and Rasband, 1997), different from our approach.

Outside the continuous spectrum, that is, above the lines $|\lambda| = m|\alpha|$ in the diagrams, fast MR waves remain discrete eigenmodes even in the non-Malkus field. Their semi-analytical solutions can be obtained from eigenvalues of the spheroidal differential equation to which (9) is reduced when $\mathcal{B} = \mu$ and $m^2\alpha^2/\lambda^2$ is small (see Appendix B). Additionally, we find that the lowest branch of the $m = 1$ sinuous modes of fast MR waves can penetrate the band of the continuous spectrum without interaction (see the upper left panel of Figure 3). This is because the Lorentz force does not act on this eigenmode. This mode is explained in detail in Appendix C.

Figure 5 depicts the dispersion diagrams for $m = 2$. They roughly epitomise the diagrams when $m \geq 3$ (not shown). Their outlines do not change much from those of Figure 3 with the exception of the absence of the branch of the fast MR waves that penetrates the continuous spectrum. Again, more conspicuous blue upward wedges exist around $10^{-2} \leq |\alpha| \leq 10^{-1}$ and $10^{-4} \leq \lambda \leq 10^{-2}$ in the right panels of Figure 5.
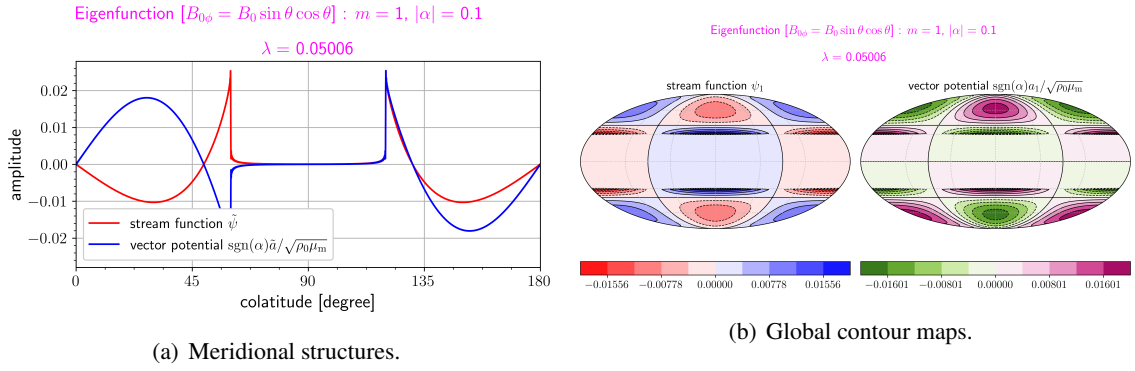
(a) Meridional structures.



(b) Global contour maps.

Figure 6: Eigenfunction of the sinuous mode with the nondimensional angular frequency $\lambda \approx 0.05006$ when the zonal wavenumber $m = 1$, the absolute value of the Lehnert number $|\alpha| = 0.1$, and the simplest equatorially-antisymmetric non-Malkus field $\mathcal{B} = \mu$ is imposed. The critical colatitudes $\theta_{\mathrm{c}} \approx 59.96°$ and $120.04°$. (a) Amplitudes of the stream function $\tilde{\psi}$ (red line) and the scaled magnetic vector potential $\mathrm{sgn}(\alpha)\tilde{a}/\sqrt{\rho_0 \mu_{\mathrm{m}}}$ (blue line) as functions of the colatitude. (b) Contour maps of the stream function $\psi_1$ (left panel) and the scaled magnetic vector potential $\mathrm{sgn}(\alpha)a_1/\sqrt{\rho_0 \mu_{\mathrm{m}}}$ (right panel) in the Mollweide projection.



(a) Sinuous mode with $\lambda \approx 0.00012$.



(b) Sinuous mode with $\lambda \approx 0.00025$.
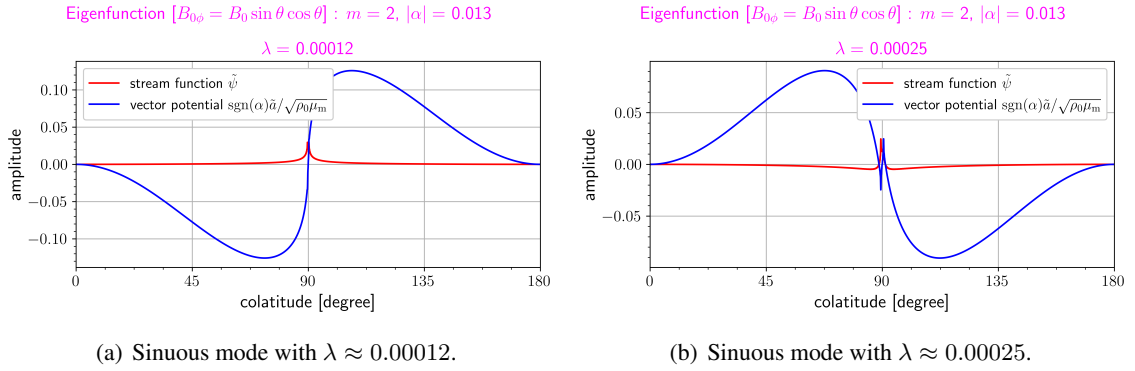
Figure 7: Same as Figure 6(a), but for $m = 2$, $|\alpha| = 0.013$.

## 3.1 Eigenfunctions of the Alfvén continuous modes

We shall investigate the eigenfunctions of the Alfvén continuous modes in this and the next subsections. Figure 6 shows typical structures of the perturbations in the stream function $\psi_1$ and the magnetic vector potential $a_1$ for the continuous modes. The dependences of their amplitudes $\tilde{\psi}$ and $\tilde{a}$ on the colatitude are illustrated in Figure 6(a), and are used for making the contour maps of Figure 6(b). From these figures, we notice that spiky singular structures appear at the critical latitudes of the eigenmode. As shown in Section 2, the eigenfunction has a logarithmic singularity or a step function singularity or both. In Section 3.2, we will provide the ratios of their contributions to the eigenfunctions around their corresponding critical latitudes. The eigenfunctions of eigenmodes which are extracted from each of the two noticeable blue upward wedges in the upper right panel of Figure 5 and which may have something to do with quasi-modes stemming from slow MR waves are also plotted in Figure 7.

To get the whole picture of the eigenfunctions of the continuous modes, we exhibit those of all the obtained continuous modes. Figures 8 and 9 are the heatmaps of the absolute values, or $|\tilde{\psi}|$ and $|\tilde{a}|$, of their amplitudes as functions of $\lambda$ and the colatitude when $|\alpha| = 0.1$ and $0.01$, respectively, and $m = 1$. The left columns in these figures correspond to $|\tilde{\psi}|$, and $|\tilde{a}|$ is depicted in their right ones. The sinuous and varicose modes are shown on the upper and lower rows, respectively. The colour gets darker as the absolute value increases. The maps indicate that the retrograde continuous modes are evanescent on the polar side of the critical latitudes, while the prograde ones are evanescent on the equatorial side. However, only the case in which $|\alpha|$ is sufficiently smaller than unity displays this behaviour (see Figure 10). Furthermore, the comparison between eigenmodes having the same value of $\lambda/m|\alpha|$ in Figures 8 and 9 shows that the smaller the value of $|\alpha|$ is, the smaller the

14

typical north-south wavelengths of their amplitudes. In Section 4, we will therefore examine the behaviour of wave packets possessing large wavenumbers at a small $|\alpha|$, which is similar to the Earth's core conditions, on the basis of the ray theory and attempt to get a better grasp of our numerical results.

For moderate or large values of $|\alpha|$, the less striking difference exists in the evanescent property between the retrograde and prograde modes which possess the same absolute value $|\lambda|$ of their angular frequency. This statement is based on Figure 10, which shows the heatmaps for $m = 1$ and $|\alpha| = 1$, and other experiments with several values of $m$ and $|\alpha|$ (not shown). Therefore, the contrast in the property between the retrograde and prograde modes as demonstrated in Figures 8 and 9 would be attributed to the planetary $\beta$ effect, that is, the effect of rotation. The ray-tracing analysis and the local dispersion relation which we are going to discuss in Section 4 offer a similar explanation. In addition, the fast MR mode buried in the continuous modes at $\lambda = -1/2$ is discernible in the upper panels of Figure 10 (see also Appendix C). In fact, we tried to utilise these plots as a means to discover buried discrete eigenmodes other than that, though no such eigenmodes have been found.

The evanescent property can be judged by the function

$$\mathcal{L}^2(\mu; m, \lambda) \equiv -m^2 - \frac{m(1 - \mu^2)}{\Lambda}\left[\lambda + 2m\alpha^2\mathcal{B}\frac{\mathrm{d}(\mathcal{B}\mu)}{\mathrm{d}\mu}\right] - \frac{1 - \mu^2}{2\sqrt{\Lambda}}\frac{\mathrm{d}}{\mathrm{d}\mu}\left(\frac{1 - \mu^2}{\sqrt{\Lambda}}\frac{\mathrm{d}\Lambda}{\mathrm{d}\mu}\right), \tag{22a}$$

which appears in an alternative form of the differential equation (9)

$$\frac{\mathrm{d}}{\mathrm{d}\mu}\left[(1 - \mu^2)\frac{\mathrm{d}(\tilde{\psi}\sqrt{\Lambda})}{\mathrm{d}\mu}\right] + \frac{\mathcal{L}^2}{1 - \mu^2}(\tilde{\psi}\sqrt{\Lambda}) = 0. \tag{22b}$$

The Mercator projection transformation $y = (1/2)\ln[(1 + \mu)/(1 - \mu)]$ yields a differential equation of the harmonic oscillation,

$$\frac{\mathrm{d}^2(\tilde{\psi}\sqrt{\Lambda})}{\mathrm{d}y^2} + \mathcal{L}^2(\tilde{\psi}\sqrt{\Lambda}) = 0, \tag{23a}$$

which shows that the sign of $\mathcal{L}^2$ determines the evanescent property of $\tilde{\psi}\sqrt{\Lambda}$ at the latitude. One can also rewrite (22b) into the form

$$\frac{\mathrm{d}^2[\tilde{\psi}\sqrt{(1 - \mu^2)\Lambda}]}{\mathrm{d}\mu^2} + \frac{\mathcal{L}^2 + 1}{(1 - \mu^2)^2}[\tilde{\psi}\sqrt{(1 - \mu^2)\Lambda}] = 0, \tag{23b}$$

which likewise shows that the value of $\mathcal{L}^2$ informs us of the evanescent property. The equivalent of this differential equation was derived by Gilman and Fox (1999a), though the form of $\mathcal{L}^2$ differs from theirs because their equation is based on a non-rotating frame; the partial derivatives with respect to $t$ in our equations have to be replaced by $(\partial/\partial t) + \Omega_0(\partial/\partial\phi)$ in the non-rotating frame. The left panel in Figure 11 shows contour plots of $\mathcal{L}^2$ as a function of $\lambda$ and the colatitude when $|\alpha| = 0.01$ and $\mathcal{B} = \mu$. We observe that the area where $\mathcal{L}^2 > 0$ (or $\mathcal{L}^2 > -1$) in the panel certainly agrees with the wavy regions in Figure 9. Now, we shall consider the case when $|\alpha|$ is small. Noting that $\lambda = \mathrm{O}(|\alpha|)$ and $|\Lambda| = \mathrm{O}(|\alpha|^2)$ for continuous modes, we have

$$\mathcal{L}^2 = -\frac{m(1 - \mu^2)}{\Lambda}\lambda + \mathrm{O}(|\Lambda|^{-2}|\alpha|^4) \tag{24}$$

unless the latitudinal position $\mu$ is very close to a critical latitude ($|\Lambda| \gg \mathrm{O}(|\alpha|^3)$), since $(\mathrm{d}\Lambda/\mathrm{d}\mu) = \mathrm{O}(|\alpha|^2)$ and $(\mathrm{d}^2\Lambda/\mathrm{d}\mu^2) = \mathrm{O}(|\alpha|^2)$ as can be seen from the definition of the function $\Lambda$. When $\mathcal{B} = \mu$ (and $|\mu^2 - \lambda^2/m^2\alpha^2| \gg \mathrm{O}(|\alpha|)$), the oscillatory condition $\mathcal{L}^2 > 0$ on the equatorial side ($\mu^2 < \lambda^2/m^2\alpha^2$) of the critical latitudes, therefore, requires that $\lambda < 0$ (the retrograde continuous modes), and $\mathcal{L}^2 > 0$ on the polar side ($\mu^2 > \lambda^2/m^2\alpha^2$) for the prograde modes ($\lambda > 0$). This explains the contrasting evanescent behaviour between the retrograde and prograde continuous modes for a small value of $|\alpha|$.

## 3.2 Comparison of the numerical results with the Frobenius series solutions

Here, we confirm that the eigenfunctions obtained numerically can be approximated by linear combinations of the linearly independent Frobenius series solutions (14). Let $\tilde{\psi}_{\mathrm{num}}$ be one of the numerical stream functions,
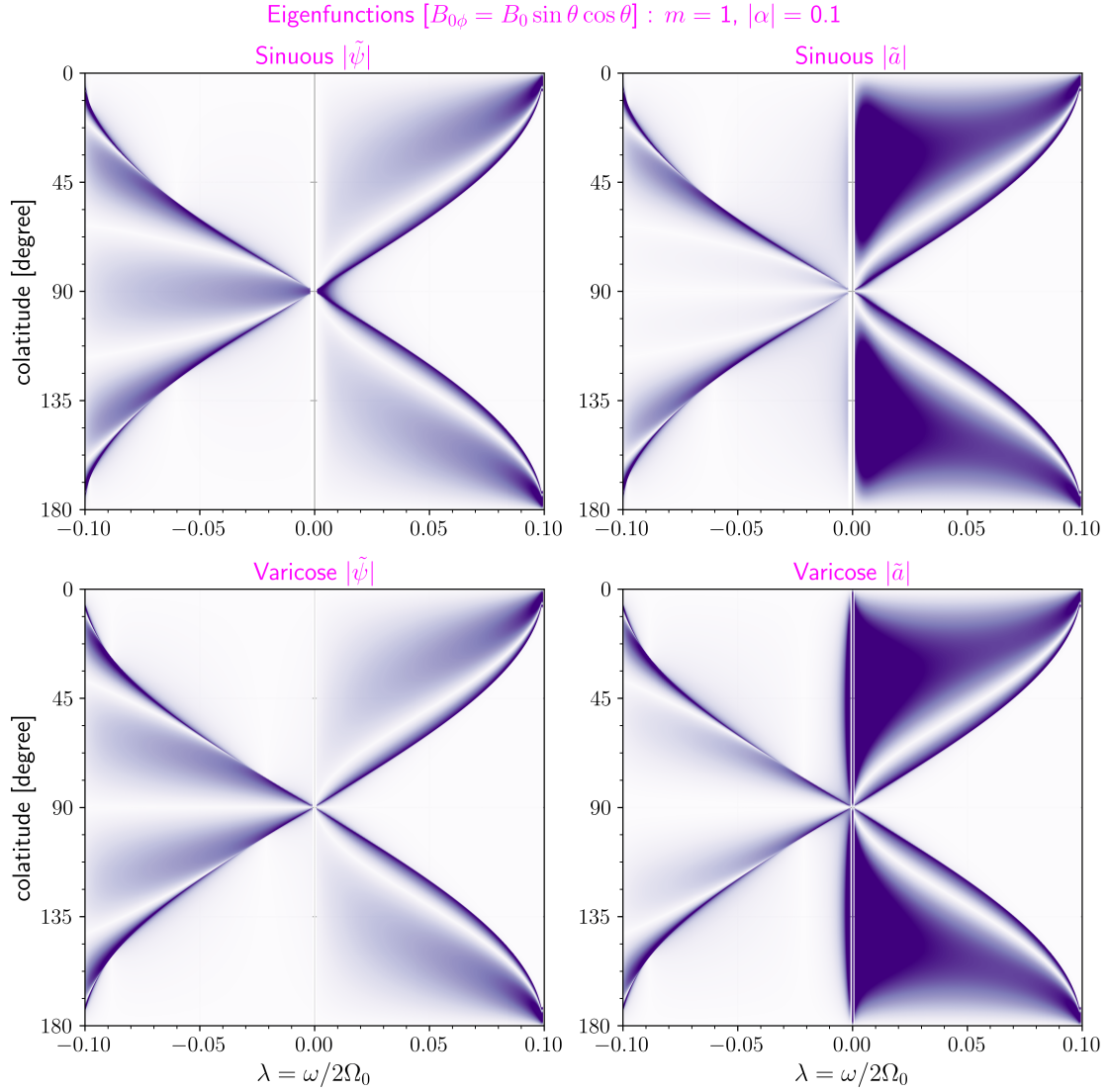
Figure 8: Amplitudes of the eigenfunctions of all the obtained continuous modes when the zonal wavenumber $m = 1$, the absolute value of the Lehnert number $|\alpha| = 0.1$, and the basic field is the simplest equatorially-antisymmetric non-Malkus one ($\mathcal{B} = \mu$). The four panels divide into the stream function and the magnetic vector potential on the left and the right columns, respectively, and sinuous and varicose modes on the upper and lower rows, respectively. The vertical axes of each panel correspond to the colatitude and the horizontal axes represent the nondimensional angular frequency $\lambda$. The darker the shades of the colour, the higher the absolute values $|\tilde{\psi}|$ and $|\tilde{a}|$ of the amplitudes of the stream function and the magnetic vector potential.
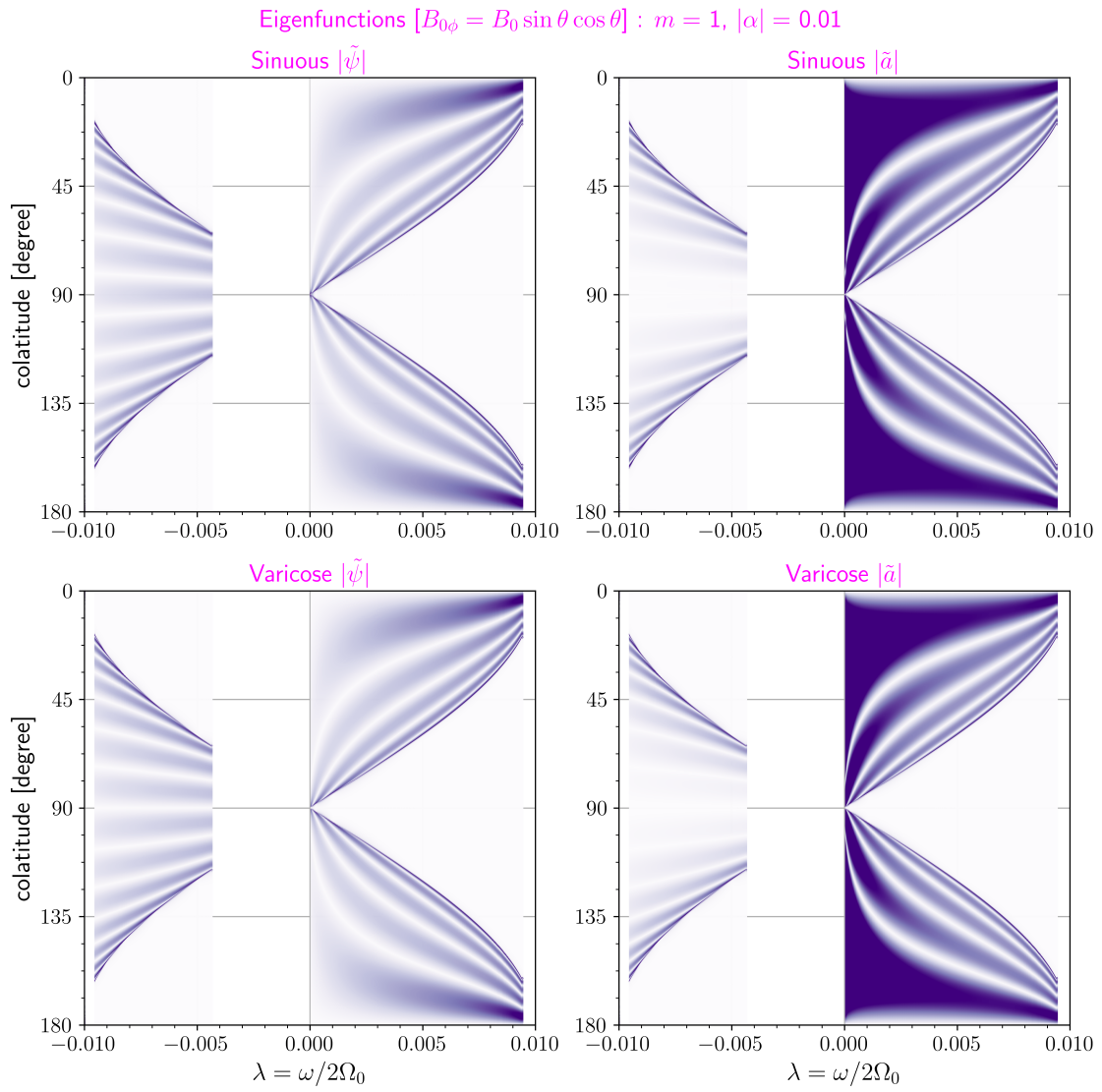
Figure 9: Same as Figure 8, but for $|\alpha| = 0.01$.

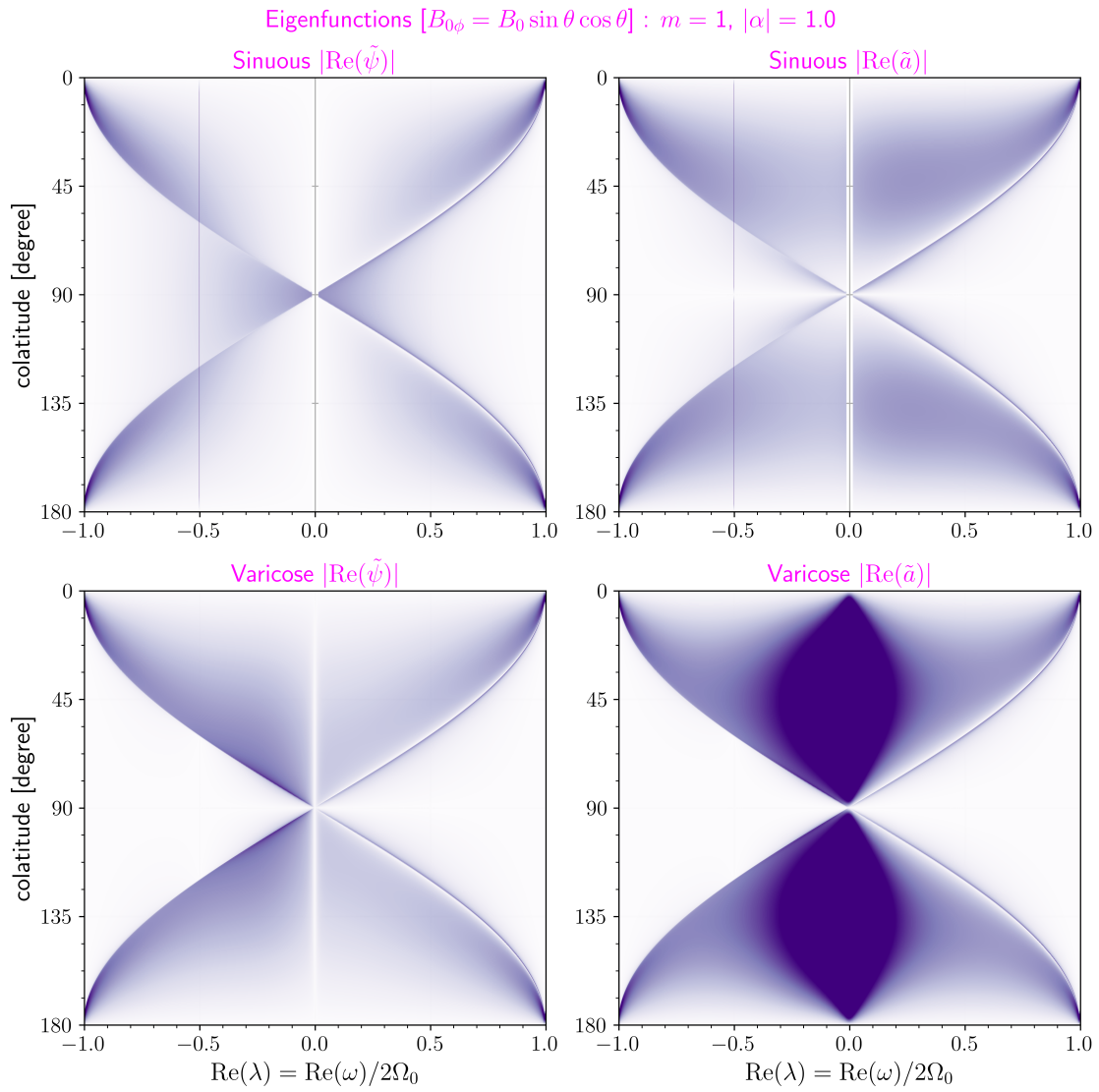Eigenfunctions $[B_{0\phi} = B_0 \sin\theta\cos\theta]$ : $m = 1$, $|\alpha| = 1.0$

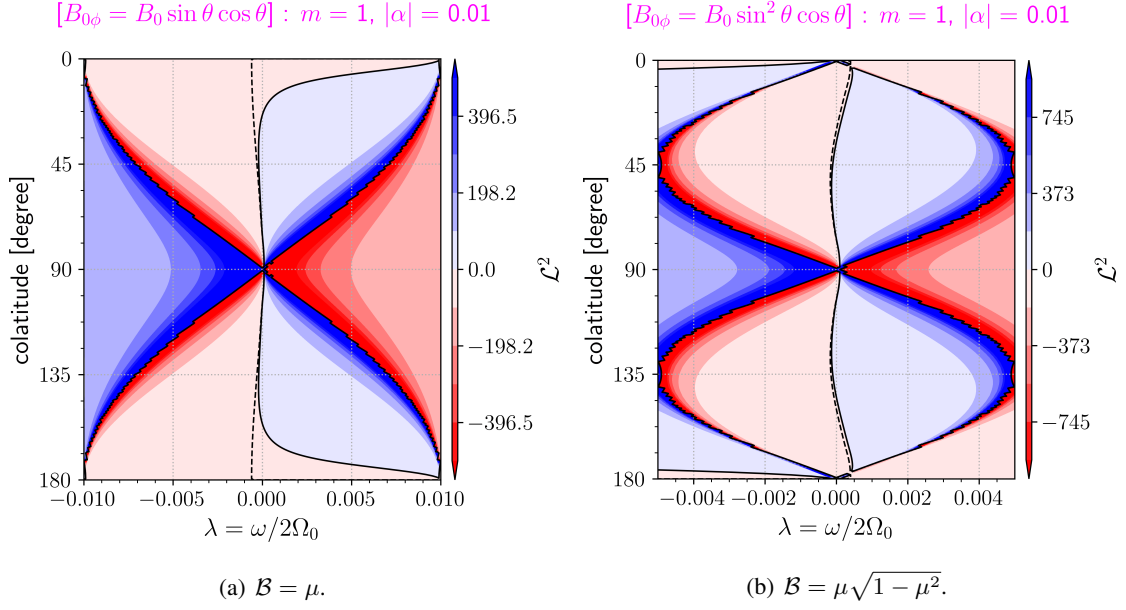Figure 10: Same as Figure 8, but for $m = 1$ and $|\alpha| = 1$.

Figure 11: Dependence of the function $\mathcal{L}^2$ given by (22a) on the nondimensional angular frequency $\lambda$ and the colatitude when the zonal wavenumber $m = 1$, the absolute value of the Lehnert number $|\alpha| = 0.01$, and the basic fields are (a) $\mathcal{B} = \mu$ and (b) $\mathcal{B} = \mu\sqrt{1-\mu^2}$. The solid and dashed curves illustrate the contour lines which correspond to $\mathcal{L}^2 = 0$ and $-1$, respectively.

and we fit it into the form $C_{\mathrm{I}}\tilde{\psi}_{\mathrm{I}}^{(c)} + C_{\mathrm{II}}\tilde{\psi}_{\mathrm{II}}^{(c)}$ by adjusting the coefficients $C_{\mathrm{I}}$ and $C_{\mathrm{II}}$ on each side of the critical latitudes. The fitting procedure is as follows. The colatitude ($0 \leq \theta \leq \pi$) is divided into $N_\theta$ points at even intervals. On each side of the nearest point of a singular latitude, the $N_{\mathrm{data}}$ points closest to the point are chosen among the $N_\theta$ points for the fitting. For these points $\theta_i$ ($1 \leq i \leq N_{\mathrm{data}}$) either on the equatorial or polar sides, we may write

$$\frac{\tilde{\psi}_{\mathrm{num}}(\cos\theta_i)}{\tilde{\psi}_{\mathrm{I}}^{(c)}(\cos\theta_i)} \approx C_{\mathrm{II}}\frac{\tilde{\psi}_{\mathrm{II}}^{(c)}(\cos\theta_i)}{\tilde{\psi}_{\mathrm{I}}^{(c)}(\cos\theta_i)} + C_{\mathrm{I}} \quad \text{and} \quad \frac{\tilde{\psi}_{\mathrm{num}}(\cos\theta_i)}{\tilde{\psi}_{\mathrm{II}}^{(c)}(\cos\theta_i)} \approx C_{\mathrm{I}}\frac{\tilde{\psi}_{\mathrm{I}}^{(c)}(\cos\theta_i)}{\tilde{\psi}_{\mathrm{II}}^{(c)}(\cos\theta_i)} + C_{\mathrm{II}}. \tag{25}$$

Now, $\tilde{\psi}_{\mathrm{I}}^{(c)}$ and $\tilde{\psi}_{\mathrm{II}}^{(c)}$ are approximated by the second-order Frobenius solutions with (15). We obtain a candidate value for each of $C_{\mathrm{I}}$ and $C_{\mathrm{II}}$ from each equation, through least squares fittings of (25) with the `numpy.polyfit` function of the NumPy library. Thereby we have four candidate values for each of $C_{\mathrm{I}}$ and $C_{\mathrm{II}}$ for one critical latitude, two from the equatorial side, and two from the polar side. The upper panels of Figure 12 show a result when we perform this procedure with $N_\theta = 7201$, and $N_{\mathrm{data}} = 200$ individually for the equatorial (red circles and solid lines) and the polar (blue circles and dashed lines) sides. These fittings demonstrate that $C_{\mathrm{I}}$ typically has different values ($C_{\mathrm{I}}^{(e)}$ and $C_{\mathrm{I}}^{(p)}$, say) between the two sides of a critical latitude, whilst $C_{\mathrm{II}}$ has the same value on both sides. Since $C_{\mathrm{III}}$ in (12a) can also be written as $\mathrm{sgn}(\mu_c)[C_{\mathrm{I}}^{(p)} - C_{\mathrm{I}}^{(e)}]$, our numerical eigenmodes are consistent with the general results as described in Section 2. We accordingly adopt the mean values of the two candidate values for each of $C_{\mathrm{I}}^{(e)}$ and $C_{\mathrm{I}}^{(p)}$ and four candidate ones of $C_{\mathrm{II}}$ ($C_{\mathrm{II}}^{(e)} = C_{\mathrm{II}}^{(p)}$) as their definite values, which are used in the graph comparing $\tilde{\psi}_{\mathrm{num}}$ with $C_{\mathrm{I}}\tilde{\psi}_{\mathrm{I}}^{(c)} + C_{\mathrm{II}}\tilde{\psi}_{\mathrm{II}}^{(c)}$ (the lower panel of Figure 12).

The above procedure is also applied to all the continuous modes obtained from our numerical calculations. Figure 13 depicts their values of $\mathrm{sgn}(\mu_c)[C_{\mathrm{I}}^{(p)} - C_{\mathrm{I}}^{(e)}]$ ($= C_{\mathrm{III}}$, red circles) and $C_{\mathrm{II}}$ (blue circles) for $m = 1$ and $|\alpha| = 0.1$ in the left ordinates as functions of $\lambda$. Their results for the sinuous and varicose modes are shown in the left and right panels, respectively. Meanwhile, the right vertical axes of these panels represent the numerical counterpart of (12d), which is written in the present instance as

$$I_{\mathrm{num}} \equiv -\mathrm{sgn}(\mu_c)\frac{C_{\mathrm{I}}^{(p)} - C_{\mathrm{I}}^{(e)}}{C_{\mathrm{II}}}(1-\mu_c^2)m^2\alpha^2(\mathcal{B}_c^2)'\left[\tilde{\psi}_{\mathrm{I}}^{(c)}(\mu_c)\right]^2. \tag{26}$$

This outcome demonstrates that the values of $I_{\mathrm{num}}$ appear to be compatible with our expectation stated in
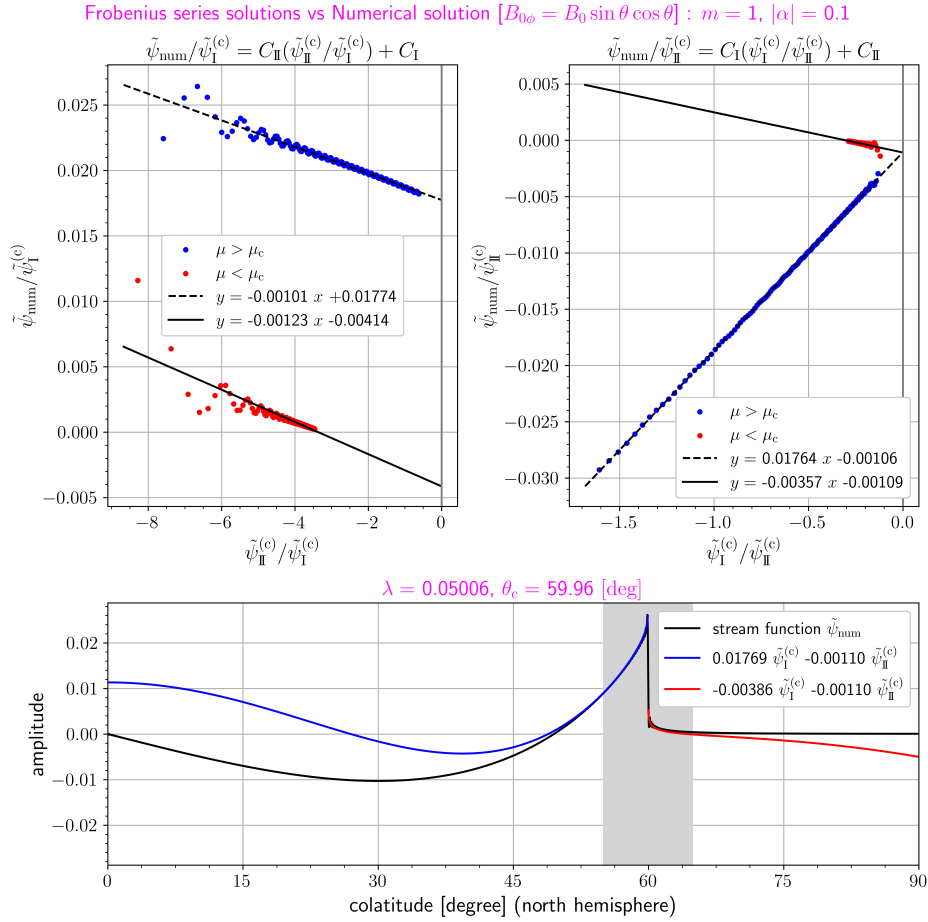
Figure 12: Comparison between the numerical eigenfunction $\tilde{\psi}_{\text{num}}$ of the sinuous mode with the dimensionless angular frequency $\lambda \approx 0.05006$ (the critical latitude $\theta_{\text{c}} = 59.96°$ in the north hemisphere) and linear combinations $C_{\text{I}}\tilde{\psi}_{\text{I}}^{(\text{c})} + C_{\text{II}}\tilde{\psi}_{\text{II}}^{(\text{c})}$ of the Frobenius series solutions (14) with (15) when the zonal wavenumber $m = 1$, the absolute value of the Lehnert number $|\alpha| = 0.1$, and the simplest equatorially-antisymmetric non-Malkus field $\mathcal{B} = \mu$ permeates the system. The undetermined coefficients $C_{\text{I}}$ and $C_{\text{II}}$ are estimated from least squares fittings of $\tilde{\psi}_{\text{num}}/\tilde{\psi}_{\text{I}}^{(\text{c})} = C_{\text{II}}(\tilde{\psi}_{\text{II}}^{(\text{c})}/\tilde{\psi}_{\text{I}}^{(\text{c})}) + C_{\text{I}}$ (upper left panel) and $\tilde{\psi}_{\text{num}}/\tilde{\psi}_{\text{II}}^{(\text{c})} = C_{\text{I}}(\tilde{\psi}_{\text{I}}^{(\text{c})}/\tilde{\psi}_{\text{II}}^{(\text{c})}) + C_{\text{II}}$ (upper right panel) with $N_{\text{data}} = 200$ points on the equatorial (red circles and solid lines) and the polar (blue circles and dashed lines) sides of the critical latitude for $N_{\theta} = 7201$. The lower panel shows $\tilde{\psi}_{\text{num}}$ (black curve) and $C_{\text{I}}\tilde{\psi}_{\text{I}}^{(\text{c})} + C_{\text{II}}\tilde{\psi}_{\text{II}}^{(\text{c})}$ with $C_{\text{I}}$ and $C_{\text{II}}$ determined by the fittings (red and blue curves) as functions of the colatitude. The vertical grey shaded area of this panel contains the $2N_{\text{data}} = 400$ points used in the fittings.
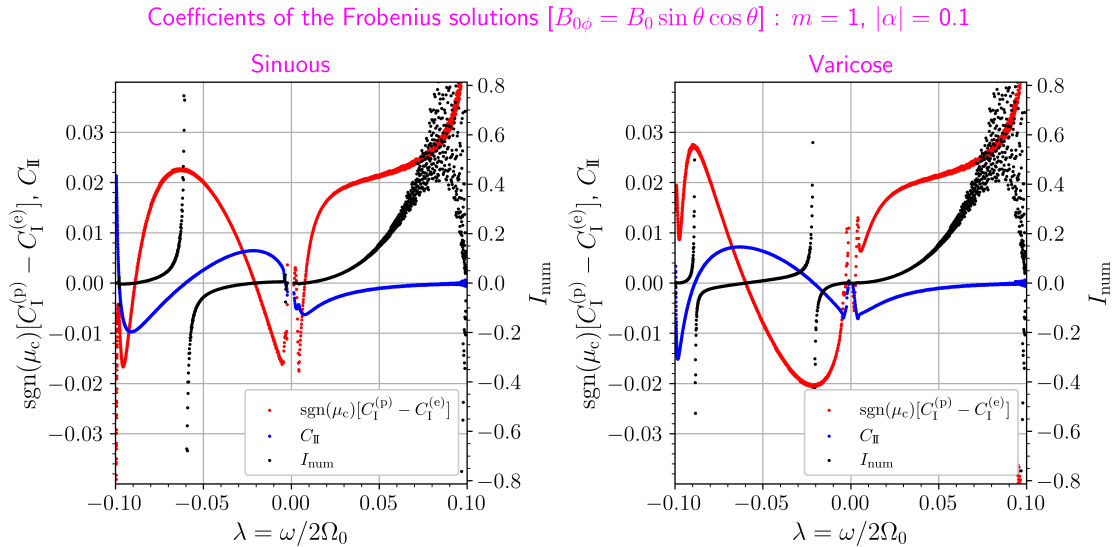
Figure 13: Values of $\mathrm{sgn}(\mu_{\mathrm{c}})[C_{\mathrm{I}}^{(\mathrm{p})} - C_{\mathrm{I}}^{(\mathrm{e})}]$ (red circles and the left vertical axes), $C_{\mathrm{II}}$ (blue circles and the left vertical axes), and $I_{\mathrm{num}}$ defined as (26) (black circles and the right vertical axes), relevant to the coefficients of the Frobenius series solutions against the nondimensional angular frequency $\lambda$. The case when the zonal wavenumber $m = 1$, the absolute value of the Lehnert number $|\alpha| = 0.1$, and the simplest equatorially-antisymmetric non-Malkus field $\mathcal{B} = \mu$ is imposed is shown in the left and the right panels for sinuous and varicose modes, respectively. $N_\theta$ and $N_{\mathrm{data}}$ are set to 7201 and 200, respectively, in the same way as Figure 12.

Section 2; the values are arbitrary numbers and adjusted to satisfy boundary conditions. In addition, we observe that the value of $\mathrm{sgn}(\mu_{\mathrm{c}})[C_{\mathrm{I}}^{(\mathrm{p})} - C_{\mathrm{I}}^{(\mathrm{e})}]$ vanishes at the extremum points of $C_{\mathrm{II}}$, and that $\mathrm{sgn}(\mu_{\mathrm{c}})[C_{\mathrm{I}}^{(\mathrm{p})} - C_{\mathrm{I}}^{(\mathrm{e})}]$ has extremums at the zeros of $C_{\mathrm{II}}$. If discrete eigenmodes without logarithmic and step function singularities are buried in the continuum, the two values must simultaneously vanish.

## 4 Interpretation in terms of the ray theory and discussion

To further comprehend the continuous modes and their eigenfunctions, we here reduce the system investigated so far to a more restricted situation when $|\alpha| \ll 1$. We apply the ray theory, in which an inhomogeneous background field varies with a much larger spatial scale than typical wavelengths. We introduce local coordinates $(\Theta, \Phi)$ which suitably measure the spatial scale size of the typical wavelength of a wave train. Introducing small parameters helps incorporate such a setting into governing equations. In Section 3.1, we found that typical meridional wavelengths decrease as the value of $|\alpha|$ decreases. Thus, it would be reasonable to select $|\alpha|$ as the parameter, if the value of $|\alpha|$ is sufficiently smaller than unity. The local coordinates are then stretched in the forms

$$\Theta \equiv |\alpha|^{-1/2}\theta, \qquad \Phi \equiv |\alpha|^{-1/2}\phi. \tag{27a}$$

The temporal scale of the wave period ($\lambda^{-1} = \mathrm{O}(|\alpha|^{-1/2})$) is similarly far from that of the migration of the wave train. The new shrunk time $T$ useful in measuring the latter is given by

$$T \equiv |\alpha|\tau. \tag{27b}$$

The values of the exponents of $|\alpha|$ of the variables above are determined in Appendix D.

We then introduce a locally defined wavenumber and angular frequency which depend on the global coordinates $(\theta, \phi)$ and $T$, and subsequently derive a local dispersion relation and ray-tracing equations, which predict the movement of a wave packet. Their derivations are based on explanations in standard textbooks on wave dynamics (e.g. Lighthill, 1978), and we explain their details in Appendix D. Here we summarise the results. The expression of perturbations of the stream function postulated in Section 2 is here rewritten as $\psi_1 \equiv \mathrm{Re}[M(\phi, \theta, T)\mathrm{e}^{\mathrm{i}\varphi_{\mathrm{L}}(\Phi, \Theta, \tau)}]$, where $M$ is the wave amplitude and $\varphi_{\mathrm{L}}$ is the phase of the wave packet. With

this ansatz, the local wavenumber and the local nondimensional angular frequency are expressed as

$$k(\phi, \theta, T) \equiv \frac{1}{\sin\theta} \frac{\partial \varphi_{\mathrm{L}}}{\partial \Phi}, \qquad l(\phi, \theta, T) \equiv \frac{\partial \varphi_{\mathrm{L}}}{\partial (-\Theta)}, \qquad \lambda(\phi, \theta, T) \equiv -\frac{\partial \varphi_{\mathrm{L}}}{\partial \tau}. \tag{28}$$

Note that $\varphi_{\mathrm{L}}$ depends on the local coordinates $(\Phi, \Theta, \tau)$, while $M$, $k$, $l$ and $\lambda$ depend on the global ones $(\phi, \theta, T)$. The local dispersion relation for our present problem is obtained from the leading order terms in the governing equations (7) in the form

$$\mathcal{D}(\phi, \theta, T, k, l, H) \equiv H^2(k^2 + l^2) + Hk\sin\theta - k^2\mathcal{B}^2\sin^2\theta(k^2 + l^2) = 0, \tag{29}$$

in which $H \equiv |\alpha|^{-1/2}\lambda$ is the scaled nondimensional angular frequency. Replacing $\sin\theta$ and $\mathcal{B}$ in (29) with constants, one would have an equivalent to the nondimensional dispersion relation on a middle latitude $\beta$ plane (Zaqarashvili *et al.*, 2007). Note that we denote $H = \mathcal{H}(\phi, \theta, k, l, T)$ as the solution of (29) for $H$. From (29), the components of the nondimensional local group velocity $\boldsymbol{c}_{\mathrm{g}}$ are given by

$$\frac{c_{\mathrm{g},\phi}}{|\alpha|} \equiv \frac{\partial \mathcal{H}}{\partial k} = -\frac{(\partial \mathcal{D}/\partial k)|_{H=\mathcal{H}}}{(\partial \mathcal{D}/\partial H)|_{H=\mathcal{H}}} = \frac{2k\mathcal{B}^2\sin^2\theta(2k^2 + l^2) - \mathcal{H}(2k\mathcal{H} + \sin\theta)}{2\mathcal{H}(k^2 + l^2) + k\sin\theta}, \tag{30a}$$

$$\frac{c_{\mathrm{g},-\theta}}{|\alpha|} \equiv \frac{\partial \mathcal{H}}{\partial l} = -\frac{(\partial \mathcal{D}/\partial l)|_{H=\mathcal{H}}}{(\partial \mathcal{D}/\partial H)|_{H=\mathcal{H}}} = -\frac{2l(\mathcal{H}^2 - k^2\mathcal{B}^2\sin^2\theta)}{2\mathcal{H}(k^2 + l^2) + k\sin\theta}. \tag{30b}$$

We eventually find the ray-tracing equations

$$\sin\theta \frac{\mathrm{d}_{\mathrm{g}}\phi}{\mathrm{d}T} = \frac{c_{\mathrm{g},\phi}}{|\alpha|}, \qquad \frac{\mathrm{d}_{\mathrm{g}}(-\theta)}{\mathrm{d}T} = \frac{c_{\mathrm{g},-\theta}}{|\alpha|}, \tag{31a}$$

and

$$\frac{\mathrm{d}_{\mathrm{g}}(k\sin\theta)}{\mathrm{d}T} = -\left(\frac{\partial \mathcal{H}}{\partial \phi}\right)_{k,l} = 0, \tag{31b}$$

$$\frac{\mathrm{d}_{\mathrm{g}}l}{\mathrm{d}T} + \frac{c_{\mathrm{g},\phi}}{|\alpha|}k\cot\theta = -\left[\frac{\partial \mathcal{H}}{\partial (-\theta)}\right]_{k,l} = \frac{k^2[\mathrm{d}(\mathcal{B}^2\sin^2\theta)/\mathrm{d}\theta](k^2 + l^2) - \mathcal{H}k\cos\theta}{2\mathcal{H}(k^2 + l^2) + k\sin\theta}, \tag{31c}$$

$$\frac{\mathrm{d}_{\mathrm{g}}H}{\mathrm{d}T} = \left(\frac{\partial \mathcal{H}}{\partial T}\right)_{k,l} = 0, \tag{31d}$$

where the material time derivative moving with the local group velocity is

$$\frac{\mathrm{d}_{\mathrm{g}}}{\mathrm{d}T} \equiv \frac{\partial}{\partial T} + \frac{c_{\mathrm{g},\phi}}{|\alpha|\sin\theta}\frac{\partial}{\partial \phi} + \frac{c_{\mathrm{g},-\theta}}{|\alpha|}\frac{\partial}{\partial (-\theta)} = \frac{\partial}{\partial T} + \frac{\boldsymbol{c}_{\mathrm{g}}}{|\alpha|}\cdot\boldsymbol{\nabla}_{\mathrm{G}}, \tag{31e}$$

with $\boldsymbol{\nabla}_{\mathrm{G}} \equiv (\hat{\boldsymbol{e}}_\phi/\sin\theta)(\partial/\partial\phi) + \hat{\boldsymbol{e}}_{-\theta}[\partial/\partial(-\theta)]$. According to these equations, a wave train migrates with its group velocity depending on its latitudinal position and its dominant local wavenumber, which also varies with the colatitude $\theta$. Furthermore, (31) show that $k\sin\theta$ and $H$ (or $\lambda$) are invariant along a ray trajectory, but $l$ is not.

We conduct the numerical time integration of the ray-tracing equations (31) with (30) for the movement of a wave packet originating at a given initial position $(\theta, \phi)$ with a given initial local wavenumber $(k, l)$ and a local dimensionless angular frequency $\lambda$ determined by the local dispersion relation (29) (e.g. Teruya *et al.*, 2022). In our code, the initial local longitudinal wavenumber $k_{\mathrm{init}}$ is calculated from the relation (29) with the `scipy.optimize.fsolve` function of the SciPy library after one specifies the initial values of $l$, $H$, $\phi$ and $\theta$. The succeeding time integration of (31) is based on an explicit Runge-Kutta method of order 8 (the `DOP853` algorithm in the `scipy.integrate.solve_ivp` function of the SciPy library). This integration is conducted without explicitly using (29) on the way, and the numerical errors in our calculations are monitored by the value of the function $\mathcal{D}$ of (29). Their results are also compared to those of Section 3.1 from the aspect of the evanescent property.

Before demonstrating their trajectories obtained numerically, we examine some properties of the local dispersion relation. In the following preliminary considerations, we assume that the physical variables satisfy the relation $H = \mathcal{H}(\phi, \theta, k, l, T)$ at any time. Figures 14 and 15 show contour plots of the scaled dimensionless
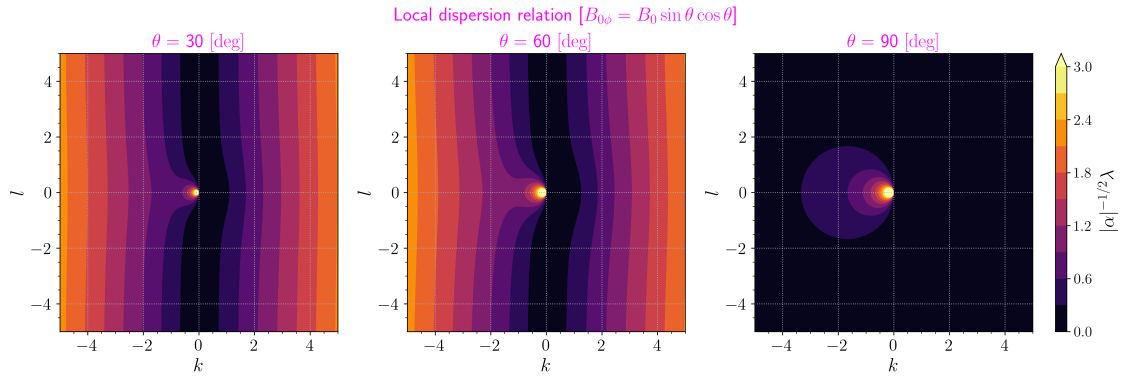
Figure 14: Local dispersion relation given by (32a) when the background field is the simplest equatorially-antisymmetric non-Malkus one ($\mathcal{B} = \cos\theta$). In these panels, the scaled nondimensional angular frequency $H = |\alpha|^{-1/2}\lambda$ is shown as a function of the local wavenumber $(k, l)$ for the colatitudes $\theta = 30°$ (left panel), $60°$ (middle), and $90°$ (right).

angular frequency $H$ as a function of $k$ and $l$ for three different latitudes, when $\mathcal{B} = \cos\theta$ and $\mathcal{B} = 1$, respectively. For ease of understanding Figure 14, we first explain Figure 15, which corresponds to Figure 1 for global modes. These diagrams are calculated from the equation transformed from (29) in the form

$$H = \frac{-k\sin\theta \pm |k|\sin\theta\sqrt{1 + 4\mathcal{B}^2(k^2 + l^2)^2}}{2(k^2 + l^2)} \, . \tag{32a}$$

In Figures 14 and 15, we take the plus of the plus-minus sign so that $H$ should be positive. This means that the sign of $k$ signifies the longitudinal direction of the phase velocity. The nearly vertical contour lines for large absolute values of $l$ in Figure 15 correspond to the relations describing the propagation properties of wave packets that belong to prograde ($H/k > 0$) and retrograde ($H/k < 0$) Alfvén waves. Additionally, it can be concluded that, in Figure 15, the circular contour lines which are tangent to the line $k = 0$ represent the dispersion relation for fast MR waves, and that the slightly curved part of the nearly vertical contour lines near the line $l = 0$ on the half plane $H/k > 0$ explains how slow MR waves propagate. The similarities between Figure 15 and the left and middle panels of Figure 14 suggest that the same is true for the case where $\mathcal{B} = \cos\theta$. However, for $\mathcal{B} = \cos\theta$, no branches of Alfvén and slow MR waves exist at the equator ($\theta = 90°$) as shown in the right panel of Figure 14, since the main field vanishes there. Note that the direction of the gradient $(\partial\mathcal{H}/\partial k, \partial\mathcal{H}/\partial l)$ at a point $(k, l)$ in these plots is identical with that of the group velocity of a wave packet whose dominant local wavenumber is $(k, l)$ at the colatitude $\theta$. For a wave packet belonging to either Alfvén or slow MR waves, the sign of the azimuthal component $c_{\mathrm{g},\phi}$ of its group velocity is the same as that of the azimuthal component $|\alpha|(H/k)$ of its nondimensional local phase velocity, whilst those of the meridional components ($c_{\mathrm{g},-\theta}$ and $|\alpha|(H/l)$) are opposite for the retrograde Alfvén packet.

Figure 14 illustrates the remarkable feature that the north-south component $c_{\mathrm{g},-\theta}$ of the group velocity vanishes at $l = 0$ and $l = \pm\infty$, as can also be seen from (30b). Then, the wave train can be refracted at or absorbed into the latitude, heading only in the $\phi$ direction there (e.g. Acheson, 1972; McKenzie, 1973; Eltayeb, 1977; Eltayeb and Mckenzie, 1977; Grimshaw, 1979). In particular, from (29) the latter situation $l^2 \to \infty$ with a reasonable condition $Hk\sin\theta \neq 0$ leads to the limit $H^2 - k^2\mathcal{B}^2\sin^2\theta \to 0$, which signifies that the latitude is a critical one. It follows that the nearly vertical lines for Alfvén waves in Figure 14 should be linked to the Alfvén continuous modes observed in the results in Section 3. Note that, though the nearly vertical lines in Figure 15 are similar to those in Figure 14, the Malkus field $\mathcal{B} = 1$ does not yield any continuous modes since $H^2 - k^2\mathcal{B}^2\sin^2\theta$ is constant.

The local dispersion relation (29) also allows one to understand the evanescent property of waves from the sign of the squared local meridional wavenumber $l^2$. This value can be calculated from

$$l^2 = -k^2 - \frac{Hk\sin\theta}{H^2 - k^2\mathcal{B}^2\sin^2\theta} \, . \tag{32b}$$

Figure 16 contains contour plots of $l^2$ as a function of $k$ and $H$ for three different latitudes in the case where $\mathcal{B} = \cos\theta$. Waves can propagate only when their wavenumbers fall within the parameter domains where
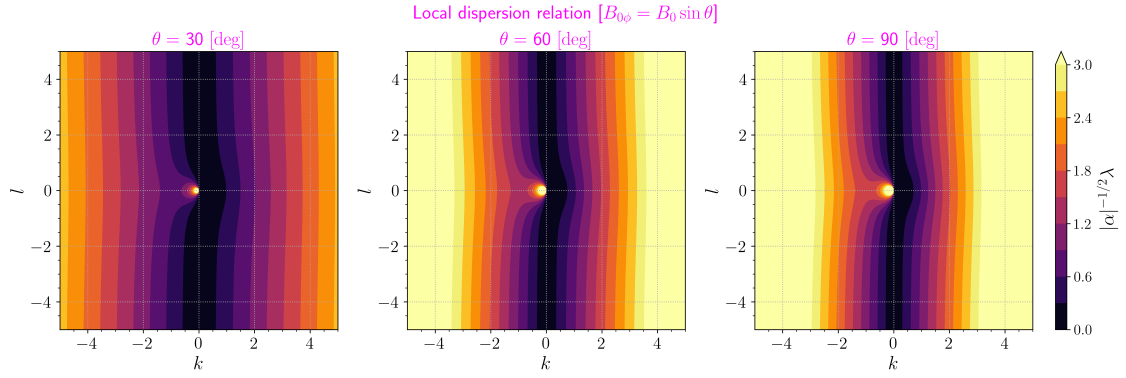
23

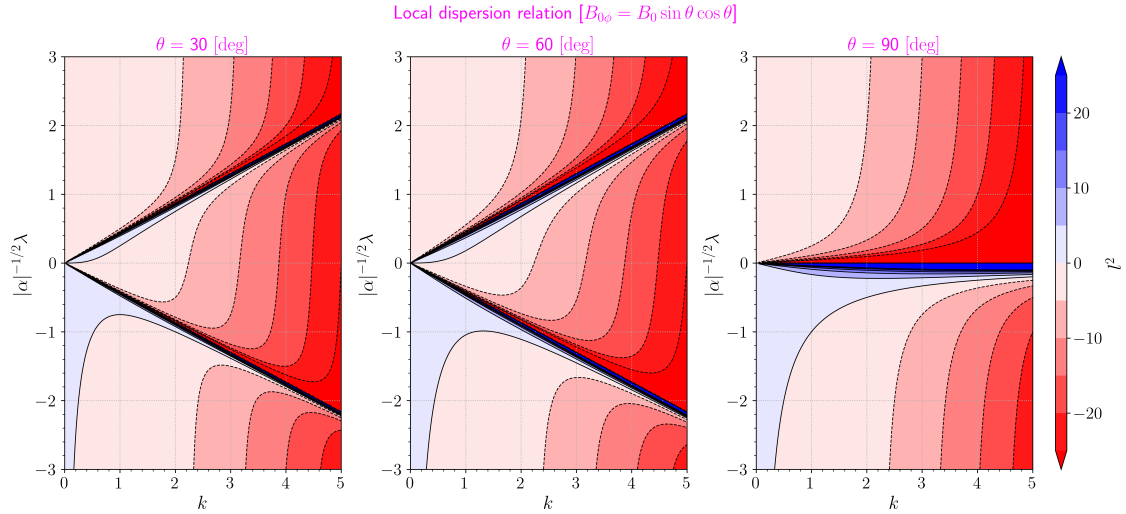Figure 15: Same as Figure 14, but for $\mathcal{B} = 1$.



Figure 16: Local dispersion relation written as (32b) when the simplest equatorially-antisymmetric non-Malkus field $\mathcal{B} = \cos\theta$ is imposed. In these panels, the square $l^2$ of the local meridional wavenumber is displayed as a function of the local longitudinal wavenumber $k$ and the scaled dimensionless angular frequency $H = |\alpha|^{-1/2}\lambda$ for the colatitudes $\theta = 30°$ (left panel), $60°$ (middle), and $90°$ (right).

$^2 > 0$ in these panels, and these regions are classified into three groups. The two thin regions near the lines $H = \pm k|\mathcal{B}|\sin\theta$ in the left and middle panels correspond to the relations for prograde Alfvén and slow MR waves ($H/k > 0$) and retrograde Alfvén waves ($H/k < 0$). Again, as shown in the right panel, no areas for Alfvén and slow MR waves are found at the equator ($\theta = 90°$), since the background field vanishes there. The propagation properties of fast MR waves are represented as the domain near the line $k = 0$ on the half plane $H/k < 0$. Note that again the curved lines $l = 0$ and the lines $H = \pm k|\mathcal{B}|\sin\theta$ show that wave packets can be refracted at or absorbed into the latitude since the latter lines are equivalent to the situation $l^2 \to \infty$.

Figure 16 are also helpful in the short-term prediction of the migration of a wave packet. We will now consider the two cases: (i) when the wave packet heads toward its corresponding critical latitude, and (ii) when the packet proceeds in the direction away from the critical latitude. Since $k\sin\theta$ and $H$ remain constant during the movement of a wave packet, its migration in the north-south direction can be converted into the movement of the point $(k, H)$ in the horizontal direction of the panels in Figure 16 (unless the outlines of their contour plots change significantly depending on the latitude).

1. When a wave train moves equatorward with $H/k$ and $l^2$ positive (then $H/l < 0$ in the north hemisphere from (30b) or Figure 14), $k$ decrease and the point $(k, H)$ approaches the line $H = k|\mathcal{B}|\sin\theta$ from the right on the plots of Figure 16. This means that the train belonging to either prograde Alfvén or slow MR waves approaches its corresponding critical latitude from the polar side and is refracted or absorbed
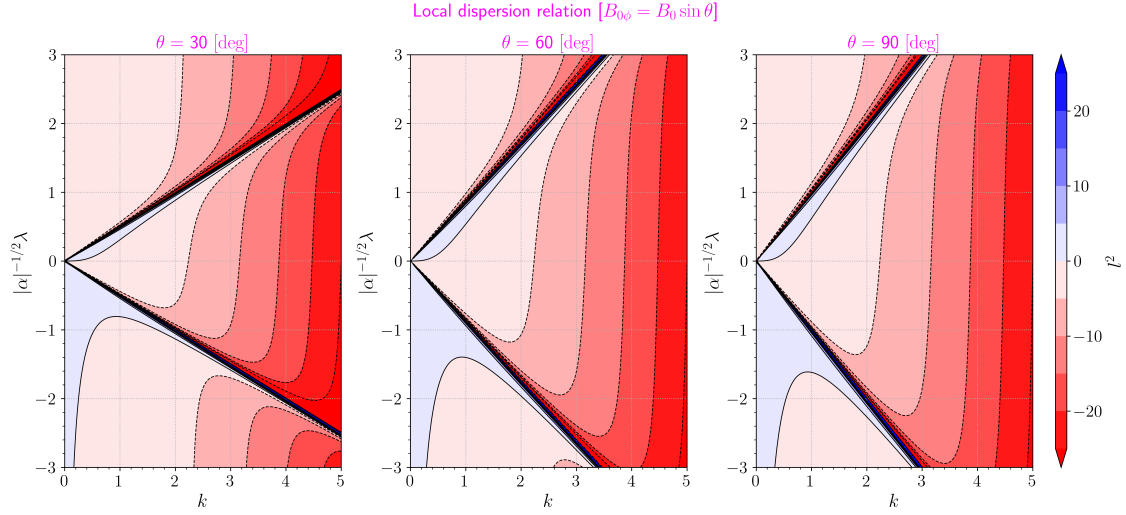
24

Figure 17: Same as Figure 16, but for $\mathcal{B} = 1$.

there. If the train went beyond the latitude, $l^2$ would become negative, hence evanescent waves. Note that, although plots for the Malkus field $\mathcal{B} = 1$, which are illustrated in Figure 17, are similar to Figure 16 except for its right panel ($\theta = 90°$), then the point $(k, H)$ never arrives near the line $H = \pm k|\mathcal{B}| \sin \theta$ due to the constancy of $k \sin \theta$ and $H$ (unless the initial condition has already approximately satisfied this equality). When $H/k$ is negative (under $\mathcal{B} = \cos \theta$), a wave train that travels poleward ($H/l < 0$ in the northern hemisphere) and that does not belong to fast MR waves approaches its corresponding critical latitude, because $k$ increases while it migrates and the point $(k, H)$ approaches the line $H = -k|\mathcal{B}| \sin \theta$ from the left. It follows that the train belonging to retrograde Alfvén waves approaches the critical latitude from the equatorial side.

2. A wave packet moving in the opposite direction from its corresponding critical latitude is realised by a local meridional phase velocity $|\alpha|(H/l)$ which is opposite in sign to the case (i). In other words, we here focus on a packet that travels poleward ($H/l > 0$ in the northern hemisphere) with $H/k$ positive and one that moves equatorward ($H/l > 0$ in the north hemisphere) with $H/k$ negative. Then, the point $(k, H)$ approaches the curved line $l = 0$, resulting in its refraction or absorption. It can be concluded that the packet that belongs to either prograde Alfvén or slow MR waves approaches the latitude where $l = 0$ from the equatorial side and that the packet belonging to retrograde Alfvén waves approaches there from the polar side.

Whether a wave packet is to be refracted at or absorbed into a latitude where $l^2 \to \infty$, or $H^2 = k^2\mathcal{B}^2 \sin^2 \theta$, is considered now. For a general profile of $\mathcal{B}$, near such a colatitude $\theta = \theta_c$, (32b) becomes

$$l^2 \simeq \frac{H/(k \sin \theta)}{(\mathrm{d}\mathcal{B}^2/\mathrm{d}\theta)|_{\theta=\theta_c}(\theta - \theta_c)}, \tag{33}$$

if $(\mathrm{d}\mathcal{B}^2/\mathrm{d}\theta)|_{\theta=\theta_c} \neq 0$. Specifically, when $\mathcal{B} = \cos \theta$, the oscillatory condition $l^2 > 0$ requires that $(\theta - \theta_c) \cos \theta_c$ has the sign opposite to $H/k$; the packet which belongs to either prograde Alfvén or slow MR waves ($H/k > 0$) approaches the critical colatitude $\theta_c$ from the polar side ($(\theta - \theta_c) \cos \theta_c < 0$), while the retrograde Alfvén one ($H/k < 0$) does from the equatorial side ($(\theta - \theta_c) \cos \theta_c > 0$). This is just a mathematical paraphrase of the consideration of the ways that the packets approach the critical latitudes in the previous paragraph. Since the term $Hk \sin \theta$ in (29), which has the same sign as the numerator of (33), represents the planetary $\beta$ effect, the aforementioned distinction between the prograde and retrograde waves is caused by the $\beta$ effect. Additionally,

25

on using (30) and (33), one can obtain an asymptotic expression of the group velocity

$$\frac{c_{g,\phi}}{|\alpha|} \simeq \frac{H}{k} = \mathrm{O}(|\theta - \theta_c|^0),\tag{34a}$$

$$\frac{c_{g,-\theta}}{|\alpha|} \simeq \frac{(\mathrm{d}\mathcal{B}^2/\mathrm{d}\theta)|_{\theta=\theta_c}(k\sin\theta)^2(\theta - \theta_c)}{Hl} = \mathrm{O}(|\theta - \theta_c|^{3/2}).\tag{34b}$$

This expression gives the travel time of the packet from a given latitude $\theta$ in the vicinity of the critical one to the latter in the form

$$\int_\theta^{\theta_c} \frac{|\alpha|}{-c_{g,-\theta}(\theta_*)}\mathrm{d}\theta_* \simeq -\frac{H}{(\mathrm{d}\mathcal{B}^2/\mathrm{d}\theta)|_{\theta=\theta_c}(k\sin\theta)^2}\int_\theta^{\theta_c}\frac{l(\theta_*)}{\theta_* - \theta_c}\mathrm{d}\theta_* = \mathrm{O}(|\theta - \theta_c|^{-1/2}).\tag{35}$$

Any packets therefore never reach their corresponding critical latitudes in a finite time and are absorbed there. In contrast, wave packets are refracted at the latitudes where $l$ vanishes, as will be explained in a similar fashion in Appendix E. The latitudes are often referred to as "turning latitudes."

At last, we shall demonstrate the ray trajectories obtained by the numerical time integration of the ray-tracing equations, though rough ones can be sketched even from the above examination. Figures 18 and 19 show two of the trajectories for wave trains belonging to prograde and retrograde Alfvén waves, respectively. Each of the trains is injected at the black asterisk in each of their upper panels, its position evolving in accordance with (31a). The colours in the trajectories represent their local wavenumbers, or the directions of their local phase velocities, by hue (see their lower left panels for the colour scale). In their lower right panels, the longitudes $\phi$ of their positions at time $T$ are recorded in the same colouring scheme as their upper panels. The numerical errors for the results shown in Figures 18 and 19 are $\mathcal{D} \lesssim 10^{-3}$ throughout their numerical integrations. The trajectories agree with the above predictions in terms of the refraction at turning latitudes, the absorption into the critical ones, and the incident directions to those. From the asymptotic expression (34a) of the group velocity near a critical latitude, one obtains the period for a wave packet to circle along the latitude around a sphere as $\mathrm{sgn}(\Omega_0)T = |2\pi k\sin\theta/H|$, which approximates the periods read from the lower right panels of Figures 18 and 19.

The facts that wave packets can not cross their corresponding critical latitudes and that whether the packets approach there from the polar or equatorial sides depends on the sign of $H/k$ are consistent with the features observed from the numerical results for the continuous modes (Figures 8 and 9) in the eigenvalue problem for global modes when $|\alpha|$ is small. Although the spatial scale of waves focused on in this section is smaller than that of global modes which were thematised in Section 3, this implies that, in the case when $|\alpha| \ll 1$, ray trajectories for Alfvén waves enable one to roughly predict the behaviours of the continuous modes without actually solving the eigenvalue problem. For instance, four of the trajectories for another equatorially-antisymmetric field $\mathcal{B} = \sin\theta\cos\theta$ are displayed in Figures 20 and 21. These figures indicate that, if $\mathcal{B} = \sin\theta\cos\theta$, the prograde continuous modes should be evanescent in the polar and equatorial regions, while the retrograde ones should become evanescent in the mid-latitudes. The value of the function $\mathcal{L}^2$ of (22a) also gives the information about the evanescent property for global modes, as with the sign of $l^2$. This function explicitly includes the effects of the gradient of the background field, parts of which have been indirectly ignored in the derivation of the ray-tracing equations (see Appendix D). However, its approximate formula (24) for a small $|\alpha|$ agrees with (33). Figure 11(b) depicts the values of $\mathcal{L}^2$ when $\mathcal{B} = \mu\sqrt{1-\mu^2}$, and our prediction using the ray theory is consistent with this plot. Based on these facts, we can consider that wave packets belonging to Alfvén waves pertain to the continuous modes in Section 3 as expected.

Moreover, we here learn why discrete branches of slow MR waves disappear under non-Malkus fields, as shown in the dispersion diagrams in Section 3, from the ray-tracing approach. Figure 22 depicts one of the trajectories for a wave packet that (at least initially) belongs to the slow MR wave, because the condition

$$H^2(k^2 + l^2) \ll Hk\sin\theta\tag{36}$$

has been satisfied by its initial condition. This inequality is obtained from the comparison between the first two terms in the local dispersion relation (29) by analogy with slow MR waves in the case of the Malkus field. The illustrated trajectory is similar to those of prograde Alfvén waves (see Figure 18). Since the propagation properties for slow MR waves and those of prograde Alfvén waves are continuous, as seen in Figures 14 and 16, wave packets for slow MR waves transform into prograde Alfvén waves as they migrate in an inhomogeneous

(a) Initial local meridional wavenumber $l_{\text{init}} = 2$.

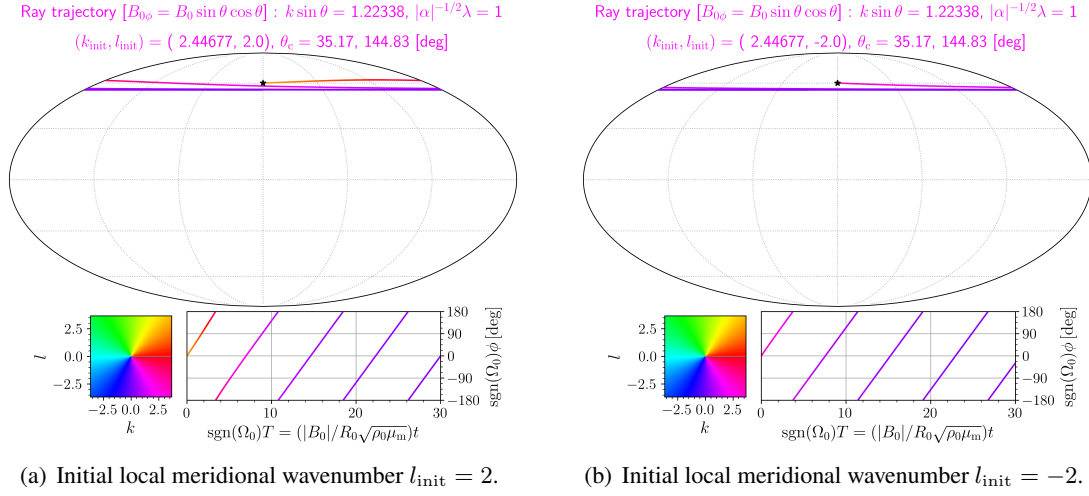(b) Initial local meridional wavenumber $l_{\text{init}} = -2$.

Figure 18: Ray trajectories in the Mollweide projection for wave packets belonging to prograde Alfvén waves (the scaled zonal wavenumber $k \sin \theta \approx 1.22338$, and the critical colatitude $\theta_{\text{c}} \approx 35.17°$ in the north hemisphere) when the simplest equatorially-antisymmetric non-Malkus field $\mathcal{B} = \cos \theta$ pervades the system (upper panels). The scaled dimensionless angular frequency $H = |\alpha|^{-1/2}\lambda = 1$. The black asterisks correspond to their initial position $(\theta_{\text{init}}, \phi_{\text{init}}) = (30°, 0°)$. The directions $(k, l)$ of their local phase velocities are represented by hue, the colour scales of which are the left lower panels. The lower right panels show the longitudes $\phi$ of their positions against the scaled nondimensional time $T = |\alpha|\tau$ with the colour denoting the directions of their local phase velocities. Note that both $\phi$ and $T$ are multiplied by $\text{sgn}(\Omega_0)$ so that the "time" $\text{sgn}(\Omega_0)T$ always become positive even when the rotation rate $\Omega_0$ of the sphere is negative.



(a) Initial local meridional wavenumber $l_{\text{init}} = 2$.

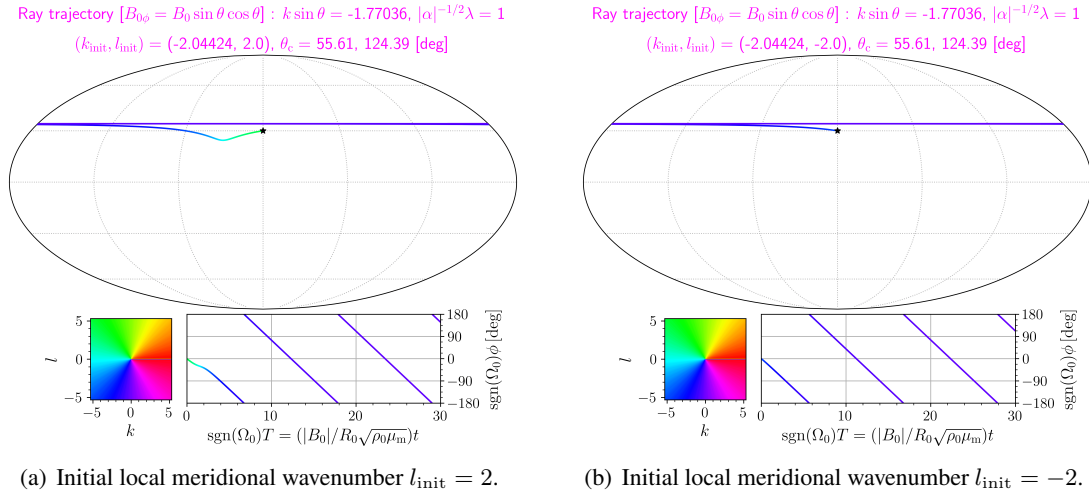(b) Initial local meridional wavenumber $l_{\text{init}} = -2$.

Figure 19: Same as Figure 18, but for retrograde Alfvén waves (the scaled zonal wavenumber $k \sin \theta \approx -1.77036$, and the critical colatitude $\theta_{\text{c}} \approx 55.61°$ in the north hemisphere). The initial colatitude $\theta_{\text{init}} = 60°$.

27

(a) Initial local meridional wavenumber $l_{\mathrm{init}} = 2$.

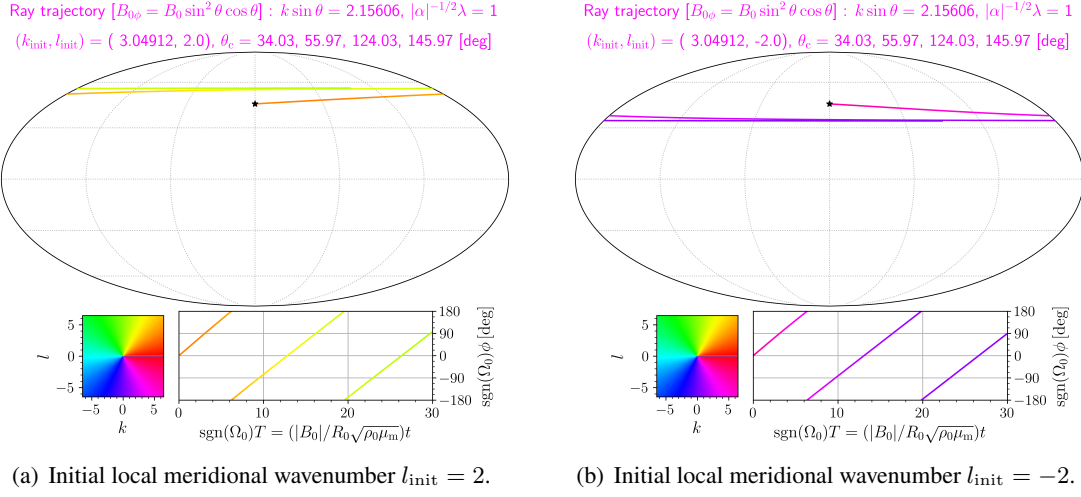(b) Initial local meridional wavenumber $l_{\mathrm{init}} = -2$.

Figure 20: Same as Figure 18, but for $\mathcal{B} = \sin^2\theta\cos\theta$. Ray trajectories for wave packets that belong to prograde Alfvén waves (the scaled zonal wavenumber $k\sin\theta \approx 2.15606$, and the critical colatitudes $\theta_{\mathrm{c}} \approx 34.03°, 55.97°$ in the north hemisphere) are shown. The initial colatitude $\theta_{\mathrm{init}} = 45°$.



(a) Scaled zonal wavenumber $k\sin\theta \approx -2.19789$, and the critical colatitudes $\theta_{\mathrm{c}} \approx 32.75°, 57.25°$ in the north hemisphere. The initial colatitude $\theta_{\mathrm{init}} = 30°$.

(b) Scaled zonal wavenumber $k\sin\theta \approx -2.04809$, and the critical colatitudes $\theta_{\mathrm{c}} \approx 38.78°, 51.22°$ in the north hemisphere. The initial colatitude $\theta_{\mathrm{init}} = 60°$.
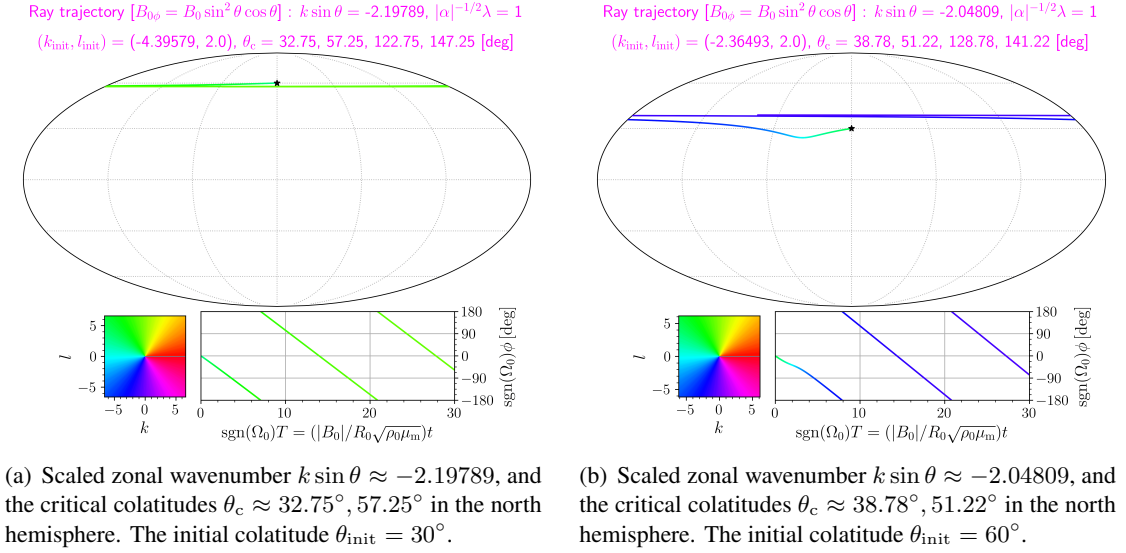
Figure 21: Same as Figure 20, but for retrograde Alfvén waves. The initial local meridional wavenumber $l_{\mathrm{init}} = 2$.
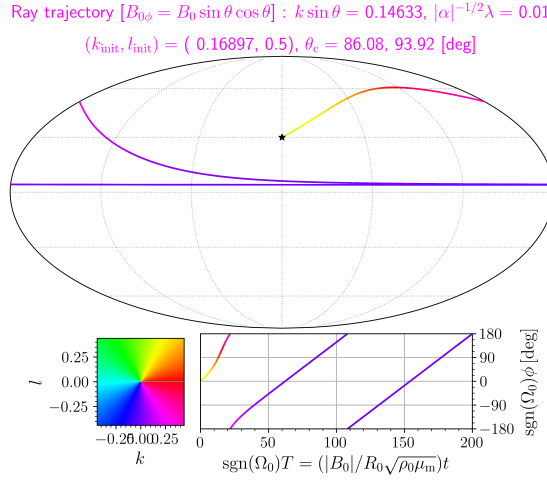
Figure 22: Same as Figure 18, but for slow MR waves (the scaled zonal wavenumber $k \sin \theta \approx 0.14633$, and the critical colatitude $\theta_{\mathrm{c}} \approx 86.08°$ in the north hemisphere). The scaled nondimensional angular frequency $H = |\alpha|^{-1/2}\lambda = 0.01$, the initial local meridional wavenumber $l_{\mathrm{init}} = 0.5$, and the initial colatitude $\theta_{\mathrm{init}} = 60°$.

background field, changing their dominant local meridional wavenumber. The time evolution of $l$ can reverse the inequality sign of the condition (36) as $l^2 \to \infty$, when the Alfvén balance $H^2 \approx k^2\mathcal{B}^2 \sin^2 \theta$ is reached. From (32b), the latitudinal variation of $l^2$ during the migration of a wave packet is written as

$$\left(\frac{\partial l^2}{\partial \theta}\right)_{k \sin \theta, H} = 2k^2 \cot \theta - \frac{Hk^3 \sin^3 \theta}{(H^2 - k^2\mathcal{B}^2 \sin^2 \theta)^2}\frac{\mathrm{d}\mathcal{B}^2}{\mathrm{d}\theta}, \tag{37}$$

and one finds that $(\partial l^2/\partial \theta)_{k \sin \theta, H}$ is always positive (negative) in the northern (southern) hemisphere when $\mathcal{B} = \cos\theta$ and $H/k > 0$. Therefore, mode conversion from slow MR into prograde Alfvén waves should have occurred between the initial colatitude $\theta_{\mathrm{init}}$ and the critical colatitude $\theta_{\mathrm{c}}$ in the example of Figure 22, since $0 \le l^2 \le l^2_{\mathrm{init}}$ within the interval between $\theta_{\mathrm{init}}$ and the turning latitude. Although mode conversions can cause the valve effect (e.g. Acheson, 1972; McKenzie, 1973; Eltayeb, 1977; Grimshaw, 1979), the effect does not occur in our system because there exists only one kind of critical latitudes: the Alfvén resonance $H^2 = k^2\mathcal{B}^2 \sin^2 \theta$. On the other hand, wave trains belonging to fast MR waves, which have discrete branches when $\lambda < -m|\alpha|$ for global modes, move back and forth between two turning latitudes without transforming into Alfvén waves even though its dominant local wavenumber evolves (see Appendix B).

The invariants including the products of perturbations are useful for understanding waves and their associated phenomena. As will be derived in Appendix D, our approximation leads to a conservation law in the form

$$\frac{\partial}{\partial T}\left(\frac{\partial \mathcal{D}}{\partial H}|M|^2\right) + \boldsymbol{\nabla}_{\mathrm{G}} \cdot \left(\frac{\boldsymbol{c}_{\mathrm{g}}}{|\alpha|}\frac{\partial \mathcal{D}}{\partial H}|M|^2\right) = 0. \tag{38}$$

It follows from the constancy of $k \sin \theta$ and $H$ that the equation in which $(\partial \mathcal{D}/\partial H)|M|^2$ is replaced by $(k \sin \theta/H^2)(\partial \mathcal{D}/\partial H)|M|^2$ is also correct. Our subsequent paper will prove that the latter quantity is equivalent to the pseudomomentum density (up to constant factor) for the 2D ideal incompressible MHD system. If weak dissipations are introduced, a packet that is related to the Alfvén continuous modes would attenuate near its corresponding critical latitude, or within its corresponding thin inner boundary layer (see Section 1), due to its long travel time (35). The fact that the packet carries the pseudomomentum in line with (38) implies that the mean flow would be accelerated there because the damping of waves can cause angular momentum exchange between waves and a mean flow in accordance with the wave-mean flow interaction theory (e.g. Bühler, 2009). This possibly may induce nonlinear oscillations such as the quasi-biennial oscillation (QBO) in the Earth's equatorial stratosphere (e.g. Baldwin *et al.*, 2001).

At the end of this section, we shall confirm the validity of the ray theory when $l^2 \to \infty$. The approximation requires that the spatial scales at which the dominant local wavenumber $(k, l)$ and the amplitude $M$ of a wave

29

packet vary are sufficiently larger than its wavelength. This condition can be written as

$$\min \left( \left| \frac{1}{l} \frac{\partial l}{\partial \theta} \right|^{-1}, \left| \frac{1}{M} \frac{\partial M}{\partial \theta} \right|^{-1} \right) \gg \frac{2\pi}{|\alpha|^{-1/2}|l|} \,. \tag{39}$$

To get an asymptotic expression of $|M|$ near its corresponding critical latitude $\theta_c$, we take advantage of the conservation law (38) in the form

$$\iint_{S_g} \left( \frac{\partial \mathcal{D}}{\partial H} |M|^2 \right) \sin \theta \mathrm{d}\theta \mathrm{d}\phi = \mathrm{const.}\,, \tag{40}$$

where $S_g$ is a region moving and deforming with the local group velocity. Let $\theta_1(T)$ and $\theta_2(T)$ be the latitudinal positions, at an arbitrary time $T$, of the rear and front of an isolated wave packet, respectively. Since the local group velocity $c_g$ of the packet depends only on the latitudinal position $\theta$, we have

$$T = \int_{\theta_1(0)}^{\theta_1(T)} \frac{|\alpha|}{-c_{g,-\theta}} \mathrm{d}\theta = \int_{\theta_2(0)}^{\theta_2(T)} \frac{|\alpha|}{-c_{g,-\theta}} \mathrm{d}\theta \,. \tag{41a}$$

Thus, the latitudinal length $|\theta_2 - \theta_1|$ of the packet satisfies

$$\int_{\theta_1(T)}^{\theta_2(T)} \frac{|\alpha|}{-c_{g,-\theta}} \mathrm{d}\theta = \mathrm{const.}\,. \tag{41b}$$

Using these relations, we can estimate that $(\partial \mathcal{D}/\partial H)|M|^2 (\Delta\phi \sin\theta) \propto c_{g,-\theta}^{-1}$ with the longitudinal length $\Delta\phi$ of the packet and achieve $M = \mathrm{O}(|\theta - \theta_c|^{-1/4})$. Note that the same asymptotic expression as this is also obtained from the steady problem in the last two paragraphs of Appendix D. Since $l = \mathrm{O}(|\theta - \theta_c|^{-1/2})$ (from (33)) and $M = \mathrm{O}(|\theta - \theta_c|^{-1/4})$, we can not properly discuss the behaviour of a wave packet if it approaches within the distance $|\theta - \theta_c| = \mathrm{O}(|\alpha|)$ from its corresponding critical latitudes. The case where $l = 0$ is addressed in Appendix E.

## 5 Conclusion

In the present paper, we numerically scrutinised 2D ideal incompressible MHD linear waves within a thin layer on a rotating sphere with latitudinally varying toroidal magnetic fields $B_{0\phi} = B_0 \mathcal{B}(\cos\theta) \sin\theta$. From the eigenvalue problem for the simplest equatorially-antisymmetric non-Malkus field $\mathcal{B} = \cos\theta$, we did not find Alfvén and slow MR discrete branches but a continuous spectrum. In particular, the slow MR waves turn into parts of the Alfvén continuous modes owing to the imposition of the non-Malkus field. The eigenfunctions of the continuous modes and their concomitant critical latitudes were investigated in unprecedented detail and compared with the Frobenius series solutions. The observed difference in the evanescent property between the prograde and retrograde continuous modes results from the planetary $\beta$ effect.

The theory of slowly varying wave packets, or the ray theory, in an inhomogeneous magnetic field for a small absolute value of the Lehnert number $\alpha$ implies that a wave packet that is related to the continuous spectrum moves toward its corresponding critical latitude and is ultimately absorbed there. The fact that whether the packet approaches the latitude from the polar or equatorial sides depends on the sign of the azimuthal component $|\alpha|(H/k)$ of its nondimensional local phase velocity is consistent with the evanescent property of the global modes obtained from the eigenvalue problem, and the planetary $\beta$ effect still causes this distinction of the evanescent property. Additionally, this theory strongly corroborates the idea that slow MR waves transform into Alfvén continuous modes under a non-Malkus field. The novel conservation law (38) derived from this approximation will provide insights into the interaction between waves and the mean flow and magnetic fields, thereby into the weakly nonlinear evolution of the background fields. Accordingly, our results could act as a stepping stone to a deeper understanding of the dynamics of the outermost Earth's core and the solar tachocline.

Other considerations for our problem should be put off until future works. Since slow MR waves occupy an important position as possible causes of geomagnetic fluctuations, it is a pivotal issue whether such waves can remain as discrete modes even under a non-Malkus field by recovering additional effects which we have omitted here or not.

# References

Abramowitz, M. and Stegun, I.A., *Handbook of Mathematical Functions with Formulas, Graphs, and Mathematical Tables*, Vol. 55, 1964 (US Government printing office).

Acheson, D.J., The critical level for hydromagnetic waves in a rotating fluid. *Journal of Fluid Mechanics*, 1972, **53**, 401–415.

Adam, J.A., Critical layer singularities and complex eigenvalues in some differential equations of mathematical physics. *Physics Reports*, 1986, **142**, 263–356.

Arlt, R., Sule, A. and Filter, R., Stability of the solar tachocline with magnetic fields. *Astronomische Nachrichten*, 2007a, **328**, 1142–1145.

Arlt, R., Sule, A. and Rüdiger, G., Stability of toroidal magnetic fields in the solar tachocline. *Astronomy and Astrophysics*, 2007b, **461**, 295–301.

Baldwin, M.P., Gray, L.J., Dunkerton, T.J., Hamilton, K., Haynes, P.H., Randel, W.J., Holton, J.R., Alexander, M.J., Hirota, I., Horinouchi, T., Jones, D.B.A., Kinnersley, J.S., Marquardt, C., Sato, K. and Takahashi, M., The quasi-biennial oscillation. *Reviews of Geophysics*, 2001, **39**, 179–229.

Balmforth, N.J., Llewellyn Smith, S.G. and Young, W.R., Disturbing vortices. *Journal of Fluid Mechanics*, 2001, **426**, 95–133.

Balmforth, N.J. and Morrison, P.J., Normal modes and continuous spectra. *Annals of the New York Academy of Sciences*, 1995a, **773**, 80–94.

Balmforth, N.J. and Morrison, P.J., Singular eigenfunctions for shearing fluids I. 1995b, Technical report, University of Texas at Austin. Institue for Fusion Studies.

Bardsley, O.P. and Davidson, P.A., The dispersion of magnetic-Coriolis waves in planetary cores. *Geophysical Journal International*, 2017, **210**, 18–26.

Barré, J., Olivetti, A. and Yamaguchi, Y.Y., Landau damping and inhomogeneous reference states. *Comptes Rendus Physique*, 2015, **16**, 723–728.

Barston, E.M., Electrostatic oscillations in inhomogeneous cold plasmas. *Annals of Physics*, 1964, **29**, 282–303.

Bouffard, M., Favier, B., Lecoanet, D. and Le Bars, M., Internal gravity waves in a stratified layer atop a convecting liquid core in a non-rotating spherical shell. *Geophysical Journal International*, 2022, **228**, 337–354.

Boyd, J.P., Sturm-Liouville eigenproblems with an interior pole. *Journal of Mathematical Physics*, 1981, **22**, 1575–1590.

Braginsky, S.I., Torsional magnetohydrodynamic vibrations in the Earth's core and variations in day length. *Geomagn. Aeron.*, 1970, **10**, 3–12.

Braginsky, S.I., Short-period geomagnetic secular variation. *Geophysical & Astrophysical Fluid Dynamics*, 1984, **30**, 1–78.

Braginsky, S.I., MAC-oscillations of the hidden ocean of the core. *Journal of geomagnetism and geoelectricity*, 1993, **45**, 1517–1538.

Braginsky, S.I., Magnetic Rossby waves in the stratified ocean of the core, and topographic core-mantle coupling. *Earth, Planets and Space*, 1998, **50**, 641–649.

Braginsky, S.I., Dynamics of the stably stratified ocean at the top of the core. *Physics of the Earth and Planetary Interiors*, 1999, **111**, 21–34.

Braun, M., *Differential Equations and Their Applications*, 1975 (Springer-Verlag, New York).

Bretherton, F.P., The propagation of groups of internal gravity waves in a shear flow. *Quarterly Journal of the Royal Meteorological Society*, 1966, **92**, 466–480.

Briggs, R.J., Daugherty, J.D. and Levy, R.H., Role of Landau damping in crossed-field electron beams and inviscid shear flow. *The Physics of Fluids*, 1970, **13**, 421–432.

Brodholt, J. and Badro, J., Composition of the low seismic velocity E' layer at the top of Earth's core. *Geophysical Research Letters*, 2017, **44**, 8303–8310.

Buffett, B., Geomagnetic fluctuations reveal stable stratification at the top of the Earth's core. *Nature*, 2014, **507**, 484–487.

Buffett, B. and Knezek, N., Stochastic generation of MAC waves and implications for convection in Earth's core. *Geophysical Journal International*, 2018, **212**, 1523–1535.

Buffett, B., Knezek, N. and Holme, R., Evidence for MAC waves at the top of Earth's core and implications for variations in length of day. *Geophysical Journal International*, 2016, **204**, 1789–1800.

Buffett, B. and Matsui, H., Equatorially trapped waves in Earth's core. *Geophysical Journal International*, 2019, **218**, 1210–1225.

Buffett, B.A. and Seagle, C.T., Stratification of the top of the core due to chemical interactions with the mantle. *Journal of Geophysical Research: Solid Earth*, 2010, **115**.

Bühler, O., *Waves and Mean Flows*, Cambridge Monographs on Mechanics 2009 (Cambridge University Press).

Cally, P.S., Nonlinear evolution of 2D tachocline instabilities. *Solar Physics*, 2001, **199**, 231–249.

Cally, P.S., Three-dimensional magneto-shear instabilities in the solar tachocline. *Monthly Notices of the Royal Astronomical Society*, 2003, **339**, 957–972.

Cally, P.S., Dikpati, M. and Gilman, P.A., The solar tachocline: Limiting magneto-tipping instabilities. *Symposium - International Astronomical Union*, 2004, **219**, 541–545.

Cally, P.S., Dikpati, M. and Gilman, P.A., Clamshell and tipping instabilities in a two-dimensional magnetohydrodynamic tachocline. *The Astrophysical Journal*, 2003, **582**, 1190–1205.

Cally, P.S., Dikpati, M. and Gilman, P.A., Three-dimensional magneto-shear instabilities in the solar tachocline - II. Axisymmetric case. *Monthly Notices of the Royal Astronomical Society*, 2008, **391**, 891–900.

Carpenter, J.R. and Guha, A., Instability of a smooth shear layer through wave interactions. *Physics of Fluids*, 2019, **31**, 081701.

Case, K.M., Plasma oscillations. *Annals of Physics*, 1959, **7**, 349–364.

Case, K.M., Stability of inviscid plane Couette flow. *The Physics of Fluids*, 1960, **3**, 143–148.

Chi-Durán, R., Avery, M.S. and Buffett, B.A., Signatures of high-latitude waves in observations of geomagnetic acceleration. *Geophysical Research Letters*, 2021, **48**, e2021GL094692.

Chulliat, A., Alken, P. and Maus, S., Fast equatorial waves propagating at the top of the Earth's core. *Geophysical Research Letters*, 2015, **42**, 3321–3329.

Couston, L.A., Lecoanet, D., Favier, B. and Le Bars, M., Dynamics of mixed convective–stably-stratified fluids. *Physical Review Fluids*, 2017, **2**, 094804.

Crawford, J.D. and Hislop, P.D., Application of the method of spectral deformation to the Vlasov-poisson system. *Annals of Physics*, 1989, **189**, 265–317.

Davies, C.J., Pozzo, M., Gubbins, D. and Alfè, D., Partitioning of oxygen between ferropericlase and Earth's liquid core. *Geophysical Research Letters*, 2018, **45**, 6042–6050.

Dikpati, M., Belucz, B., Gilman, P.A. and McIntosh, S.W., Phase speed of magnetized Rossby waves that cause solar seasons. *The Astrophysical Journal*, 2018a, **862**, 159.

Dikpati, M., Cally, P.S. and Gilman, P.A., Linear analysis and nonlinear evolution of two-dimensional global magnetohydrodynamic instabilities in a diffusive tachocline. *The Astrophysical Journal*, 2004, **610**, 597–615.

Dikpati, M., Cally, P.S., McIntosh, S.W. and Heifetz, E., The origin of the "seasons" in space weather. *Scientific Reports*, 2017, **7**, 14750.

Dikpati, M. and Gilman, P.A., Joint instability of latitudinal differential rotation and concentrated toroidal fields below the solar convection zone. *The Astrophysical Journal*, 1999, **512**, 417–441.

Dikpati, M., Gilman, P.A., Cally, P.S. and Miesch, M.S., Axisymmetric MHD instabilities in solar/stellar tachoclines. *The Astrophysical Journal*, 2009, **692**, 1421–1431.

Dikpati, M., Gilman, P.A., Chatterjee, S., McIntosh, S.W. and Zaqarashvili, T.V., Physics of Magnetohydrodynamic Rossby Waves in the Sun. *The Astrophysical Journal*, 2020, **896**, 141.

Dikpati, M., Gilman, P.A. and Rempel, M., Stability analysis of tachocline latitudinal differential rotation and coexisting toroidal band using a shallow-water model. *The Astrophysical Journal*, 2003, **596**, 680–697.

Dikpati, M., McIntosh, S.W., Bothun, G., Cally, P.S., Ghosh, S.S., Gilman, P.A. and Umurhan, O.M., Role of interaction between magnetic Rossby waves and tachocline differential rotation in producing solar seasons. *The Astrophysical Journal*, 2018b, **853**, 144.

Drazin, P.G. and Reid, W.H., *Hydrodynamic Stability*, Cambridge Mathematical Library 1981 (Cambridge University Press).

Eltayeb, I.A., On linear wave motions in magnetic-velocity shears. *Philosophical Transactions of the Royal Society of London. Series A, Mathematical and Physical Sciences*, 1977, **285**, 607–636.

Eltayeb, I.A. and Mckenzie, J.F., Propagation of hydromagnetic planetary waves on a beta-plane through magnetic and velocity shear. *Journal of Fluid Mechanics*, 1977, **81**, 1–23.

Farrell, B.F., The initial growth of disturbances in a baroclinic flow. *Journal of Atmospheric Sciences*, 1982, **39**, 1663 – 1686.

Finlay, C.C., Course 8 Waves in the presence of magnetic fields, rotation and convection. In *Dynamos*, Les Houches, edited by P. Cardin and L. Cugliandolo, Vol. 88 of *Les Houches*, pp. 403–450, 2008 (Elsevier: Amsterdam).

Gachechiladze, T., Zaqarashvili, T.V., Gurgenashvili, E., Ramishvili, G., Carbonell, M., Oliver, R. and Ballester, J.L., Magneto-Rossby waves in the solar tachocline and the annual variations in solar activity. *The Astrophysical Journal*, 2019, **874**, 162.

Gastine, T., Aubert, J. and Fournier, A., Dynamo-based limit to the extent of a stable layer atop Earth's core. *Geophysical Journal International*, 2020, **222**, 1433–1448.

Gillet, N., Gerick, F., Angappan, R. and Jault, D., A dynamical prospective on interannual geomagnetic field changes. *Surveys in Geophysics*, 2021.

Gillet, N., Jault, D., Canet, E. and Fournier, A., Fast torsional waves and strong magnetic field within the Earth's core. *Nature*, 2010, **465**, 74–77.

Gilman, P.A., Magnetohydrodynamic "shallow water" equations for the solar tachocline. *The Astrophysical Journal*, 2000, **544**, L79–L82.

Gilman, P.A. and Dikpati, M., Joint instability of latitudinal differential rotation and concentrated toroidal fields below the solar convection zone. II. Instability of narrow bands at all latitudes. *The Astrophysical Journal*, 2000, **528**, 552–572.

Gilman, P.A. and Dikpati, M., Analysis of instability of latitudinal differential rotation and toroidal field in the solar tachocline using a magnetohydrodynamic shallow-water model. I. Instability for broad toroidal field profile. *The Astrophysical Journal*, 2002, **576**, 1031–1047.

Gilman, P.A., Dikpati, M. and Miesch, M.S., Global MHD instabilities in a three-dimensional thin-shell model of solar tachocline. *The Astrophysical Journal Supplement Series*, 2007, **170**, 203–227.

Gilman, P.A. and Fox, P.A., Joint instability of latitudinal differential rotation and toroidal magnetic fields below the solar convection zone. *The Astrophysical Journal*, 1997, **484**, 439–454.

Gilman, P.A. and Fox, P.A., Joint instability of latitudinal differential rotation and toroidal magnetic fields below the solar convection zone. II. Instability for toroidal fields that have a node between the equator and pole. *The Astrophysical Journal*, 1999a, **510**, 1018–1044.

Gilman, P.A. and Fox, P.A., Joint instability of latitudinal differential rotation and toroidal magnetic fields below the solar convection zone. III. Unstable disturbance phenomenology and the solar cycle. *The Astrophysical Journal*, 1999b, **522**, 1167–1189.

Gizon, L., Fournier, D. and Albekioni, M., Effect of latitudinal differential rotation on solar Rossby waves: Critical layers, eigenfunctions, and momentum fluxes in the equatorial $\beta$ plane. *Astronomy and Astrophysics*, 2020, **642**, A178.

Goedbloed, J.P.H. and Poedts, S., *Principles of Magnetohydrodynamics: With Applications to Laboratory and Astrophysical Plasmas*, 2004 (Cambridge University Press).

Grimshaw, R., A general theory of critical level absorption and valve effects for linear wave propagation. *Geophysical and Astrophysical Fluid Dynamics*, 1979, **14**, 303–326.

Gubbins, D. and Davies, C.J., The stratified layer at the core-mantle boundary caused by barodiffusion of oxygen, sulphur and silicon. *Physics of the Earth and Planetary Interiors*, 2013, **215**, 21–28.

Gubbins, D., Thomson, C.J. and Whaler, K.A., Stable regions in the Earth's liquid core. *Geophysical Journal International*, 1982, **68**, 241–251.

Hardy, C.M., Livermore, P.W. and Niesen, J., Enhanced magnetic fields within a stratified layer. *Geophysical Journal International*, 2020, **222**, 1686–1703.

Heifetz, E., Guha, A. and Carpenter, J.R., Wave interactions in neutrally stable shear layers: Regular and singular modes, and non-modal growth. *Physics of Fluids*, 2020, **32**, 074106.

Helffrich, G. and Kaneshima, S., Outer-core compositional stratification from observed core wave speed profiles. *Nature*, 2010, **468**, 807–810.

Heng, K. and Spitkovsky, A., Magnetohydrodynamic shallow water waves: Linear analysis. *The Astrophysical Journal*, 2009, **703**, 1819–1831.

Hide, R., Free hydromagnetic oscillations of the Earth's core and the theory of the geomagnetic secular variation. *Philosophical Transactions of the Royal Society of London. Series A, Mathematical and Physical Sciences*, 1966, **259**, 615–647.

Hollerbach, R. and Cally, P.S., Nonlinear evolution of axisymmetric twisted flux tubes in the solar tachocline. *Solar Physics*, 2009, **260**, 251–260.

Hori, K., Nilsson, A. and Tobias, S.M., Waves in planetary dynamos. *Reviews of Modern Plasma Physics*, 2023, **7**, 5.

Hughes, D.W. and Tobias, S.M., On the instability of magnetohydrodynamic shear flows. *Proceedings of the Royal Society of London. Series A: Mathematical, Physical and Engineering Sciences*, 2001, **457**, 1365–1384.

Iga, K., Critical layer instability as a resonance between a non-singular mode and continuous modes. *Fluid Dynamics Research*, 1999, **25**, 63–86.

Iga, K., Shear instability as a resonance between neutral waves hidden in a shear flow. *Journal of Fluid Mechanics*, 2013, **715**, 452–476.

Irving, J.C.E., Cottaar, S. and Lekić, V., Seismically determined elastic parameters for Earth's outer core. *Science Advances*, 2018, **4**, eaar2538.

Jaupart, E. and Buffett, B., Generation of MAC waves by convection in Earth's core. *Geophysical Journal International*, 2017, **209**, 1326–1336.

Kaneshima, S., Array analyses of SmKS waves and the stratification of Earth's outermost core. *Physics of the Earth and Planetary Interiors*, 2018, **276**, 234–246.

Kitchatinov, L.L. and Rüdiger, G., Stability of toroidal magnetic fields in rotating stellar radiation zones. *Astronomy and Astrophysics*, 2008, **478**, 1–8.

Knezek, N. and Buffett, B., Influence of magnetic field configuration on magnetohydrodynamic waves in Earth's core. *Physics of the Earth and Planetary Interiors*, 2018, **277**, 1–9.

Landau, L., On the vibration of the electronic plasma. *Journal of Physics U.S.S.R.*, 1946, **10**, 25.

Landeau, M., Olson, P., Deguen, R. and Hirsh, B.H., Core merging and stratification following giant impact. *Nature Geoscience*, 2016, **9**, 786–789.

Lighthill, J., *Waves in Fluids*, 1978 (Cambridge University Press).

Longuet-Higgins, M.S., The eigenfunctions of Laplace's tidal equation over a sphere. *Philosophical Transactions of the Royal Society of London. Series A, Mathematical and Physical Sciences*, 1968, **262**, 511–607.

Mak, J., Griffiths, S.D. and Hughes, D.W., Shear flow instabilities in shallow-water magnetohydrodynamics. *Journal of Fluid Mechanics*, 2016, **788**, 767–796.

Malkus, W.V.R., Hydromagnetic planetary waves. *Journal of Fluid Mechanics*, 1967, **28**, 793–802.

Márquez-Artavia, X., Jones, C.A. and Tobias, S.M., Rotating magnetic shallow water waves and instabilities in a sphere. *Geophysical and Astrophysical Fluid Dynamics*, 2017, **111**, 282–322.

Maslowe, S.A., Critical layers in shear flows. *Annual Review of Fluid Mechanics*, 1986, **18**, 405–432.

McKenzie, J.F., On the existence of critical levels, with applications to hydromagnetic waves. *Journal of Fluid Mechanics*, 1973, **58**, 709–726.

Miesch, M.S. and Gilman, P.A., Thin-shell magnetohydrodynamic equations for the solar tachocline. *Solar Physics*, 2004, **220**, 287–305.

Miesch, M.S., Gilman, P.A. and Dikpati, M., Nonlinear evolution of global magnetoshear instabilities in a three-dimensional thin-shell model of the solar tachocline. *The Astrophysical Journal Supplement Series*, 2007, **168**, 337–361.

Moffatt, H.K., Magnetic field generation in electrically conducting fluids. *Cambridge Monographs on Mechanics and Applied Mathematics*, 1978.

Mound, J., Davies, C., Rost, S. and Aurnou, J., Regional stratification at the top of Earth's core due to core–mantle boundary heat flux variations. *Nature Geoscience*, 2019, **12**, 575–580.

Pozzo, M., Davies, C., Gubbins, D. and Alfè, D., Thermal and electrical conductivity of iron at Earth's core conditions. *Nature*, 2012, **485**, 355–358.

Raphaldini, B. and Raupp, C.F.M., Nonlinear MHD Rossby wave interactions and persistent geomagnetic field structures. *Proceedings of the Royal Society A: Mathematical, Physical and Engineering Sciences*, 2020, **476**, 20200174.

Schecter, D.A., Dubin, D.H.E., Cass, A.C., Driscoll, C.F., Lansky, I.M. and O'Neil, T.M., Inviscid damping of asymmetries on a two-dimensional vortex. *Physics of Fluids*, 2000, **12**, 2397–2412.

Sedláček, Z., Electrostatic oscillations in cold inhomogeneous plasma I. Differential equation approach. *Journal of Plasma Physics*, 1971, **5**, 239–263.

Sharif, B.W. and Jones, C.A., Rotational and magnetic instability in the diffusive tachocline. *Geophysical and Astrophysical Fluid Dynamics*, 2005, **99**, 493–511.

Shivamoggi, B.K., Ideal and resistive magnetohydrodynamic modes. *International Journal of Theoretical Physics*, 1992, **31**, 2121–2141.

Spencer, R.L. and Rasband, S.N., Damped diocotron quasi-modes of non-neutral plasmas and inviscid fluids. *Physics of Plasmas*, 1997, **4**, 53–60.

Spiegel, E.A. and Zahn, J.P., The solar tachocline. *Astronomy and Astrophysics*, 1992, **265**, 106–114.

Steinolfson, R.S., Resistive wave dissipation on magnetic inhomogeneities Normal modes and phase mixing. *The Astrophysical Journal*, 1985, **295**, 213–219.

Stewartson, K., Slow oscillations of fluid in a rotating cavity in the presence of a toroidal magnetic field. *Proceedings of the Royal Society of London. Series A. Mathematical and Physical Sciences*, 1967, **299**, 173–187.

Strogatz, S.H., From Kuramoto to Crawford: exploring the onset of synchronization in populations of coupled oscillators. *Physica D: Nonlinear Phenomena*, 2000, **143**, 1–20.

Takehiro, S. and Lister, J.R., Penetration of columnar convection into an outer stably stratified layer in rapidly rotating spherical fluid shells. *Earth and Planetary Science Letters*, 2001, **187**, 357–366.

Taniguchi, H. and Ishiwatari, M., Physical interpretation of unstable modes of a linear shear flow in shallow water on an equatorial beta-plane. *Journal of Fluid Mechanics*, 2006, **567**, 1–26.

Tataronis, J. and Grossmann, W., Decay of MHD waves by phase mixing. *Zeitschrift für Physik A Hadrons and nuclei*, 1973, **261**, 203–216.

Teruya, A.S.W., Raphaldini, B. and Raupp, C.F.M., Ray tracing of MHD Rossby waves in the solar tachocline: Meridional propagation and implications for the solar magnetic activity. *Frontiers in Astronomy and Space Sciences*, 2022, **9**.

Triana, S.A., Dumberry, M., Cébron, D., Vidal, J., Trinh, A., Gerick, F. and Rekier, J., Core eigenmodes and their impact on the Earth's rotation. *Surveys in Geophysics*, 2021.

Tung, K.K., A theory of stationary long waves. Part III: Quasi-normal modes in a singular waveguide. *Monthly Weather Review*, 1979, **107**, 751–774.

Turner, M.R. and Gilbert, A.D., Linear and nonlinear decay of cat's eyes in two-dimensional vortices, and the link to Landau poles. *Journal of Fluid Mechanics*, 2007, **593**, 255–279.

Uberoi, C., Alfvén waves in inhomogeneous magnetic fields. *The Physics of Fluids*, 1972, **15**, 1673–1675.

Van Kampen, N.G., On the theory of stationary waves in plasmas. *Physica*, 1955, **21**, 949–963.

van Tent, R., Deuss, A., Kaneshima, S. and Thomas, C., The signal of outermost-core stratification in body-wave and normal-mode data. *Geophysical Journal International*, 2020, **223**, 1338–1354.

Wang, C., Gilbert, A. and Mason, J., Critical-layer instability of shallow-water magnetohydrodynamic shear flows. *Journal of Fluid Mechanics*, 2022a, **943**, A24.

Wang, C., Gilbert, A.D. and Mason, J., An analytical study of the MHD clamshell instability on a sphere. *Journal of Fluid Mechanics*, 2022b, **953**, A38.

Zaqarashvili, T.V., Albekioni, M., Ballester, J.L., Bekki, Y., Biancofiore, L., Birch, A.C., Dikpati, M., Gizon, L., Gurgenashvili, E., Heifetz, E., Lanza, A.F., McIntosh, S.W., Ofman, L., Oliver, R., Proxauf, B., Umurhan, O.M. and Yellin-Bergovoy, R., Rossby waves in astrophysics. *Space Science Reviews*, 2021, **217**, 15.

Zaqarashvili, T.V., Oliver, R. and Ballester, J.L., Global shallow water magnetohydrodynamic waves in the solar tachocline. *The Astrophysical Journal*, 2009, **691**, L41–L44.

Zaqarashvili, T.V., Oliver, R., Ballester, J.L., Carbonell, M., Khodachenko, M.L., Lammer, H., Leitzinger, M. and Odert, P., Rossby waves and polar spots in rapidly rotating stars: Implications for stellar wind evolution. *Astronomy and Astrophysics*, 2011, **532**, A139.

Zaqarashvili, T.V., Oliver, R., Ballester, J.L. and Shergelashvili, B.M., Rossby waves in "shallow water" magnetohydrodynamics. *Astronomy and Astrophysics*, 2007, **470**, 815–820.

Zaqarashvili, T., Equatorial magnetohydrodynamic shallow water waves in the solar tachocline. *The Astrophysical Journal*, 2018, **856**, 32.

Zaqarashvili, T.V., Carbonell, M., Oliver, R. and Ballester, J.L., Magnetic Rossby waves in the solar tachocline and Rieger-type periodicities. *The Astrophysical Journal*, 2010a, **709**, 749–758.

Zaqarashvili, T.V., Carbonell, M., Oliver, R. and Ballester, J.L., Quasi-biennial oscillations in the solar tachocline caused by magnetic Rossby wave instabilities. *The Astrophysical Journal*, 2010b, **724**, L95–L98.

Zaqarashvili, T.V., Oliver, R., Hanslmeier, A., Carbonell, M., Ballester, J.L., Gachechiladze, T. and Usoskin, I.G., Long-term variation in the Sun's activity caused by magnetic Rossby waves in the tachocline. *The Astrophysical Journal*, 2015, **805**, L14.

Zatman, S. and Bloxham, J., Torsional oscillations and the magnetic field within the Earth's core. *Nature*, 1997, **388**, 760–763.

Zhang, Y., Luo, K., Hou, M., Driscoll, P., Salke, N.P., Minár, J., Prakapenka, V.B., Greenberg, E., Hemley, R.J., Cohen, R.E. and Lin, J.F., Thermal conductivity of Fe-Si alloys and thermal stratification in Earth's core. *Proceedings of the National Academy of Sciences*, 2022, **119**.

# A  Proofs of (16a) and (16b)

In this first appendix, we prove two theorems (16a) and (16b) giving eigenvalue bounds. Integrating (9) with respect to $\mu$ from $-1$ to $1$ after it is multiplied by the complex conjugate of $\tilde{\psi}$, we find

$$\int_{-1}^{1} \Lambda |\tilde{Q}|^2 \mathrm{d}\mu + m \int_{-1}^{1} \left[ \lambda + 2m\alpha^2 \mathcal{B} \frac{\mathrm{d}(\mathcal{B}\mu)}{\mathrm{d}\mu} \right] |\tilde{\psi}|^2 \mathrm{d}\mu = 0 \,, \tag{42}$$

where $|\tilde{Q}|^2 \equiv (1 - \mu^2)|\mathrm{d}\tilde{\psi}/\mathrm{d}\mu|^2 + [m^2/(1 - \mu^2)]|\tilde{\psi}|^2$. The real part of (42) is given by

$$\begin{aligned}
\left\{ [\mathrm{Re}(\lambda)]^2 - [\mathrm{Im}(\lambda)]^2 \right\} \int_{-1}^{1} |\tilde{Q}|^2 \mathrm{d}\mu &- m^2\alpha^2 \int_{-1}^{1} \mathcal{B}^2 |\tilde{Q}|^2 \mathrm{d}\mu \\
&+ m\mathrm{Re}(\lambda) \int_{-1}^{1} |\tilde{\psi}|^2 \mathrm{d}\mu + 2m^2\alpha^2 \int_{-1}^{1} \mathcal{B} \frac{\mathrm{d}(\mathcal{B}\mu)}{\mathrm{d}\mu} |\tilde{\psi}|^2 \mathrm{d}\mu = 0 \,.
\end{aligned} \tag{43a}$$

On the other hand, the imaginary part is

$$\mathrm{Im}(\lambda) \left( 2\mathrm{Re}(\lambda) \int_{-1}^{1} |\tilde{Q}|^2 \mathrm{d}\mu + m \int_{-1}^{1} |\tilde{\psi}|^2 \mathrm{d}\mu \right) = 0 \,. \tag{43b}$$

Note that $\text{Re}(\lambda) \leq 0$ when $\text{Im}(\lambda) \neq 0$, as can be seen from (43b). The combination of the expressions (43a) and (43b) with $\text{Im}(\lambda) \neq 0$ yields

$$\left[\frac{\text{Re}(\lambda)}{m}\right]^2 + \left[\frac{\text{Im}(\lambda)}{m}\right]^2 = -\alpha^2 \frac{\int_{-1}^{1} \mathcal{B}^2 |\tilde{Q}|^2 \mathrm{d}\mu}{\int_{-1}^{1} |\tilde{Q}|^2 \mathrm{d}\mu} + 4 \frac{-\text{Re}(\lambda)}{m} \alpha^2 \frac{\int_{-1}^{1} \mathcal{B}[\mathrm{d}(\mathcal{B}\mu)/\mathrm{d}\mu]|\tilde{\psi}|^2 \mathrm{d}\mu}{\int_{-1}^{1} |\tilde{\psi}|^2 \mathrm{d}\mu}$$

$$\leq -\alpha^2 \min(\mathcal{B}^2) + 2 \frac{-\text{Re}(\lambda)}{m} \alpha^2 \max\left[2\mathcal{B}\frac{\mathrm{d}(\mathcal{B}\mu)}{\mathrm{d}\mu}\right]. \tag{44}$$

This inequality gives (16a).

We can derive another bound (16b) by using (43b) when $\text{Im}(\lambda) \neq 0$. The property of the Rayleigh quotient of the associated Legendre operator in the form

$$m(m+1) = \min_{\tilde{\psi}(\mu)} \frac{\int_{-1}^{1} |\tilde{Q}|^2 \mathrm{d}\mu}{\int_{-1}^{1} |\tilde{\psi}|^2 \mathrm{d}\mu} \tag{45}$$

then becomes

$$-\frac{m}{2\text{Re}(\lambda)} \geq m(m+1), \tag{46}$$

unless $\text{Im}(\lambda) = 0$. This inequality is equal to (16b) since $\text{Re}(\lambda) \leq 0$.

## B    Fast MR waves when $\mathcal{B} = \mu$

This appendix and Appendix C cover the fast MR waves when the simplest equatorially-antisymmetric non-Malkus field $\mathcal{B} = \mu$ is imposed. In particular, we now narrow our interests down to discrete branches $\lambda < -m|\alpha|$ outside the continuous spectrum. If one focuses on waves with frequencies $|\lambda| \gg m|\alpha|$, sufficiently higher than the continuous modes, (22a) is reduced to

$$\mathcal{L}^2 = -m^2 + (1-\mu^2)\left[\left(-\frac{m}{\lambda} + \frac{m^2\alpha^2}{\lambda^2}\right) - c^2\mu^2 + \text{O}\left(\frac{\alpha^4}{\lambda^4}\right)\right], \tag{47}$$

where $c^2 \equiv (m^2\alpha^2/\lambda^2)(7 + m/\lambda)$, and then (22b) approximately becomes the same form as the differential equation for the angular prolate spheroidal wave function $\text{S}_{mn}(c, \mu)$ (e.g. Abramowitz and Stegun 1964; see also Zaqarashvili *et al.* 2009). The power series expansion for the eigenvalues $\lambda_{mn} \equiv -m/\lambda + m^2\alpha^2/\lambda^2$ of this differential equation yields the approximate dispersion relation for the fast MR waves outside the continuous spectrum in the form

$$\lambda_{mn} = n(n+1) + \frac{1}{2}\left[1 - \frac{(2m-1)(2m+1)}{(2n-1)(2n+3)}\right]c^2 + \text{O}\left(\frac{\alpha^4}{\lambda^4}\right). \tag{48}$$

Their approximate angular frequencies $\lambda_{\text{approx}}$ were calculated from the above relation with the `scipy.optimize.fsolve` function of the SciPy library. Their results for $m = 1$ are shown in Figure 23, overlaid on the same graphs as the left panels of Figure 3. When $|\lambda| \gg m|\alpha|$, their values surely approximate the angular frequencies obtained numerically from the full eigenvalue problem. Figure 24 displays two of their approximate eigenfunctions $\text{S}_{mn}/\sqrt{\lambda_{\text{approx}}^2 - m^2\alpha^2\mu^2} (\simeq \tilde{\psi})$, in which $\text{S}_{mn}$ were given by the `scipy.special.pro_ang1` function of the SciPy library, with their corresponding eigenfunctions calculated from the full problem. Note that, if $c^2 = (m^2\alpha^2/\lambda_{\text{approx}}^2)(7 + m/\lambda_{\text{approx}}) < 0$, the parameter $c$ in $\text{S}_{mn}(c, \mu)$ is replaced by $-ic$, and then $\text{S}_{mn}(-ic, \mu)$ is regarded as the angular oblate spheroidal wave function. In this case, we used the `scipy.special.obl_ang1` function of the SciPy library.

We also integrated the ray-tracing equations (see Section 4) numerically for wave packets that belong to fast MR waves. Figure 25 shows three of their trajectories when $\mathcal{B} = \cos\theta$. They move back and forth between two turning latitudes, at which $l = 0$, in the latitudinal direction, while their manners of migration in the longitudinal direction are complicated by the fact that the radii of the circular contour lines which represent the propagation properties of the packets belonging to the fast modes depend on the latitude (see Figure 14); when the point $(k, l)$ corresponding to the dominant local wavenumber of a wave packet is located on the left half of one of the
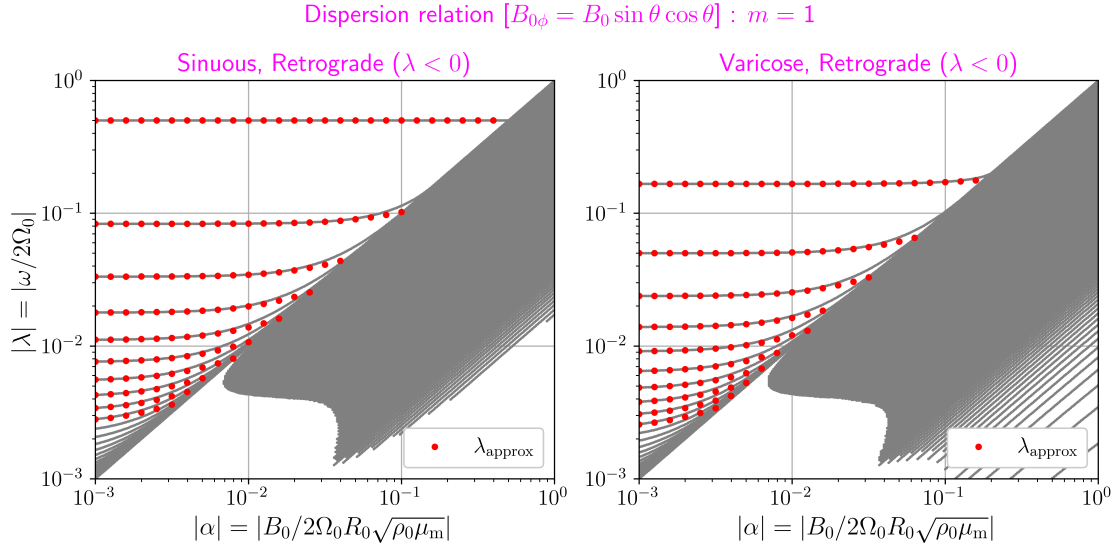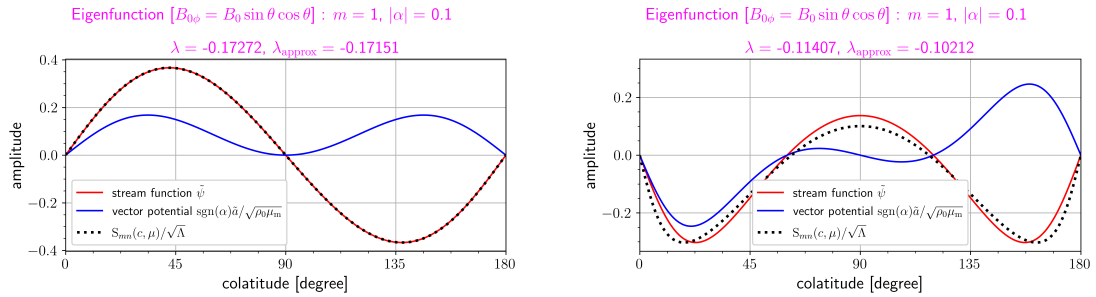
Figure 23: Same as the left panels of Figure 3, but for a different plotting range (grey markers). The red circles represent the approximate dimensionless angular frequencies $\lambda_{\text{approx}}$ calculated by the approximate dispersion relation (48).



(a) Varicose mode with $\lambda \approx -0.17272$ and the approximate eigenmode with $\lambda_{\text{approx}} \approx -0.17151$ ($n = 2$, $c^2 \approx 0.39756$).

(b) Sinuous mode with $\lambda \approx -0.11407$ and the approximate eigenmode with $\lambda_{\text{approx}} \approx -0.10212$ ($n = 3$, $c^2 \approx -2.6777$).

Figure 24: Same as Figure 6(a), but for fast MR waves outside the continuous spectrum. The black dashed curves illustrate their approximate eigenfunctions $S_{mn}/\sqrt{\Lambda}$. The eigenfunctions have been scaled so that their amplitudes become comparable to those of their corresponding eigenfunctions which are obtained numerically from the full eigenvalue problem.
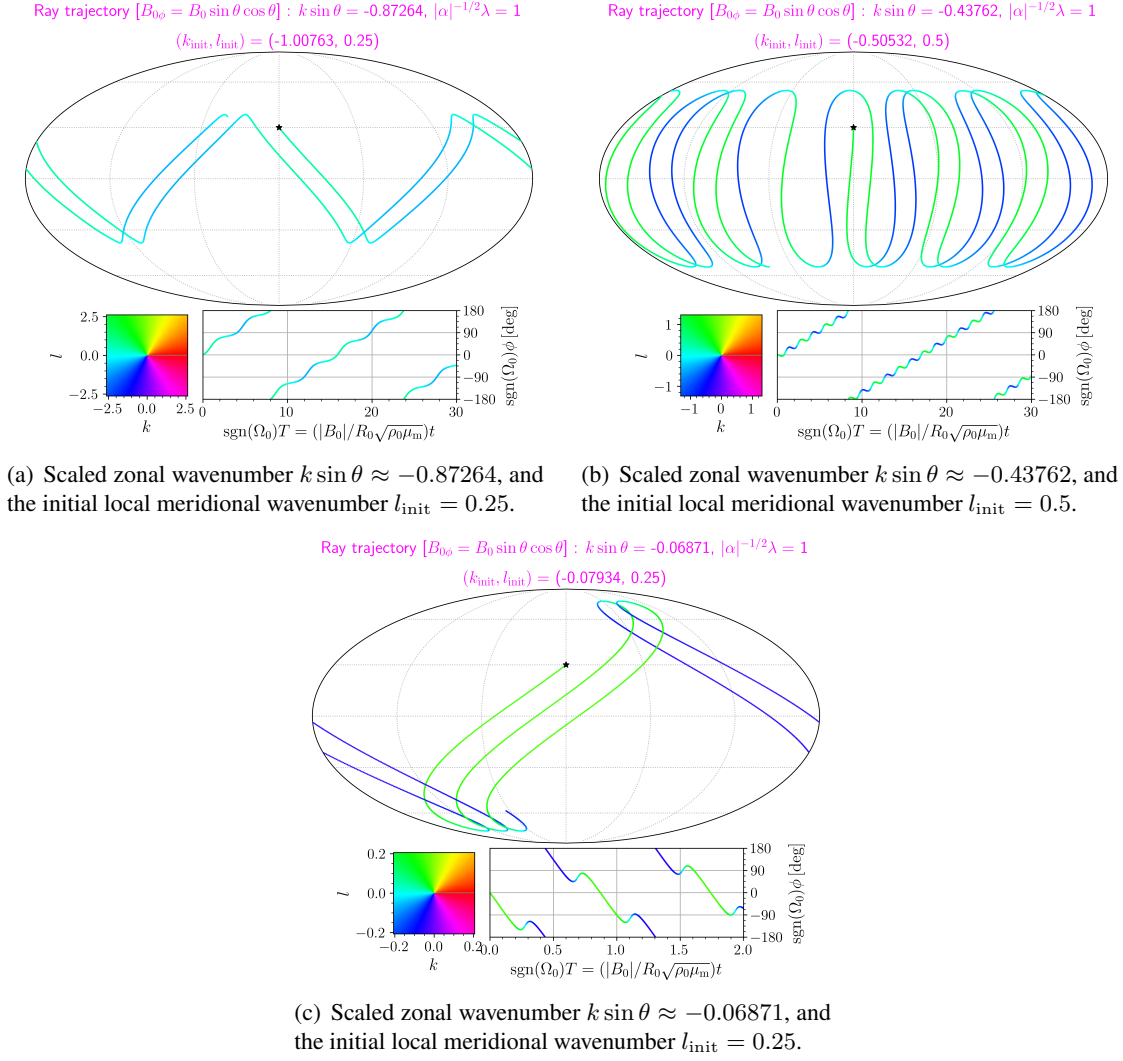
(a) Scaled zonal wavenumber $k \sin \theta \approx -0.87264$, and the initial local meridional wavenumber $l_{\text{init}} = 0.25$.

(b) Scaled zonal wavenumber $k \sin \theta \approx -0.43762$, and the initial local meridional wavenumber $l_{\text{init}} = 0.5$.

(c) Scaled zonal wavenumber $k \sin \theta \approx -0.06871$, and the initial local meridional wavenumber $l_{\text{init}} = 0.25$.

Figure 25: Same as Figure 18, but for fast MR waves. The initial colatitude $\theta_{\text{init}} = 60°$.

contour lines, the azimuthal component $c_{\text{g},\phi}$ of its group velocity is positive (see the cyanish markers in Figures 25(a), (b) and (c)), and conversely $c_{\text{g},\phi} < 0$ for the points on the right half (see the green and blue markers in Figures 25(b) and (c)). Since no critical latitudes exist, their behaviours are decidedly different from those of Alfvén (see Figures 18 and 19) and slow MR waves (see Figure 22).

## C  Discrete eigenvalue buried in the continuous spectrum

We here explain, for the simplest equatorially-antisymmetric non-Malkus background field $\mathcal{B} = \mu$, why the lowest mode of the $m = 1$ sinuous modes of the fast MR wave has no critical latitudes (see the upper panels of Figure 10), and why its branch can penetrate the Alfvén continuous spectrum while being discrete (see the upper left panel of Figure 3). According to Section 3, its angular frequency $\lambda = -1/2$ is constant regardless of the value of $|\alpha|$. When $m = 1$ and $\lambda = -1/2$, (8) are simplified as

$$\left( \frac{1}{2} \nabla_{\text{h}}^2 + 1 \right) \tilde{\psi} = |\alpha| \mu (\nabla_{\text{h}}^2 + 6) \left[ \frac{\text{sgn}(\alpha) \tilde{a}}{\sqrt{\rho_0 \mu_{\text{m}}}} \right], \tag{49a}$$

$$\frac{1}{2} \left[ \frac{\text{sgn}(\alpha) \tilde{a}}{\sqrt{\rho_0 \mu_{\text{m}}}} \right] = |\alpha| \mu \tilde{\psi}. \tag{49b}$$

If both sides of both (49a) and (49b) did not vanish, the above equations would be transformed into the same form as (9) and inevitably possess critical latitudes $\mu_{\text{c}}^2 = 1/4\alpha^2$. We, therefore, presume that a solution for which
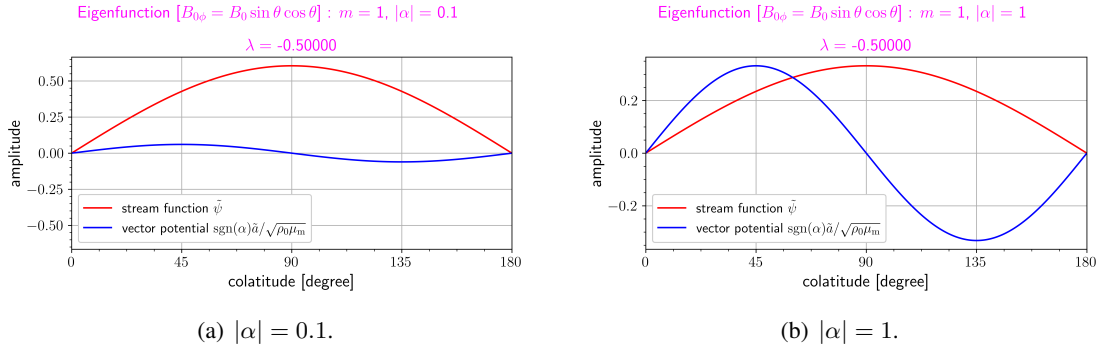
40

(a) $|\alpha| = 0.1$.

(b) $|\alpha| = 1$.

Figure 26: Same as Figure 6(a), but for the fast MR wave buried in the Alfvén continuous spectrum (the zonal wavenumber $m = 1$ and the nondimensional angular frequency $\lambda = -0.5$).

both sides of (49a) are identically equal to zero exists. Because one knows $\nabla_{\mathrm{h}}^2 \mathrm{P}_1^1 = -2\mathrm{P}_1^1$, $\nabla_{\mathrm{h}}^2 \mathrm{P}_2^1 = -6\mathrm{P}_2^1$, and $\mu \mathrm{P}_1^1 = \mathrm{P}_2^1/3$ from (18), the presumption requires that its eigenfunction is written as $\tilde{\psi} = \tilde{\psi}^{[1]} \mathcal{N}_1^1 \mathrm{P}_1^1$ and $\mathrm{sgn}(\alpha)\tilde{a}/\sqrt{\rho_0 \mu_{\mathrm{m}}} = \tilde{a}^{[2]} \mathcal{N}_2^1 \mathrm{P}_2^1$, where $2|\tilde{\psi}^{[1]}|^2 + 6|\tilde{a}^{[2]}|^2 = 1$ and $\tilde{a}^{[2]}/\tilde{\psi}^{[1]} = 2|\alpha|/\sqrt{5}$ (see Figure 26). This implies that this discrete mode buried in the continuous spectrum is exceptional. On its branch, the equipartition between MKE and MME occurs only when $|\alpha| = \sqrt{5/12} \approx 0.6455$, and we found that the value agrees with that which one can read from the colours of markers in the upper left panel of Figure 3. Furthermore, we notice that its angular frequency $\lambda = -1/2$ satisfies even the approximate dispersion relation (48) for fast MR waves "outside" the continuous spectrum, since one then has $c^2 = 20\alpha^2$ and $\lambda_{11} = 2 + 4\alpha^2$. Nevertheless, its (exact) eigenfunction $\tilde{\psi}^{[1]} \mathcal{N}_1^1 \mathrm{P}_1^1$ is not identical with the approximate eigenfunctions $\mathrm{S}_{11}/\sqrt{\Lambda}$ for the fast modes outside the continuous spectrum (see Appendix B).

It should be added, at the end of this appendix, that Wang *et al.* (2022b) recently studied two distinctive modes in the same system as our problem. One is the above buried discrete mode ($\lambda = -1/2$), and the other is the stationary mode ($\lambda = 0$) whose eigenfunction is represented as $\psi_1 = 0$ and $a_1 \propto \mathrm{P}_2^1 e^{i\phi}$ in (49). Their paper showed that the latter is closely linked to "clamshell instability" (see Section 1) and referred to this mode as the "tilting mode". On the other hand, we consider that the former is also interesting, because this mode remains stationary in the non-rotating frame although this is a rotating fluid problem, as shown in Wang *et al.* (2022b). Those two modes are similar in terms of the tilt of a toroidal magnetic field. For the buried mode of the fast MR wave, the perturbation $\psi_1$ in the stream function, which is proportional to $\mathrm{P}_1^1 e^{i\phi}$, makes the imposed field $B_{0\phi} = B_0 \sin\theta \cos\theta$ tilt, hence the perturbation $a_1 \propto \mathrm{P}_2^1 e^{i\phi}$ in the magnetic vector potential. Such a total magnetic field does not obviously induce the Lorentz force acting on the perturbation. Recall that the right-hand side of (49a) vanishes when $\mathrm{sgn}(\alpha)\tilde{a}/\sqrt{\rho_0 \mu_{\mathrm{m}}} \propto \mathrm{P}_2^1$.

# D Derivations of the ray-tracing equations and their related formulae

This appendix explains detailed derivations of the ray-tracing equations and their related formulae, which were skipped in Section 4. We first introduce the parameter given by $s \equiv -\mathrm{sgn}(\ln|\alpha|)$. Then, $|\alpha|^s \leq 1$ is always satisfied regardless of the magnitude of $|\alpha|$. If one is interested in a restricted situation that is represented by either $|\alpha| \gg 1$ or $|\alpha| \ll 1$, the parameter $|\alpha|^s$ becomes sufficiently smaller than unity. Utilising this small parameter, we can express the separations of the spatial and the temporal scales, as explained in Section 4. In other words, with the local coordinates $(\Phi, \Theta, \tau)$ and the global ones $(\phi, \theta, T)$, we can write

$$\Theta \equiv |\alpha|^{-sp}\theta, \qquad \Phi \equiv |\alpha|^{-sp}\phi, \qquad T \equiv |\alpha|^{sq}\tau, \qquad (50)$$

where $p, q > 0$.

In such separations, the local coordinates are supposed to be suitable to measure the phase $\varphi_{\mathrm{L}}$ of waves. The local wavenumber and local nondimensional angular frequency, which may depend only on the global

41

coordinates, are accordingly defined as

$$k(\phi, \theta, T) \equiv \frac{1}{\sin\theta}\frac{\partial\varphi_{\mathrm{L}}}{\partial\Phi} = \frac{1}{\sin\theta}\frac{\partial(|\alpha|^{sp}\varphi_{\mathrm{G}})}{\partial\phi} = |\alpha|^{sp}\frac{m}{\sin\theta}, \tag{51a}$$

$$l(\phi, \theta, T) \equiv \frac{\partial\varphi_{\mathrm{L}}}{\partial(-\Theta)} = \frac{\partial(|\alpha|^{sp}\varphi_{\mathrm{G}})}{\partial(-\theta)}, \tag{51b}$$

$$\lambda(\phi, \theta, T) \equiv -\frac{\partial\varphi_{\mathrm{L}}}{\partial\tau} = -|\alpha|^{s(q-p)}\frac{\partial(|\alpha|^{sp}\varphi_{\mathrm{G}})}{\partial T}, \tag{51c}$$

where $\varphi_{\mathrm{G}}(\phi, \theta, T)$ $(= \varphi_{\mathrm{L}}(\Phi, \Theta, \tau))$ denotes the phase function whose independent variables are the global coordinates. Now we recognise that $k$, $l = \mathrm{O}(|\alpha|^0)$ by construction, and that the zonal wavenumber $m = \mathrm{O}(|\alpha|^{-sp})$ measured in the global coordinates is large. This implies that $\lambda = \mathrm{O}(|\alpha|^{s(q-p)})$, and we introduce the scaled nondimensional angular frequency $H \equiv |\alpha|^{s(p-q)}\lambda$. In addition, (51) yield the curl-free conditions

$$\frac{\partial(k\sin\theta)}{\partial(-\theta)} = \frac{\partial l}{\partial\phi}, \qquad -\frac{\partial(k\sin\theta)}{\partial T} = \frac{\partial H}{\partial\phi}, \qquad -\frac{\partial l}{\partial T} = \frac{\partial H}{\partial(-\theta)}. \tag{52}$$

If we consider $(\phi, -\theta)$ to be generalised coordinates in analytical mechanics, $(k\sin\theta, l)$ and $|\alpha|^{sp}\varphi_{\mathrm{G}}$ can, from (51a) and (51b), correspond to generalised momentums and a generating function, respectively. The first equation of (52) is also equivalent to the property $\{k\sin\theta, l\} = 0$ of the Poisson bracket. On the basis of these facts, we may raise the topic of the Hamilton–Jacobi equation

$$\frac{\partial(|\alpha|^{sp}\varphi_{\mathrm{G}})}{\partial T} + \mathcal{H}(\phi, \theta, k, l, T) = 0, \tag{53}$$

where $\mathcal{H}$ is the "Hamiltonian" for our problem. We however will not pursue the solution $|\alpha|^{sp}\varphi_{\mathrm{G}}$ of this equation. Upon comparing (51c) to (53) and treating $H$ as an independent variable, one obtains a dispersion relation in the form

$$\mathcal{D}_{\mathcal{H}}(\phi, \theta, T, k, l, H) \equiv H - \mathcal{H}(\phi, \theta, k, l, T) = 0. \tag{54}$$

The nondimensional local group velocity with respect to the dimensionless time $\tau$ and the coordinates $(\phi, -\theta)$ is then written as

$$c_{\mathrm{g},\phi} \equiv -\frac{[\partial\mathcal{D}_{\mathcal{H}}/\partial(|\alpha|^{-sp}k)]|_{H=\mathcal{H}}}{[\partial\mathcal{D}_{\mathcal{H}}/\partial(|\alpha|^{s(q-p)}H)]|_{H=\mathcal{H}}} = |\alpha|^{sq}\frac{\partial\mathcal{H}}{\partial k}, \tag{55a}$$

$$c_{\mathrm{g},-\theta} \equiv -\frac{[\partial\mathcal{D}_{\mathcal{H}}/\partial(|\alpha|^{-sp}l)]|_{H=\mathcal{H}}}{[\partial\mathcal{D}_{\mathcal{H}}/\partial(|\alpha|^{s(q-p)}H)]|_{H=\mathcal{H}}} = |\alpha|^{sq}\frac{\partial\mathcal{H}}{\partial l}. \tag{55b}$$

Instead of the Hamilton–Jacobi equation (53), we will solve the ray-tracing equations, which are the counterparts of Hamilton's equations in analytical mechanics, in the forms

$$\sin\theta\frac{\mathrm{d}_{\mathrm{g}}\phi}{\mathrm{d}T} = \frac{\partial\mathcal{H}}{\partial k} = |\alpha|^{-sq}c_{\mathrm{g},\phi}, \qquad \frac{\mathrm{d}_{\mathrm{g}}(-\theta)}{\mathrm{d}T} = \frac{\partial\mathcal{H}}{\partial l} = |\alpha|^{-sq}c_{\mathrm{g},-\theta}, \tag{56a}$$

$$\frac{\mathrm{d}_{\mathrm{g}}(k\sin\theta)}{\mathrm{d}T} = -\left(\frac{\partial\mathcal{H}}{\partial\phi}\right)_{k,l}, \qquad \frac{\mathrm{d}_{\mathrm{g}}l}{\mathrm{d}T} + |\alpha|^{-sq}c_{\mathrm{g},\phi}k\cot\theta = -\left[\frac{\partial\mathcal{H}}{\partial(-\theta)}\right]_{k,l}, \tag{56b}$$

$$\frac{\mathrm{d}_{\mathrm{g}}H}{\mathrm{d}T} = \left(\frac{\partial\mathcal{H}}{\partial T}\right)_{k,l}, \tag{56c}$$

in which the material time derivative moving with the local group velocity is expressed as $(\mathrm{d}_{\mathrm{g}}/\mathrm{d}T) \equiv (\partial/\partial T) + |\alpha|^{-sq}(\boldsymbol{c}_{\mathrm{g}} \cdot \boldsymbol{\nabla}_{\mathrm{G}})$. Using the chain rule, one can also get (56b) and (56c) from (51), (52), (53), and (55).

The difference between our ray-tracing approach and standard analytical mechanics is that we do not initially know an explicit expression of the Hamiltonian. To obtain it, we need to substitute the ansatz $\psi_1 \equiv \mathrm{Re}[M(\phi, \theta, T)\mathrm{e}^{\mathrm{i}\varphi_{\mathrm{L}}(\Phi, \Theta, \tau)}]$ into the original partial differential equation

$$\left(\frac{\partial^2}{\partial\tau^2}\nabla_{\mathrm{h}}^2 + \frac{\partial^2}{\partial\tau\partial\phi}\right)\psi_1 = \alpha^2\left[\mathcal{B}^2\frac{\partial^2}{\partial\phi^2}\nabla_{\mathrm{h}}^2 + \frac{\mathrm{d}\mathcal{B}^2}{\mathrm{d}\theta}\frac{\partial^3}{\partial\phi^2\partial\theta} - \frac{2\mathcal{B}}{\sin\theta}\frac{\mathrm{d}(\mathcal{B}\cos\theta)}{\mathrm{d}\theta}\frac{\partial^2}{\partial\phi^2}\right]\psi_1, \tag{57}$$

which is constructed from the perturbation equations (7). For an arbitrary function $f(\phi, \theta, T)$, the relation

$$\frac{1}{\sin\theta}\frac{\partial(fMe^{i\varphi_L})}{\partial\phi} = \left[\frac{1}{\sin\theta}\frac{\partial f}{\partial\phi} + f\left(\frac{1}{\sin\theta}\frac{\partial\ln M}{\partial\phi} + i|\alpha|^{-sp}k\right)\right]Me^{i\varphi_L}, \tag{58}$$

and so forth, and nests of these are useful in the above tedious substitution. Then, one finds that the leading order terms of each term in (57) are $O(|\alpha|^{2s(q-2p)})$, $O(|\alpha|^{s(q-2p)})$, $O(|\alpha|^{2-4sp})$, $O(|\alpha|^{2-3sp})$, and $O(|\alpha|^{2-2sp})$ from the first term on the left-hand side to the third term on the right-hand side. A plausible balance among them requires that

$$2(q - 2p) = q - 2p = 2s - 4p \quad (< 2s - 3p < 2s - 2p). \tag{59}$$

One then has $s = 1$ ($|\alpha| \ll 1$), $p = 1/2$, and $q = 1$. Because possible balances for $s = -1$ do not exist, our approximation is probably inappropriate for the case when $|\alpha| \gg 1$. It follows that the leading order terms $O(|\alpha|^0)$ in (57) yield the local dispersion relation (29), or $\mathcal{D}(\phi, \theta, T, k, l, H) = 0$. Solving this relation for $H$, one can also obtain (54). Additionally, the next-to-leading order terms $O(|\alpha|^{1/2})$ are written as

$$\frac{\partial\ln M}{\partial T}\frac{\partial\mathcal{D}}{\partial H} - \frac{1}{\sin\theta}\frac{\partial\ln M}{\partial\phi}\frac{\partial\mathcal{D}}{\partial k} - \frac{\partial\ln M}{\partial(-\theta)}\frac{\partial\mathcal{D}}{\partial l} =$$
$$-\frac{\partial[H(k^2+l^2)]}{\partial T} - H\frac{\partial(k^2+l^2)}{\partial T} + \frac{H^2}{\sin\theta}\left[\frac{\partial k}{\partial\phi} + \frac{\partial(l\sin\theta)}{\partial(-\theta)}\right] - \frac{\partial(k\sin\theta)}{\partial T}$$
$$-\frac{1}{\sin\theta}\frac{\partial[k\mathcal{B}^2\sin^2\theta(k^2+l^2)]}{\partial\phi} - \frac{k}{\sin\theta}\frac{\partial[\mathcal{B}^2\sin^2\theta(k^2+l^2)]}{\partial\phi}$$
$$-\frac{k^2\mathcal{B}^2\sin^2\theta}{\sin\theta}\left[\frac{\partial k}{\partial\phi} + \frac{\partial(l\sin\theta)}{\partial(-\theta)}\right] - k^2l\frac{d\mathcal{B}^2}{d(-\theta)}\sin^2\theta. \tag{60}$$

Note that this equation is complex at a glance, but conforms to the same rule as the structure that the counterpart in Bretherton (1966) has. At last, the novel conservation law (38) is obtained from (30), (52), and (60) with (54).

In the remainder of this appendix and Appendix E, we shall set about the steady problem in which wave trains with specified values of $k\sin\theta$ and $H$ uniformly continue to be injected on a line of latitude. The discussion of the problem will teach one the behaviours of the steady trains near critical latitudes, where $l^2 \to \infty$. Its findings are also helpful in learning the behaviours of the trains near turning latitudes, at which $l = 0$ (see Appendix E). First of all, consider a region sandwiched between two ray trajectories drawn by the trains injected at two distinct longitudes ($\phi_1$ and $\phi_2$, say). This region may be called a "ray tube." Note that, because of the symmetry about the axis of rotation, one of the two trajectories can overlap the other by the rotation $|\phi_1 - \phi_2|$ about the axis. The distance between the two trajectories along a line of a colatitude $\theta$ is, therefore, $|\phi_1 - \phi_2|\sin\theta$. We then prepare two cross-sections of the tube along two lines of latitude. Let $S$ be the region bounded by the two sections on the tube. For the steady problem with the uniform injection, the surface integral of (38) over $S$ gives

$$\frac{c_{g,-\theta}}{|\alpha|}\frac{\partial\mathcal{D}}{\partial H}|M|^2\sin\theta = -\frac{\partial\mathcal{D}}{\partial l}|M|^2\sin\theta = \text{const.}. \tag{61}$$

Then, one obtains $|M|^2 \propto [l(H^2 - k^2\mathcal{B}^2\sin^2\theta)\sin\theta]^{-1}$, that is, $M = O(|\theta - \theta_c|^{-1/4})$ near a critical colatitude $\theta_c$ since $l = O(|\theta - \theta_c|^{-1/2})$ (from (33)) and $H^2 - k^2\mathcal{B}^2\sin^2\theta = O(|\theta - \theta_c|)$. This means that steady trains jam into such a latitude and that their amplitudes increase there. Note that the same is true for an isolated packet, as shown in the last paragraph of Section 4.

For constant values of $k\sin\theta$ and $H$, we can get the same expression for $|M|$ as the above in a different way. The solution is again redefined as $\psi_1 \equiv \text{Re}[\tilde{\psi}(\theta)e^{i\varphi}]$ with $\varphi = |\alpha|^{-1/2}(k\sin\theta)\phi - |\alpha|^{1/2}H\tau$, where we conjecture that $\tilde{\psi}$ can be expressed by the WKBJ (Wentzel–Kramers–Brillouin–Jeffreys) form

$$\tilde{\psi} \equiv \exp\left[-i\int^\theta L(\theta_*)d\theta_*\right]. \tag{62}$$

Consequently, one has $(d\tilde{\psi}/d(-\theta)) = iL\tilde{\psi}$. Provided that $L = |\alpha|^{-1/2}l + L_0 + O(|\alpha|^{1/2})$, the leading order

terms $\mathrm{O}(|\alpha|^0)$ in the ordinary differential equation (9), which can be written as

$$
|\alpha| \frac{H^2 - k^2 \mathcal{B}^2 \sin^2 \theta}{\sin \theta} \frac{\mathrm{d}}{\mathrm{d}\theta} \left( \sin \theta \frac{\mathrm{d}\tilde{\psi}}{\mathrm{d}\theta} \right) - |\alpha| k^2 \sin^2 \theta \frac{\mathrm{d}\mathcal{B}^2}{\mathrm{d}\theta} \frac{\mathrm{d}\tilde{\psi}}{\mathrm{d}\theta}
$$
$$
- \left[ k^2 (H^2 - k^2 \mathcal{B}^2 \sin^2 \theta) + Hk \sin \theta - 2|\alpha| k^2 \sin \theta \mathcal{B} \frac{\mathrm{d}(\mathcal{B} \cos \theta)}{\mathrm{d}\theta} \right] \tilde{\psi} = 0 \tag{63}
$$

if we use $k$ and $\theta$ instead of $m$ and $\mu$, lead to the local dispersion relation (29). Its next-to-leading order terms $\mathrm{O}(|\alpha|^{1/2})$ become the equation for $L_0$ in the form

$$
\mathrm{i}L_0 = \frac{1}{2} \frac{\mathrm{d} \ln |l(H^2 - k^2 \mathcal{B}^2 \sin^2 \theta) \sin \theta|}{\mathrm{d}\theta} \tag{64}
$$

when $l \neq 0$ and $H^2 \neq k^2 \mathcal{B}^2 \sin^2 \theta$, resulting in

$$
\tilde{\psi} \propto \frac{1}{|l(H^2 - k^2 \mathcal{B}^2 \sin^2 \theta) \sin \theta|^{1/2}} \exp \left\{ -\mathrm{i} \int^\theta \left[ |\alpha|^{-1/2} l(\theta_*) + \mathrm{O}(|\alpha|^{1/2}) \right] \mathrm{d}\theta_* \right\}. \tag{65}
$$

The pre-exponent of this WKBJ solution is consistent with $|M|$ in (61), and $\varphi_\mathrm{G}$ in (51) is equivalent to $\varphi - |\alpha|^{-1/2} \int^\theta l(\theta_*) \mathrm{d}\theta_*$ as long as we pay attention to the solutions with constant values of $k \sin \theta$ and $H$.

# E    Behaviors of wave packets near a turning latitude

The last appendix is devoted to an investigation into the behaviours of wave packets near turning latitudes, where $l = 0$, when $|\alpha| \ll 1$ (see also Section 4 and Appendix D). We here write $l^2 = (l_\mathrm{t}^2)'(\theta - \theta_\mathrm{t}) + \mathrm{O}(|\theta - \theta_\mathrm{t}|^2)$ in the vicinity of a turning colatitude $\theta = \theta_\mathrm{t}$, in which $(l_\mathrm{t}^2)' \equiv (\mathrm{d}l^2/\mathrm{d}\theta)|_{\theta=\theta_\mathrm{t}}$ (and we assume that $(l_\mathrm{t}^2)' \neq 0$). If a packet advances toward its corresponding turning latitude from a nearby latitude $\theta$, it can then reach there in a finite time

$$
\int_\theta^{\theta_\mathrm{t}} \frac{|\alpha|}{-c_{\mathrm{g},-\theta}(\theta_*)} \mathrm{d}\theta_* \simeq \pm \frac{2Hk^2 + k \sin \theta}{2|(l_\mathrm{t}^2)'|^{1/2}(H^2 - k^2 \mathcal{B}^2 \sin^2 \theta)} \bigg|_{\theta=\theta_\mathrm{t}} \int_\theta^{\theta_\mathrm{t}} \frac{\mathrm{d}\theta_*}{\left\{ \mathrm{sgn} \left[ (l_\mathrm{t}^2)' \right] (\theta_* - \theta_\mathrm{t}) \right\}^{1/2}}
$$
$$
= \mathrm{O}(|\theta - \theta_\mathrm{t}|^{1/2}), \tag{66}
$$

and its refraction will occur. The asymptotic expression $M = \mathrm{O}(|\theta - \theta_\mathrm{t}|^{-1/4})$ of its amplitude near the turning latitude is obtained from (61). In addition, the valid range (39) of the ray theory is given by $|\theta - \theta_\mathrm{t}| \gg \mathrm{O}(|\alpha|^{1/3})$. This tempts us into introducing a new stretched coordinate $y \equiv |\alpha|^{-1/3}\theta$ (with $y_\mathrm{t} \equiv |\alpha|^{-1/3}\theta_\mathrm{t}$). One should notice that the scale of $y$ is a little coarser than that of $\Theta$, since $\theta = |\alpha|^{1/3}y = |\alpha|^{1/2}\Theta$. The WKBJ solutions (65) are then valid in the range $\mathrm{O}(|\alpha|^0) \ll |y - y_\mathrm{t}|$; in particular, the solutions near the turning latitude within the range $\mathrm{O}(|\alpha|^0) \ll |y - y_\mathrm{t}| \ll \mathrm{O}(|\alpha|^{-1/3})$ are written as

$$
\tilde{\psi} \simeq \frac{C}{|\alpha|^{1/12}|(l_\mathrm{t}^2)'|^{1/6}Y^{1/4}|(H^2 - k^2 \mathcal{B}^2 \sin^2 \theta) \sin \theta|^{1/2}} \exp \left\{ -\mathrm{i} \frac{2}{3} \mathrm{sgn} \left[ l(l_\mathrm{t}^2)' \right] \left( Y^{3/2} - Y_0^{3/2} \right) \right\}, \tag{67}
$$

where $C$ and $Y_0$ are constants and $Y \equiv |(l_\mathrm{t}^2)'|^{-2/3}(l_\mathrm{t}^2)'(y - y_\mathrm{t})$. The signs of $(l_\mathrm{t}^2)'$ and the meridional component $|\alpha|(H/l)$ of the phase velocity determine whether the packet is the incident ($l(l_\mathrm{t}^2)'/H > 0$) or reflected waves ($l(l_\mathrm{t}^2)'/H < 0$). Note that the scaled stretched coordinate $Y$ is always positive in the oscillatory region $l^2 > 0$.

When $y - y_\mathrm{t} = \mathrm{O}(|\alpha|^0)$, the above approximation breaks down. This is because $\mathrm{i}L_0 \simeq (1/2)(\mathrm{d} \ln |l|/\mathrm{d}\theta) = \mathrm{O}(|\theta - \theta_\mathrm{t}|^{-1})$ is of the same order of magnitude as $|\alpha|^{-1/2}l$. To match an incident wave with its corresponding reflected one at its corresponding turning latitude $y = y_\mathrm{t}$, we need to return to the original equation (63). Without the need to introduce $L$, we substitute the Taylor expansion of (32b) around the turning latitude in the form

$$
-k^2 - \frac{Hk \sin \theta}{H^2 - k^2 \mathcal{B}^2 \sin^2 \theta} = (l_\mathrm{t}^2)'(\theta - \theta_\mathrm{t}) + \mathrm{O}(|\theta - \theta_\mathrm{t}|^2) \tag{68}
$$

into (63), and use the variable $Y$ to take the dominant terms at $\theta - \theta_\mathrm{t} = \mathrm{O}(|\alpha|^{1/3})$, to obtain

$$
\frac{\mathrm{d}^2 \tilde{\psi}}{\mathrm{d}(-Y)^2} = (-Y)\tilde{\psi} + \mathrm{O}(|\alpha|^{1/3}), \tag{69}
$$

which is the Airy differential equation (e.g. Abramowitz and Stegun, 1964). Because $\tilde{\psi}$ should vanish as $Y \to -\infty$ (evanescent), the equation has $\tilde{\psi} = C_A \mathrm{Ai}(-Y)$ as its solution, in which $\mathrm{Ai}$ denotes the Airy function of the first kind and $C_A$ is a constant. We now require that the asymptotic expression for this solution as $Y \to +\infty$ ($\ll \mathrm{O}(|\alpha|^{-1/3})$), which is given by

$$\mathrm{Ai}(-Y) \sim \frac{1}{\sqrt{\pi}Y^{1/4}} \cos\left(\frac{2}{3}Y^{3/2} - \frac{\pi}{4}\right) \qquad (Y \to +\infty), \tag{70}$$

should match the sum $\tilde{\psi}_i + \tilde{\psi}_r$ of the incident ($C = C_i$, say) and reflected ($C = C_r$, say) waves (Lighthill, 1978). It follows that, if $C_i = C_r$ (total reflection), one has $(2/3)Y_0^{3/2} = N_0\pi + (\pi/4)$ ($N_0 = 0, \pm1, \pm2, \ldots$) and

$$\frac{C_A}{C_i} = \frac{2\sqrt{\pi}(-1)^{N_0}}{|\alpha|^{1/12}|(l_t^2)'|^{1/6}|(H^2 - k^2\mathcal{B}^2\sin^2\theta)\sin\theta|^{1/2}}. \tag{71}$$

These expressions constitute consistent solutions to the incident, reflected and evanescent waves across a turning latitude.

We have a by-product of the above study of the matching of solutions. The expression of the constant $Y_0$ of integration, or the phase shift $\pi/4$ in (70), implies the existence of the quantization condition of waves that have no critical latitudes (which include waves under the Malkus background field $\mathcal{B} = 1$, and fast MR waves for the simplest equatorially-antisymmetric non-Malkus field $\mathcal{B} = \cos\theta$). The condition is expressed as

$$|\alpha|^{-1/2} \int_{\theta_{t1}}^{\theta_{t2}} |l|\,\mathrm{d}\theta = \int_{\theta_{t1}}^{\theta_{t2}} \sqrt{-\frac{m\lambda}{\Lambda} - \frac{m^2}{\sin^2\theta}}\,\mathrm{d}\theta = \left(N + \frac{1}{2}\right)\pi \quad (N = 0, 1, 2, \ldots), \tag{72}$$

where $l^2 > 0$ through the range $\theta_{t1} < \theta < \theta_{t2}$ between two different turning colatitudes $\theta_{t1}$ and $\theta_{t2}$. For $\mathcal{B} = 1$, we use the substitution $x \equiv \cos\theta/\sqrt{\sin^2\theta - (\lambda^2 - m^2\alpha^2)/(-\lambda/m)}$ to calculate the integral, getting

$$\pi\left(\sqrt{-\frac{m\lambda}{\lambda^2 - m^2\alpha^2}} - |m|\right) = \left(N + \frac{1}{2}\right)\pi. \tag{73}$$

Letting $n \equiv |m| + N$, one obtains an approximate formula for the dispersion relation (1) in the form

$$\lambda = \frac{-m \pm m\sqrt{1 + 4\alpha^2[n(n+1) + (1/4)]^2}}{2[n(n+1) + (1/4)]}. \tag{74}$$

As expected, the larger the value of $n$ is, the more accurately the above formula approximates the relation (1). Next, we proceed to the case when $\mathcal{B} = \cos\theta$. If we perform the substitution $x \equiv \cos\theta/\sqrt{\sin^2\theta - \kappa^{-2}}$, where $\kappa^2 \equiv (-\lambda/m - m^2\alpha^2)/(\lambda^2 - m^2\alpha^2)$, the condition (72) becomes

$$(1 + m\lambda)\sqrt{-\frac{m\lambda}{\lambda^2 - m^2\alpha^2}\kappa^2} \int_{-\infty}^{\infty} \frac{\mathrm{d}x}{(x^2 + \kappa^2)\sqrt{(x^2 + 1)(x^2 + (-m\lambda)\kappa^2)}} = \left(N + \frac{1}{2}\right)\pi. \tag{75}$$

Note that, in the above equation, either $1 < (-m\lambda)\kappa^2 < \kappa^2$ or $0 < (-m\lambda)\kappa^2 < 1 < \kappa^2$ holds, because we find that $1 + m\lambda > 0$ during the derivation of (75). To evaluate the integral in (75), we consider the integral of a complex-valued function of $z$ ($\equiv x + iy$) in the form

$$\oint_{C_0} \frac{\mathrm{d}z}{(z^2 + \kappa^2)\sqrt{(z^2 + a^2)(z^2 + b^2)}}$$

$$= \oint_{C_1 + C_2} \frac{\mathrm{d}z}{(z^2 + \kappa^2)\sqrt{(z^2 + a^2)(z^2 + b^2)}}$$

$$= 2\pi i\,\mathrm{Res}\left(\frac{1}{(z^2 + \kappa^2)\sqrt{(z^2 + a^2)(z^2 + b^2)}}, i\kappa\right) + 2\int_a^b \frac{\mathrm{d}y}{(\kappa^2 - y^2)\sqrt{(y^2 - a^2)(b^2 - y^2)}}$$

$$= -\frac{\pi}{\kappa\sqrt{(\kappa^2 - a^2)(\kappa^2 - b^2)}}$$

$$+ \frac{2}{\kappa^2 b}\int_0^1 \frac{\mathrm{d}v}{\sqrt{(1 - v^2)(1 - \gamma v^2)}} + \frac{2a^2}{\kappa^2 b(\kappa^2 - a^2)}\int_0^1 \frac{\mathrm{d}v}{(1 - \chi v^2)\sqrt{(1 - v^2)(1 - \gamma v^2)}}, \tag{76}$$
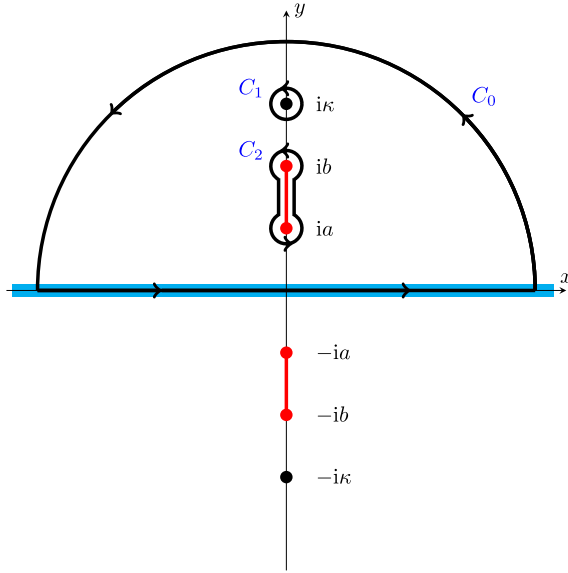
Figure 27: Path of integration for the integral (76). The contours $C_0$, $C_1$ and $C_2$ are represented as thick black curves. The black and red circles are poles and branch points, respectively, and the red lines correspond to branch cuts. The integral in (75) must be evaluated along the path represented as the cyan line.

where $a \equiv \min(1, \sqrt{-m\lambda}\kappa)$, $b \equiv \max(1, \sqrt{-m\lambda}\kappa)$, $\gamma \equiv 1 - (a/b)^2$, and $\chi \equiv \gamma\kappa^2/(\kappa^2 - a^2)$. In addition, the contours $C_0$, $C_1$ and $C_2$ of integration are shown in Figure 27, and the substitution $y = ab/\sqrt{b^2 - (b^2 - a^2)v^2}$ has been used in the last equal sign of (76). When the radius of the semicircle bounded by the contour $C_0$ goes to infinity, one knows that (76) is equal to the integral in (75). Because the integrals in the rightmost side of (76) are the complete elliptic integrals of the first and third kinds for the elliptic modulus $\gamma$ and the characteristic $\chi$ (e.g. Abramowitz and Stegun, 1964), its calculation requires a numerical method. Figure 28 shows the approximate angular frequencies obtained from (75), the calculation of which was performed by the `scipy.optimize.fsolve` and the `scipy.integrate.quad` functions of the SciPy library. The condition (72) will provide the approximate dispersion relation for discrete modes when any basic field is imposed and can be utilised for the check of the numerical calculation of the full eigenvalue problem for such a field.
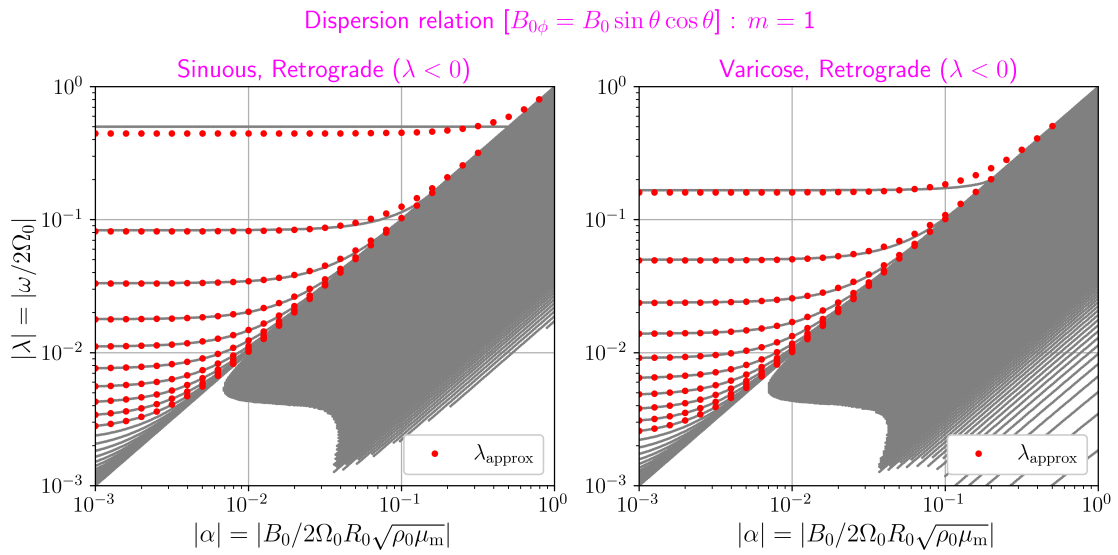
Figure 28: Same as Figure 23, but for the approximate dimensionless angular frequencies $\lambda_{\text{approx}}$ calculated by the approximate dispersion relation (75) instead of (48).